# Quantitative Imaging of Living Cells by Deep Ultraviolet Microscopy

by

Benjamin J. Zeskind

S.B., Electrical Engineering & Computer Science
Massachusetts Institute of Technology, 2003

Submitted to the Biological Engineering Division
in Partial Fulfillment of the Requirements for the Degree of
Doctor of Philosophy in Bioengineering
at the
MASSACHUSETTS INSTITUTE OF TECHNOLOGY

June 2006



Signature of Author: _____

Benjamin J. Zeskind
Biological Engineering Division

Certified by: _____

Paul Matsudaira
Professor of Biological Engineering and Biology
Thesis Supervisor

Accepted by: _____

Alan J. Grodzinsky
Professor of Biological Engineering
Chairman, Committee for Graduate Students

This doctoral thesis has been examined by a committee of the Biological Engineering Division as follows:

Chairperson, Graduate Thesis Committee: _____

Peter So
Professor of Biological Engineering
and Mechanical Engineering

Thesis Committee Member: _____

Matt Lang
Professor of Biological Engineering
and Mechanical Engineering
Thesis Committee Member

Thesis Committee Member: _____

Scott Manalis
Professor of Biological Engineering
Thesis Committee Member

Quantitative Imaging of Living Cells by Deep Ultraviolet Microscopy

by

Benjamin J. Zeskind

Submitted to the Biological Engineering Division on April 13, 2006 in Partial Fulfillment of the Requirements for the Degree of Doctor of Philosophy in Bioengineering

ABSTRACT

**Developments in light microscopy over the past three centuries have opened new windows into cell structure and function, yet many questions remain unanswered by current imaging approaches. Deep ultraviolet microscopy received attention in the 1950s as a way to generate image contrast from the strong absorbance of proteins and nucleic acids at wavelengths shorter than 300 nm. However, the lethal effects of these wavelengths limited their usefulness in studies of cell function, separating the contributions of protein and nucleic acid proved difficult, and scattering artifacts were a significant concern. We have used short exposures of deep-ultraviolet light synchronized with an ultraviolet-sensitive camera to observe mitosis and motility in living cells without causing necrosis, and quantified absorbance at 280 nm and 260 nm together with tryptophan native fluorescence in order to calculate maps of nucleic acid mass, protein mass, and quantum yield in unlabeled cells. We have also developed a method using images acquired at 320nm and 340nm, and an equation for Mie scattering, to determine a scattering correction factor for each pixel at 260nm and 280nm. These developments overcome the three main obstacles to previous deep UV microscopy efforts, creating a new approach to imaging unlabeled living cells that acquires quantitative information about protein and nucleic acid as a function of position and time.**

Thesis Supervisor: Paul Matsudaira

Title: Professor of Biological Engineering and Biology

**ACKNOWLEDGEMENTS**

First I'd like to thank Paul Matsudaira. Paul took a risk by welcoming into his lab an electrical engineer with little biology background, and I hope that the gamble proved worthwhile. He then took another risk by supporting my desire to pursue live-cell UV imaging, an idea that most biologists would have dismissed as impossible. Paul's willingness to encourage unconventional ideas stands out in a field that is too often dogmatic, and such flexibility of thought is crucial to the future of biology and medicine. The following pages give testimony in support of Paul's philosophy.

Paul was extremely patient and encouraging during the early phases of the research when progress was slow, and more recently as the data improved he managed to simultaneously convey his excitement and challenge me to push the work further. His guidance has proven strategically valuable, shaping the course of this research at every turning point. At the same time, he gave me the freedom, flexibility, and resources to pursue the research however I saw fit. I have taken many lessons from Paul's leadership style.

From the very beginning of this work, Matt Lang has proven a key resource. He has always been approachable and generous with his time. Matt's knowledge of optics is ironclad. I eventually developed a rule about Matt's suggestions: either I would implement them right away, or I would implement them later and wish that I had implemented them right away!

Peter So has also played a critical role, asking insightful questions and guiding the thesis committee. His microscopy course also proved helpful in cementing much of my knowledge of microscopy.

Scott Manalis was one of the first people who encouraged me to apply to BE. His suggestion to use PDMS channels for calibration was crucial, as was the assistance from members of his lab in creating these devices.

Dan Ehrlich created an environment that was an engineer's paradise, with tools for the electrical, optical, mechanical and chemical aspects of every project. Dan also helped me gain experience writing grants, and was always willing to provide interesting feedback on any document I produced.

While I have only met with Shinya Inoué three times, each of those meetings proved a critical turning point in my research. The UV condenser that he loaned me was crucial for my work, and equally important were his suggestions and perspective.

I would also like to acknowledge Doug Lauffenburger. Doug has gone out of his way to be supportive, and I truly believe that he has created a department that will have a significant impact on the future of biology and medicine.

I am grateful to the members of the Matsudaira lab for their support. In particular, Guichy Waller was extremely helpful with general advice as well as preparing calibration solutions. Nicki Watson generously loaned me much of the equipment used in my initial setup. Winston Timp helped me establish the live-cell procedures and was a wealth of knowledge of many subjects. Danielle Cook France helped me establish the connection to Shinya and provided many useful suggestions. James Evans helped facilitate my move to 500 Tech Square which proved extremely important. Roger Lam designed and constructed crucial amplifiers and driver circuits. I am also grateful to Mekhail Anwar, Lera Baru, Yelena Freyzon, Victor Horodincu, Brian McKenna, Mike Murrell, and Barney Tam, as well as former members James Aborn and Nils Goedecke.

Caroline Jordan, a talented UROP student, helped make native fluorescence imaging a reality.

Johnson Hou in the Manalis lab was critical in building PDMS devices; Bianca Sculimbrene in the Imperiali Lab helped with a key measurement in their well-calibrated fluorimeter; and Sandy McAllister of the Weinberg Lab provided an important plate of HMLER cells.

Administrative support has also been crucial. I particularly appreciate the fine work of Erin Keegan and Olga Parkin. Kristine Marzilli and previously Tom Canel were also helpful. I also appreciate the help of Pat Granahan, Amina Hamzoui, and Rena Denoncourt in the Whitehead IP office. Shawna Vogel in the MIT TLO went above and beyond the call of duty in answering my endless stream of questions.

I acknowledge my fellow BE graduate students for their advice and friendship.

Finally, I would like to thank my friends for tolerating my obsession with lab, and my family for their love and encouragement. I treasure my father's advice, my mother's support, and my sister's candor.

TABLE OF CONTENTS

## LIST OF FIGURES

**Fig. 16:** A diagram, image of fixed IC-21 cells, and photo of our scope with oblique flood illumination from above, and the new internal dichroic filter.

**Fig. 17:** 3D rendering of deconvolved native fluorescence image, and image of PolyFluor 345 microspheres (1μm diameter).

**Fig. 18:** Epifluorescent scope design for native fluorescence; **(right)** native fluorescence data with LED adjusted for uniform illumination (green) overlaid on visible transmission image (gray); **(bottom)** native fluorescence data with LED adjusted for max intensity: concentric circles are image of LED emitter.

**Fig. 19:** Diafluorescent scope design and image for native fluorescence scope.

**Fig. 20:** Native fluorescence with various emission filters. (**top left**) 320nm longpass filter, 15 sec exposure; (**top center**) Chroma HQ350/20x bandpass filter, 5 min exposure; (**top right**) ThorLabs 360nm bandpass filter, 5 min exposure; (**bottom left**) 320nm longpass filter, 40 sec exposure; (**bottom right**) 385nm longpass filter, 40 sec exposure.

**Fig. 21:** Block diagrams of our polarization modulator setup, (**top**) with initial beam combination method, and (**Bottom**) with mirror-edge beam combination method.

**Fig. 22:** Images of beams from polarization modulator for a cuvette of (**top**) water and (**bottom**) ~4mg/ml tryptophan.

**Fig. 23**: Verification that the polarization modulator beams are in fact orthogonally polarized. Varying peak heights may be due to a slight optical misalignment.

**Fig. 24**: Circular dichroism values for nucleoside solutions measured on our JASCO J-715 spectrophotometer. While the calibration of this instrument has been questionable, these spectra seem to qualitatively match those in [61].

**Fig. 25**: Photograph of polarization modulator adjacent to microscope.

**Fig. 26:** Diagram and photograph of our polarizing combiner condenser.

**Fig. 27:** Verification of dual-port orthogonal polarizations.

**Fig. 28:** Determination of half-wave plate angles for circular polarization.

**Fig. 29:** Determination of half-wave plate angles for circular polarization with Ultrafluar objective.

**Fig. 30:** Attempted CD images of CSA (**left**) and water (**right**) in quartz microchannels, units in mdeg, showing significant noise and inconsistency.

**Fig. 31:** Attempted CD images of IC-21s by manual rotation of quarter-wave plate. Left images are taken with the half-wave plate at each of the two angles determined to have circular polarization as shown in **Fig. 29**. Right image is the log of the ratio of these two images at each pixel, which equals the difference of the ODs, assuming constant field illumination.

**Fig. 32:** Attempted CD images of IC-21s by alternate use of side port and bottom port. Unlike the previous figure, we could no longer assume constant field illumination, so the log of the ratio of background to image at each position was taken to determine the OD at that position; the image on the right is the difference of these two ODs.

**Fig. 33:** Attempted FDCD images of IC-21s. **(top left and bottom left)** taken with the half-wave plate at each of the two angles determined to have circular polarization as shown in Fig. 29. **(top right)** Calculated CD from these two images by equations in the text. **(bottom right)** Another calculated FDCD image.

**Fig. 34**: Robust scope design.

**Fig. 35**: Adhesive heating elements on stage.

**Fig. 36**: Procedure for preparing live-cell samples.

**Fig. 37**: Time-lapse image of IC-21 subjected to 10 second UV exposures with 10 second delay in between, showing dramatic necrosis.

**Fig. 38**: Time-lapse image of IC-21 using 100 msec UV exposures with 60 second delay in between, showing no visible harm after six hours.

**Fig. 39:** 280nm time-lapse images of IC-21 motility.

**Fig. 40:** 280nm time-lapse images of HT-1080 motility.

**Fig. 41:** 280nm time-lapse images of HT-1080 mitosis.

**Fig. 42:** 280nm time-lapse images of another HT-1080 undergoing mitosis.

**Fig. 43:** Inverted, gamma-corrected 280nm time-lapse images of a third HT-1080 undergoing mitosis.

**Fig. 44:** Data from live/dead kit experiments, showing that cell morphology is a faster determinant of cell death than the live/dead kit. **(top row)** Time lapse images of 69 100ms exposures, followed by a live/dead image. **(second row)** Time lapse images of 181 10sec exposures with 1sec in between, followed by a live/dead image and an image

after 11 more 10 sec exposures. (**third row**) Time lapse of ethidium homodimer (dead kit) over ~2.5 hours, followed by a live/dead image.

**Fig. 45**: Time-lapse images of IC-21 native fluorescence using 10 second exposures separated by 60 second dark time. The cells clearly undergo necrosis. It is interesting to note that the background noise decreases, possible due to bleaching of proteins in the media.

**Fig. 46:** (**top**) 280nm transmission image of IC-21, with yellow line indicating location of line plots in bottom row. (**middle left**) Nucleic acid mass map. (**middle right**) Protein mass map. (**bottom left**) Line plot of nucleic acid mass. (**bottom right**) Line plot of protein mass.

**Fig. 47:** (**top left**) 260nm and (**top right**) 280nm transmission image of fixed mitotic HMLER cell. (**bottom left**) Nucleic acid and (**bottom right**) protein mass map.

**Fig. 48:** (**left**) Native fluorescence image and (**right**) calculated tryptophan quantum yield image for the same fixed unlabeled IC-21 shown in the previous chapter.

**Fig. 49:** (**red**) Normalized approximate quantum efficiency of our camera as a function of wavelength in nanometers, from manufacturer's specifications, (**green**) Normalized approximate transmission efficiency of our 320nm longpass filter from manufacturer's specifications, (**blue**) Normalized approximate emission spectra of tryptophan in solution, from our fluorimeter measurements.

**Fig. 50:** (**left**) Native fluorescence image and (**right**) calculated tryptophan quantum yield image for a fixed mitotic HMLER cell.

**Fig. 51:** (**left column**) Transmission images and (**right column**) OD images for (**first row**) 260nm, (**second row**) 280nm, (**third row**) 320nm, and (**fourth row**) 340nm.

**Fig. 52:** OD320 minus OD340 at each pixel, for (**top**) a more complete display range, and (**bottom**) a display range set to emphasize location of of negative values. Future work could investigate why the negative values seem more prevalent in the thinner areas of the cell – somewhat contrary to what one would expect for a type of scattering caused by larger particles.

**Fig. 53:** (**left column**) Original OD value, (**middle column**) calculated OD correction factor, and (**right column**) corrected OD value, for (**top row**) 260nm and (**bottom row**) 280nm.

**Fig. 54:** (**top row**) Uncorrected and (**bottom row**) scattering-corrected mass maps in grams for (**left column**) nucleic acid and (**right column** ) protein.

**Fig. 55:** Quantum yield map determined with (**left**) uncorrected and (**right**) scattering-corrected protein mass maps.

**Fig. 56:** For an object of diameter 10nm (much less than $\lambda$), curves showing the scattering magnitude as a function of wavelength in nm, for (**left**) the Mie approximation equation and (**right**) the Rayleigh scattering ($\lambda^{-4}$) approximation.

**Fig. 57:** (**left column**) Transmission images, (**center column**) uncorrected OD, and (**right column**) scattering-corrected OD images at (**first row**) 260nm, (**second row**) 280nm, (**third row**) 320nm, and (**fourth row**) 340nm.

**Fig. 58:** (**top row**) Uncorrected and (**bottom row**) scattering-corrected maps of (**left column**) nucleic acid mass, (**center column**) protein mass, (**right column**) and tryptophan quantum yield.

**Fig. 59:** (**left**) Protein mass minus nucleic acid mass, and (**right**) Protein mass divided by nucleic acid mass.

**Fig. 60:** (**top**) Protein mass displayed in green, overlaid with nucleic acid mass displayed in red, with each contrast set independently by autocontrast. (**bottom**) Same except contrast ranges set by hand.

**Fig. 61:** (**top left**) Protein mass image showing location of line plot. (**top right**) Nucleic acid mass map image showing location of line plot. (**bottom**) Line plot of protein mass and nucleic acid mass, each independently normalized.

**Fig. 62:** Motorized filter wheel for switching fiber input.

**Fig. 63:** 2$\lambda$ Imaging of HT-1080 mitosis. (**top row**) Time-lapse 260nm images. (**second row**) Time-lapse 280nm images. (**third row**) Time-lapse nucleic acid mass map with units in grams, (**bottom row**) Time-lapse protein mass map with units in grams.

**Fig. 64:** Motorized filter wheel for switching emission filters.

**Fig. 65:** 4 $\lambda$ Time-lapse images of HT-1080 mitosis. (**top row**) 260nm, (**second row**) 280nm, (**third row**) 320nm, and (**bottom row**) 340nm.

**Fig. 66:** Time-lapse mass maps of HT-1080 mitosis with units in grams. (**top row**) Uncorrected nucleic acid mass, (**second row**) uncorrected protein mass, (**third row**)

scattering-corrected nucleic acid mass, and **(bottom row)** scattering-corrected protein mass.

**Fig. 67:** PDMS/Quartz microchannel device.

**Fig. 68:** Validation using tryptophan solutions. **(left)** OD280 for microscope vs. spectrophotometer. Different absolute values are a result of different pathlengths. **(right)** Fluorescence for microscope versus fluorimeter.

**Fig. 69:** Validation using BSA-adenosine mixtures. **(A)** OD280 for microscope vs. spectrophotometer. Different absolute values are a result of different pathlengths. **(B)** OD260 for microscope vs. spectrophotometer. Different absolute values are a result of different pathlengths. **(C)** Fluorescence for microscope versus fluorimeter.

**Fig. 70:** **(top)** Image of fused silica Ronchi ruling with line, and **(bottom)** resulting line plot used to determine pixel size.

**Fig. 71:** A **(top row)** wider field and **(bottom row)** smaller field of 205nm beads at a variety of focal planes, for **(left column)** 480nm light. **(center column)** 280nm light, and **(right column)** 480nm light again.

**Fig. 72:** Negative quantum yield at cell edges as a result of lensing effects.

**Fig. 73:** The Nikon TE2000-U, **(top left)** shows the results of removing the stage, objective turret, and filter cube wheel. **(top center)** Shows the tube lens mount before and **(top right)** after removal of the tube lens. **(bottom left and center)** show the mounting of beamsplitter cubes in the path selector, and **(bottom right)** shows the empty "aux" position.

**Fig. 74:** **(left column)** Full images, and **(right column)** close-ups of a 5% caffeine tablet.

**Fig. 75:** Histograms of blank field **(left column)** transmission and **(right column)** autofluorescence measurements for **(top row)** functionalized quartz, **(second row)** blank quartz, **(third row)** glass slide, and **(bottom row)** no slide.

**Fig. 76:** **(top images)** Native fluorescence, blank field, and transmission images used to calculate quantum yield (color image) of a stalk extended with EGTA. **(bottom images)** Native fluorescence, blank field, and transmission images used to calculate quantum yield (color image) of a stalk contracted with $CaCl_2$.

**Fig. A1:** Cross section (top left) and photo (bottom left) of the photoacoustic chamber designed by our group. A beam splitter plate is placed over the central channel, sending a

reference beam of light out the channel on the left. The remaining light passes down the central channel and strikes the sample at the bottom of the chamber. The microphone is inserted in the channel on the right.

**Fig. A2:** Block diagram of our photoacoustic detector. Chopped laser light excites the sample in the chamber, creating vibrations that are detected by the microphone, amplified by the lock-in, and recorded on the computer. The magnitude of the signal is proportional to the absorption of the sample, according to the Rosencwaig-Gersho theory.

**Fig. A3:** Data measured with our photoacoustic detector, fitted with predictions from the Rosencwaig-Gersho theory. The sample was water with red dye. The circles, with error bars, represent the average and standard deviations of our measurements at a given frequency. The measured voltage is related to pressure by our microphone's conversion factor, and this pressure is related to the absorption of the sample. The dashed line is the R-G theory. We have used an arbitrary constant to scale the theory to the correct magnitude. Voltages are on the order of 20 μV and frequencies range from 0 – 2.5 kHz.

**Fig. A4:** Initial laser scanning photoacoustic microscope apparatus.

**Fig. A5:** Data from laser scanning photoacoustic microscope.

**Fig. A6:** Appartus for modulating two lasers at different frequencies and combining the resulting beam.

**Fig. A7:** Data from dual-wavelength photoacoustic microscope.

**Fig. A8:** Chip with microchannels coupled to photoacoustic chamber.

**Fig. A9:** Data from chip with microchannels.

**Fig. A10:** Data from photoacoustics on calf liver.

**Fig. A11:** Water coupled resonant chamber.

**Fig. A12:** Air coupled resonant chamber designed for Ealing objective.

**Fig. A13:** DUV LED photoacoustic apparatus.

**Fig. A14:** Data from DUV LED photoacoustic apparatus for an activated charcoal sample.

**Fig. A15:** Shimadzu spectrophotometer data at (top) low concentration and (top right) high concentration, and photoacoustic data at (bottom right) high concentration collected on our appartus (bottom left) demonstrating the ability of photoacoustics to measure a spectra even on concentrations at which the spectrophotometer saturates.

## LIST OF TABLES

# INTRODUCTION

## Chapter 1: Background and Motivation

### 1.1 Introduction

Developments in light microscopy over the past three centuries have opened new windows into cell structure and function, yet many questions remain that cannot be answered by current imaging approaches.

Fluorescent labeling is currently the most popular approach to biological imaging, and will likely remain so. Typically, a specific protein is labeled with a fluorophore such as fluorescein isothiocyanate (FITC) or green fluorescent protein (GFP). DNA can also be labeled, using fluorescent dyes such as Hoechst. The fluorophore is excited at a certain wavelength and fluoresces at a longer wavelength. The fluorescent signal is extremely strong and can be imaged rapidly and with high resolution in three dimensions and time. This enables many elegant experiments such as imaging the dynamic organization of histones over time [1]. Fluorescent labeling is a powerful tool, but there are some biological questions that cannot be answered using fluorescent labels.

Most fluorescence microscopes can only monitor three different fluorophores (channels) in any given sample. Even the most specialized systems can only monitor 5 or 6 channels. As a result, fluorescent labeling cannot effectively monitor many proteins simultaneously, except by using whole-cell stains such as CMFDA which are used for tracking cell motility.

In order to specifically label a protein, its identity must be known. Structures such as the non-histone protein scaffold in mitotic chromosomes [2] cannot be labeled because the proteins that compose it are unknown. Similarly, it is not possible to fluorescently label just the fiber of the spasmoneme in the contractile stalk of *Vorticella* since its protein composition is unknown [3].

Preparing samples for fluorescent labeling can also be time-consuming. Even a simple immunofluorescent labeling protocol on fixed cells [4] takes over 3 hours. Preparing GFP-expressing cells can take significantly longer. Indeed, some cell types such as primary cells cannot be transfected to produce GFP-labeled proteins. Fluorescent

dyes can also be expensive: CMFDA costs $184/mg, four orders of magnitude more than gold at ~$0.016/mg.

Fluorescent labels can also interfere with the sample under study. Literature has shown that GFP can increase the likelihood of apoptosis in NIH/3T3, BHK-21, Huh-7, and HepG2 cells [5], alter the intracellular localization of granulysin in NK cells [6], change the function of a Bfl-1 protein from anti-apoptotic to pro-apoptotic [7], cause aggregation of mitochondria [8], induce differentiation in human neuronal stem cells [9], cause apoptosis when coexpressed with beta-galactosidase in mouse neurons [10], and elicit an immune response in mice [11]. Our own lab's work has found that a common cell-tracking stain used for motility studies (CMFDA) actually inhibits cell motility as compared to GFP transformed cells [12].

### 1.2 Imaging Without Fluorescent Labels

Transmission bright field microscopy is perhaps the oldest form of microscopy, in use as early as the $17^{th}$ century. This method generates contrast based primarily on refractive effects around cell edges known as Becke lines [13] and a small amount of visible light absorption by cell components. Unfortunately, the major components of cells including DNA, RNA, and protein do not absorb strongly at these wavelengths and so the resulting images have extremely low contrast unless external stains, dyes, or other labels are added.

Two more advanced approaches to label-free imaging are commonly used today: phase contrast and differential interference contrast (referred to as DIC or Nomarski) microscopy. As shown in **Fig. 1**, phase contrast and DIC both produce excellent images of cell morphology. These approaches can be used on living cells without harm to produce informative time lapse movies of processes such as motility [14]. However, both approaches generate contrast based on differences in index of refraction, and so it is extremely difficult to extract quantitative biologically relevant information from the measured intensity at each pixel. With a few computationally-intensive exceptions where DIC can be used to determine dry mass [15, 16], phase contrast and DIC are basically qualitative imaging modes.

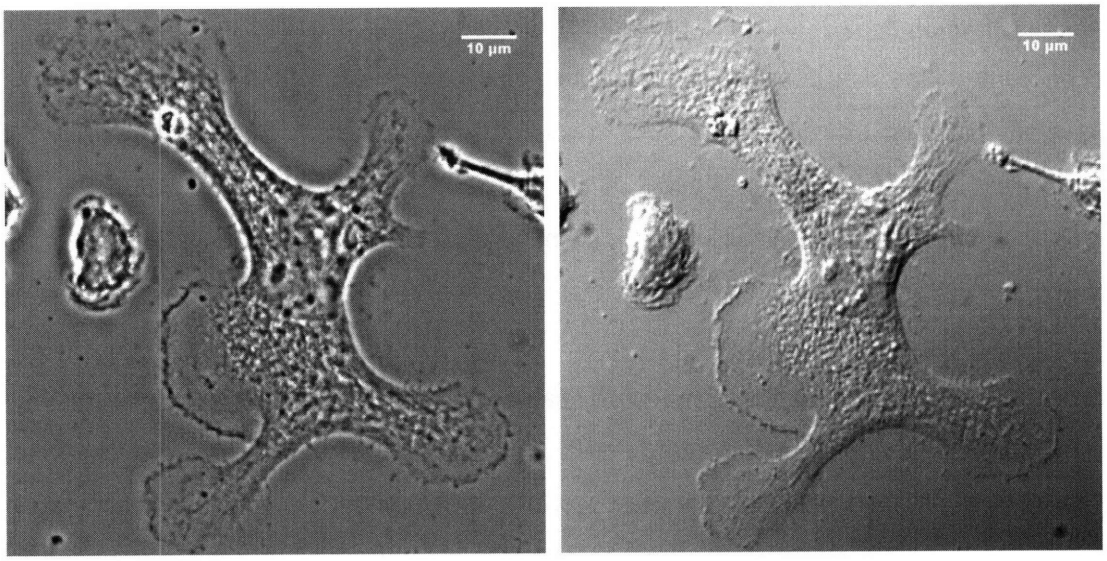


**Fig. 1:** Phase contrast and DIC images of a fixed, unlabeled IC-21 mouse macrophage cell.

### 1.3 Imaging at Deep Ultraviolet Wavelengths

A more quantitative approach to imaging without fluorescent labels involves generating contrast based on the intrinsic absorbance of two major cell components, protein and nucleic acid, at wavelengths shorter than 300 nm. Single-point (non-spatially-resolved) absorbance measurements at these wavelengths are ubiquitous in biological research, performed on isolated samples in solution using a spectrophotometer. These UV spectroscopy measurements are often used to determine molecular identity or concentration using well-established relationships like the Beer-Lambert law (also known as Beer's law) and to quantify the purity of samples [17]. Spectroscopy can also be performed on whole cells or microorganisms in solution to study changes in aggregation during growth [18] manifested as both absorbance and scattering. A further advantage of imaging at these wavelengths is that it provides higher spatial resolution according to the Rayleigh criterion.

Deep UV imaging was investigated as early as the 1930s, and these investigations seemed to peak around 1950. This early work is summarized in an excellent 1956 review [19]. Most of these efforts utilized film cameras for wide-field images; a few used basic photodetectors to make an electronic measurement at a single point. Much of the work at the time was conducted by T.O. Caspersson in Sweden, whose 1950 classic *Cell Growth*

*and Cell Function* [20] describes procedures that were as careful and quantitative as the technology of the day allowed. For instance, Caspersson took photographs at different wavelengths, then used a densitometer to quantify intensities in each photograph and reconstruct spectra for different areas of the cell in order to, for instance, compare the spectra in chromosomes to that in cytoplasm. After 1950, deep UV imaging work for biological applications seems to decline in frequency in the literature, in large part due to the complexity of the necessary equipment. We have reduced this complexity by using LED light sources and a UV-sensitive CCD camera as described in subsequent chapters.

One relatively recent paper [21] utilized a deep ultraviolet microscope to examine living plant cells. However, the shortest wavelength used was 300nm, and the apparatus was a fairly old Zeiss UV microscope described more fully in [22], a paper which also looks at living plant cells but only includes data taken at 310nm. The microscope used in both of these papers uses mercury and xenon lamp sources and a video camera recording to magnetic tape (not a CCD).

The most recent example of transmission deep UV microscopy on biological samples involved examining protein crystals with a UV-sensitive CCD camera and a xenon lamp source [23].

Work in a few similar areas also has relevance. UV microbeam irradiation was a technique used to intentionally induced damage in a localized region of a cell in order to then image and study this damage using other means [13]. Microspectrophotometers have also appeared in the literature; one group [24] used a deep UV microspectrophotometer to compare the absorption spectra in nucleolus, nuclear sap, and cytoplasm of living cells and fixed cells. There is at least one deep UV-capable microspectrophotometer commercially available (CRAIC Technologies, Altadena CA) with a motorized stage option and which can measure UV absorption as a function of position. This is designed as a single point measurement device and the sample would have to be slowly rastered by the stage. Such instruments are prohibitively expensive (over $100k), have limited spatial resolution, and may be too slow to capture events in live cells. Finally, deep UV wavelengths have been used to image semiconductors at high resolution [25] and major manufacturers including Zeiss, Leica, and Olympus have

all manufactured microscopes for this purpose; however these microscopes have operated in reflection mode rather than transmission mode and have not quantified absorbance.

### 1.4 Previous Work in Live-Cell Deep UV Imaging

The original UV imaging work in the 1950s required film, which necessitated a UV exposure level that quickly proved toxic to cells. As a result, Caspersson [20] concludes that *"the living cell is, as a rule, an unsuitable object for microspectrophotometric studies."* Walker and Davies also attempted live cell UV imaging using electromechanical shutters and a film camera. This setup necessitated 2.4 second exposures every 12 sec for 200 exposures, resulting in major changes in the nucleus; these same authors also report data in which they can only take 8 photographs of a cell at 280nm before damage occurs [19],[26],[27].

By the early 1960s some of these challenges were overcome as a result of developments in technology associated with television. Much of this progress was reported at a conference on "Scanning Techniques in Biology and Medicine" which took place in 1961 at the New York Academy of Sciences and was published in the Annals of the New York Academy of Sciences in 1962. One particularly relevant paper describes *"Instrumentation for Time Lapse Ultraviolet Television Microscopy"* that uses *"exposures of 0.01 sec."* or *"10 to 50 msec. open times"* and *"intervals of 3.2 sec. to 60 min."* for transmission imaging at 265nm onto a *"UV sensitive vidicon"* TV camera to image living cells with no *"evidence of change due to UV injury"* [28]. We independently developed the idea of using short exposures and longer recovery intervals to reduce UV toxicity prior to discovering this article. We can directly quantify values at each pixel using the CCD camera and computer, whereas the 1962 article described quantitation using an oscilloscope trace. The same proceedings describe a *"Vibrating-Mirror Flying Spot Microscope for Ultraviolet Spectrophotometry"*[29] that uses point scanning and a photomultiplier tube to scan a sample with a *"2-sec. over-all frame time"* in order *"to permit serial absorption measurements on living cells to be carried out without the induction of radiation damage artifacts."* The same authors describe advancements to this system in a later publication [30], now calling it a *"Double-Beam Vibrating Mirror Flying Spot Scanning-Integrating Microspectrophotometer."* They use UV light

(including 280nm) and raster it quickly across a sample in order to prevent damage to living cells, then reconstruct an image and calculate absorbances. Their abstract describes *"2 sec/frame"* but then on page 310 they say that *"The camera shutter remains open during the entire 1.6 sec scan duration, and closes for film advance during the vertical flyback time."* As the diagrams in these articles show, this was an extremely complicated piece of electromechanical machinery occupying a significant amount of space. This is perhaps the primary reason that this instrument never caught on. While the ultraviolet television microscope was a much simpler and more straightforward system, it still occupied a significant amount of space and calculation from the electronic signals was difficult. Our transmission imaging apparatus and methods allow for a significantly more compact setup and more direct quantitation.

### 1.5 Native Fluorescence Imaging

Light at these wavelengths can also be used to excite the intrinsic fluorescence of the amino acids tryptophan and tyrosine. Tryptophan has an absorbance peak around 280nm and a broad emission that peaks around 350nm. Like absorbance, protein native fluorescence is commonly measured at a single-point (non-spatially-resolved) for molecules in solution using a fluorimeter. Such measurements provide information about the environment surrounding a fluorophore. In particular, changes in the quantum yield are an indication that the environment around the fluorophore has been perturbed by events such as binding [31] or pressure [32]. Native fluorescence spectroscopy has also been used on whole cells in solution to determine differences between tumorigenic and non-tumorigenic cells [33].

For native fluorescence imaging there is also a small body of prior literature. Using a 305nm laser source with mechanical shutter, one group imaged the native fluorescence of serotonin in living cells at low magnification [34],[35]. They appear to have used the shutter to limit the exposure time of the cells to UV. They also explicitly chose 305nm in order to excite serotonin without exciting protein native fluorescence. Another group used a 280nm lamp source to produce low-magnification native tryptophan fluorescence image of protein crystals (not cells) [36]. We have improved on

these studies by producing 280nm excited, high magnification native fluorescence images of cells.

### 1.6 Previous Work in Protein and Nucleic Acid Mass Mapping

In spectroscopy, the A260/A280 ratio is a common measurement used to assess the purity of a protein or nucleic acid sample. It has also been applied to microspectrophotometry, and the Walker review describes 260/280 ratios measured on whole cells, albeit with significant noise [19]. Caspersson also used a Beer-Lambert law equation with contributions from protein and nucleic acid, at multiple wavelengths, to determine mass of protein and nucleic acid per area [20]. We independently developed extremely similar equations before seeing them in Caspersson's book, which is not surprising since they are fairly straightforward derivations from the Beer-Lambert law. It appears that Caspersson used film photographs taken at each wavelength, quantified the values in different regions with a densitometer, and used that to calculate masses. However, he did not do so at each pixel. By using a digital camera, we are able to determine the same resolution more quickly and accurately, and at higher spatial resolution. We believe that we are also the first to use the phrase "mass map" to describe the masses of protein and nucleic acid, calculated for and displayed at each pixel of an image. The need for such techniques was identified in a passage from James and Tanke discussing UV microscopy: *"A further disadvantage is that the absorption spectra of different cellular macromolecules (proteins, nucleic acids) show a large overlap"* [37].

### 1.7 Previous Work in Circular Dichroism Imaging

A third type of spectroscopy frequently performed at these wavelengths is circular dichroism (CD). By examining the difference in absorbance of left-circularly-polarized light and right-circularly-polarized light, it is possible to distinguish between alpha helices and beta sheets, and to see other structural changes. This technique has provided information about molecular structure for decades, and a search for "circular dichroism" on PubMed returns over 26,000 hits. Circular dichroism spectra appear frequently in the literature, including studies of the changes in spectra when DNA dissociates from a histone [38], when a histone is acetylated [39], and when chromatin is exposed to ethanol

[40]. CD can distinguish between solutions containing different DNA bases [41], and between different protein structures [42]. It has also been used in research on topics with medical relevance including studies of the beta-peptide associated with Alzheimer's [43], and interactions of metals with prions [44]. Virtually all of these studies were conducted with commercial CD spectropolarimeters.

Several groups have explored the use of circular dichroism to generate contrast for imaging, but none have successfully reported images at deep UV wavelengths. One group created a circular dichroism microspectrophotometer [45] which measured the circular dichroism of a single 6.3 μm spot on a sample at wavelengths down to 240 nm, but did not measure multiple spots or generate an image. The same researchers also created a differential polarization microscope capable of imaging circular dichroism, but only at wavelengths down to 400 nm, and using point illumination instead of a wide-field system [46]. Wide-field circular dichroism imaging has been reported at visible wavelengths by one group using synchronous detection with a CCD camera and a mechanically rotating polarizer to image crystals [47]. We believe that no one in the world has yet created true circular dichroism images at wavelengths below 400 nm – the very wavelengths that provide the most biologically relevant information. We have taken steps in this direction as described in subsequent chapters.

### 1.8 Previous Work in Polarization Modulation

Typical CD spectropolarimeters also utilize a photoelastic modulator (PEM) to modulate light between left and right circular polarization sinusoidally at a fixed frequency, usually 50 kHz. The light then passes through a sample and onto a detector, and the detector output is amplified at the modulation frequency to yield a signal related to the sample's CD. This synchronous detection method is necessary because the differences in absorption are very small. However, such modulators are expensive and bulky. Moreover, the fixed frequency of 50 kHz is too high for synchronization with most CCD cameras, which is why previous CD imaging efforts have resorted to mechanical modulation [47]. Obviously having mechanically moving parts is not ideal, both from a reliability standpoint and because of a lack of fine control. One solution to this general type of problem appears in a paper for the measurement of birefringence:

combining two orthogonally polarized beams modulated 180 degrees out of phase with each other, which travel along different paths that impart fixed polarizations, in order to produce a single beam of light that oscillates between two orthogonal polarizations [48]. As described in subsequent chapters, we have applied this concept to the measurement of circular dichroism, making a number of improvements and changes.

## 1.9 Previous Work in Native Fluorescence-Detected Circular Dichroism Imaging

Deep ultraviolet wavelengths are used to perform fluorescence-detected circular dichroism spectroscopy. Like circular dichroism spectroscopy, the sample is excited with left-circularly-polarized light and right-circularly-polarized light, but instead of measuring absorbance the resulting native fluorescence is instead measured. As a result, this method probes the circular dichroism specifically in the vicinity of native fluorophores – most notably tryptophan. This spectroscopy technique is not common but has appeared on several occasions in the literature [49].

While native fluorescence-detected circular dichroism appears in the literature as a spectroscopic technique used on samples in solution, we are not aware of any literature describing the use of this technique for imaging, and we believe we are the first to both propose and attempt this form of imaging.

## 1.10 Previous Work in Quantum Yield Imaging

Quantum yield is commonly measured in spectroscopy. It is also common to assess changes in the quantum yield of a fluorophore in visible fluorescence imaging, but we are not aware of any literature describing the actual calculation of quantum yield at each point in an image using transmission and fluorescence images, at any wavelength for native or artificial fluorophores. We believe this is the case because diafluorescence imaging, which is necessary to produce transmission and fluorescence images with the same field illumination, is extremely rare. We believe we are the first to produce true quantum yield images, at any wavelength.

## 1.11 Conclusion

Deep UV wavelengths are commonly used in biological research as part of the various spectroscopy techniques discussed here. These techniques provide quantitative, biologically relevant information at the cellular and molecular level. This thesis describes the development of apparatus and methods to make these same measurements as a function of position and time in a living cell. The results create a bridge between UV spectroscopy and live cell imaging, providing for the first time a viable means of quantitative live cell imaging without fluorescent labels. While deep ultraviolet imaging is a straightforward idea that has been previously explored by several investigators, these earlier efforts exposed significant challenges that prevented it from reaching its full potential. Building upon these previous efforts, our work has focused on overcoming the challenges to live-cell deep ultraviolet imaging.

## APPARATUS DEVELOPMENT

### Chapter 2: Deep UV Transmission Imaging Development

Our first scope design was an attempt to match the designs we had seen in the literature, modulated by what equipment we had available. The scope was based around a Zeiss upright Axioskop frame. We removed the condenser and condenser fork in order to inject light from a source adjacent to the microscope on the table as shown in **Fig. 2**. Like many of the efforts described in the literature, we utilized a mercury lamp (Oriel, Stratford CT) as a light source, coupled into a monochrometer (Oriel, Stratford CT) for wavelength selection. One issue was that the monochometer may have been out of calibration, so the actual output wavelength we were producing may have differed significantly from the indicated wavelength. The output from the monochrometer was reflected off a UV-reflective mirror (ThorLabs, Newton NJ) mounted underneath the stage and focused onto the sample using a biconvex fused silica lens (Esco Products, Oak Ridge NJ). Samples were mounted on quartz slides and coverslips (Chemglass, Vineland NJ). A 36X reflecting objective was used (Ealing, UK) – one of the few deep UV objectives which is still commercially available at a reasonable price (~$3k). For some images a 280nm bandpass filter with ~12% transmission at peak (Oriel, Stratford CT) was placed in the filter slider. Next, we replaced the standard Zeiss tube lens with a Zeiss quartz tube lens (45-29-61). The best camera we had available at the time was a Hamamatsu Orca 4742-95-12NR, which had approximately 10% quantum efficiency at 300nm. The manufacturer did not specify quantum efficiency at wavelengths shorter than 300nm, but extrapolation suggested a quantum efficiency of only ~3% at 280nm. The images in **Fig. 3** were acquired using this first design. They are extremely low magnification and few details are visible.

### 2.1 Light-Emitting Diodes

The next major change to the scope design involved replacing the mercury lamp and monochrometer with a light emitting diode (LED). The most dramatic effect was on apparatus size. The LED has a volume of ~0.357 $cm^3$ – more than four orders of

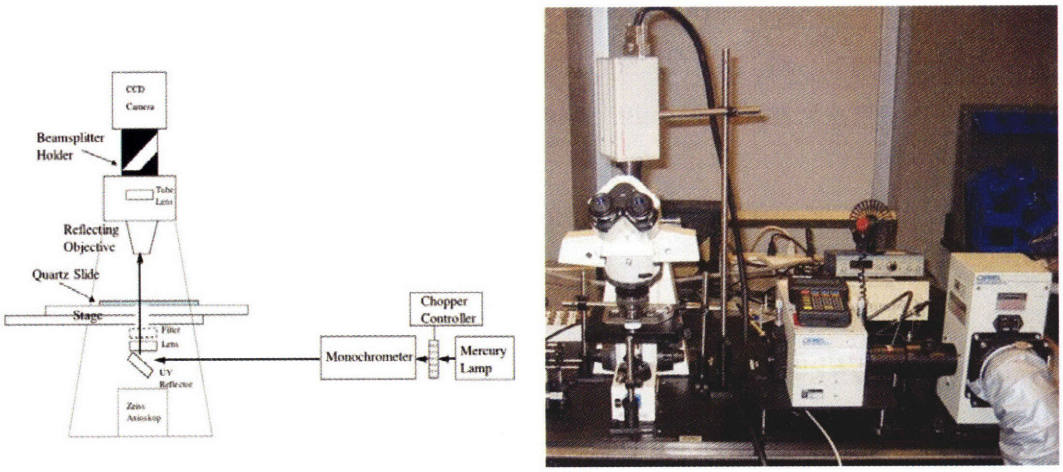


**Fig. 2:** Photo and diagram of our initial UV transmission microscope design.

magnitude smaller than the volume of our mercury lamp housing which has a volume of approximately 4588 $cm^3$ (not including the power supply or ozone scrubber or monochrometer). While visible wavelength LEDs have existed for years, deep ultraviolet LEDs only became commercially available in 2004. Much of the development work for these devices was funded by the Defense Advanced Research Projects Agency (DARPA) Semiconductor Ultraviolet Optical Sources (SUVOS) program. Key motivations include detection of biological warfare agents and covert communication, as well as water purification [50]. Deep UV LEDs are based on aluminum gallium nitride (AlGaN) and have been described in the literature [51]. They can be designed to have emission peaks at many wavelengths

**Fig. 3:** Images produced by our initial UV transmission microscope design.

between 250 nm [52], 278 nm [53], and 340nm [54]. LEDs can be modulated (turned on and off) very quickly, unlike lamps which depend on high energy arcs and heating and would be damaged by rapid switching on and off. While lamp output can be modulated with electromechanical shutters, direct modulation provides more precise control, reduces the complexity and cost of an instrument, and eliminates a potential failure point. Because of this flexibility, microscopes using LEDs can be easily adapted to new imaging techniques such as fluorescence lifetime microscopy [55]. While the mercury lamp does produce more wavelengths, the LEDs are also available with several different wavelength emitters in one package.

We obtained 280nm LEDs from Sensor Electronic Technology (Columbia, SC). Mounting the LEDs proved challenging. Our initial work with these light sources involved simply attaching them to an electronics breadboard, and then holding this breadboard in place with a chemistry-style clamp as shown in **Fig. 4**. Obviously this was not stable enough, nor did it provide sufficient flexibility for alignment. The LEDs came in fairly standard TO39 packages, yet we had difficulty finding an appropriate mount for these packages, particularly one that would interface well with our ThorLabs cage systems and SM1 style optical mounts. Initially we used a ThorLabs mount (S1LM9) designed for 9mm laser packages. While the LED did fit in this mount, it could not fit in all the way because its back lip was too wide, so we could not use the threads to attach the LED. For some time we solved this problem by using a space filling gel-type super glue (Locktite Super Bonder Quick Gel 409) to secure the LED in place as shown in **Fig. 4**. While this approach was effective, it presented a significant risk that the LED would become misaligned, especially since there was pressure on the leads from the connector. It was also difficult to make sure the LED was perfectly straight during the gluing process. We were helped in this regard when our LED supplier altered the packaging to be a slightly flatter version of the TO39 package. Using the same S1LM9 mount, and bending back the tab on the LED with pliers, we were able to push the LED snugly into the mount so that the window was flush with the mount as shown in **Fig. 4**. We could also then screw in a retainer to hold it in place, although the fit was so tight that this was usually unnecessary. After mounting, we connected the LED leads to a small piece of breadboard to which we had already connected a BNC cable.

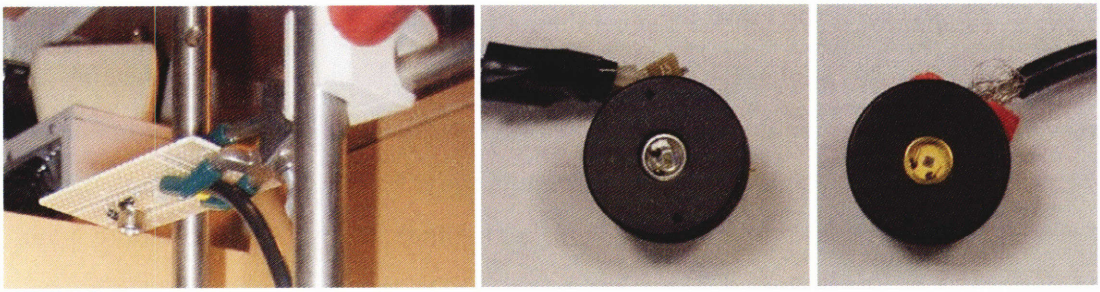

**Fig. 4:** Evolution of LED mounting procedures. (**a**) Chemistry-style clamp. (**b**) Glued into S1LM9 mount. (**c**) Fitted into S1LM9 mount.

Developing circuits to drive the LEDs was also challenging. Each of the drivers was constructed by Roger Lam after we extensively discussed the requirements. The most basic driver circuit utilized a high-current Darlington sink driver (TD62064 Toshiba, Japan) powered by a 24V power supply, along with a pair of rectifiers (1N4007, Micro Commercial Components, Chatsworth CA) and some resistors to drive the LED at the desired current in response to a TTL input signal. See wiring diagram and photo in **Fig. 5**.

For version 2 of the microscope, in addition to replacing the lamp with an LED, we also improved the condenser by the additional of a second biconvex fused silica lens to serve as a collector lens in front of the light source. We also repositioned the lens serving as the condenser. These changes improved the magnification of the system. A diagram of this second version of the microscope, and representative images from it, are shown in **Fig. 6**. We also made our first attempt to overlay visible and UV images by replacing the LED with a mounted Mag-Lite flashlight, but we found that the images differed

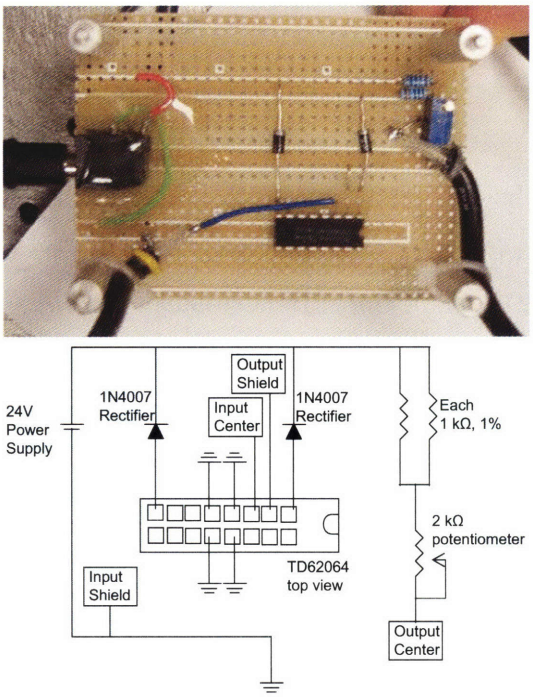


**Fig. 5:** Wiring diagram and photo of our TTL-activated LED driver circuit.

significantly due to the different size and shape of the emitter elements. This issue helped lead us in the direction of fiber optics as discussed below.

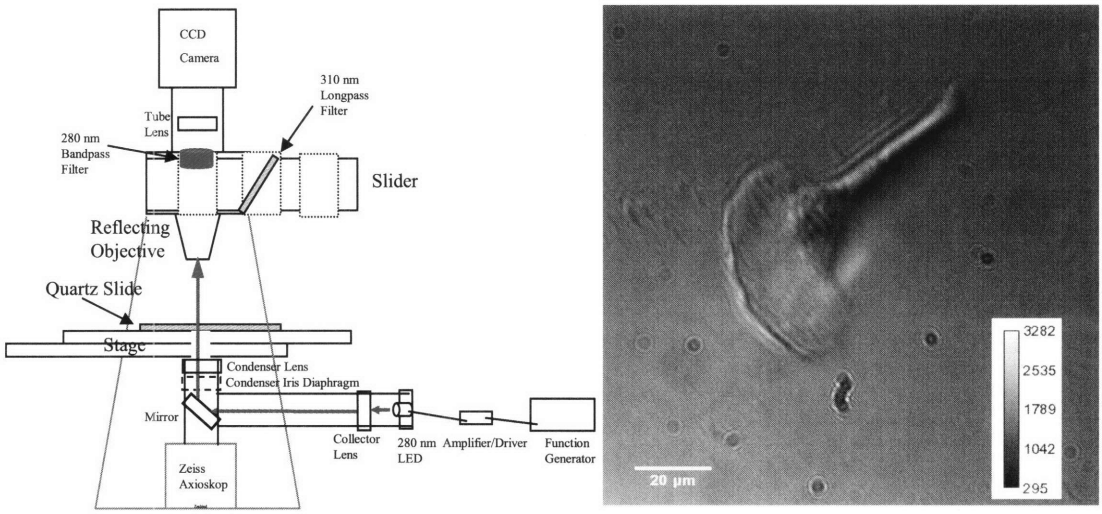


**Fig. 6:** Diagram of, and image produced by, our second UV transmission microscope design.

## 2.2 Condenser

The next version of the microscope showed significant improvement as a result of important input from Shinya Inoué. Having assessed the data and design of version 2, he correctly ascertained that our condenser was the limiting factor on image quality and magnification. He then very generously loaned us a Zeiss UV-Kond Achromat 0.8 (58-829) condenser. This condenser has standard RMS threads, but we did not have an RMS thread adapter to fit in the Zeiss condenser fork (although we believe Zeiss did manufacture such an adapter at one point). Instead, we used a Zeiss dovetail designed to hold standard 25mm diameter parts, and mounted in it a ThorLabs SM1-to-RMS (SM1A3) adaptor. This seemingly simply mechanical adaptation was incredibly useful, because it allowed us to mount the condenser stably in the condenser fork with x,y, and z adjustment capabilities, and also because on the other end we were able to attach an RMS-to-SM1 adapter (ThorLabs SM1A4) which then enabled us to connect standard SM1 threaded parts to this optical train.

As part of the same design iteration, we also eliminated the right angle geometry that had been used to introduce excitation light, since the mirror caused some loss and

also provided an additional surface that required alignment. Instead, we removed the base plate of the microscope in order to create a straight path with more room for modification. We removed the iris and the mirror in the transmitted light path. In order to take advantage of this newly lengthened straight light path, we had to actually hang the microscope off the end of the optical table. Although we were able to fasten it down securely, this still reduced the stability of the scope somewhat. However, the design flexibility that it provided turned out to be worth the tradeoff.

With these improvements, we were able to connect a cage system underneath the condenser and mount an LED on those rails so that it illuminated straight up through the path. This was extremely efficient and provided a very high signal-to-noise ratio. The combination of the condenser and the new geometry significantly improved the magnification of the system and eliminated some of the ringing artifacts that had plagued previous designs. This design, and data from it, are both shown in **Fig. 7**.

However, having the LED mounted as part of the condenser system had several painful drawbacks. Changing the LED required realigning the optical system. The shape of the emitter element from the LED also had an effect on the images. And it was impossible to switch wavelengths by switching LEDs, without a lengthy mechanical process. This arrangement was therefore not modular and not sustainable.

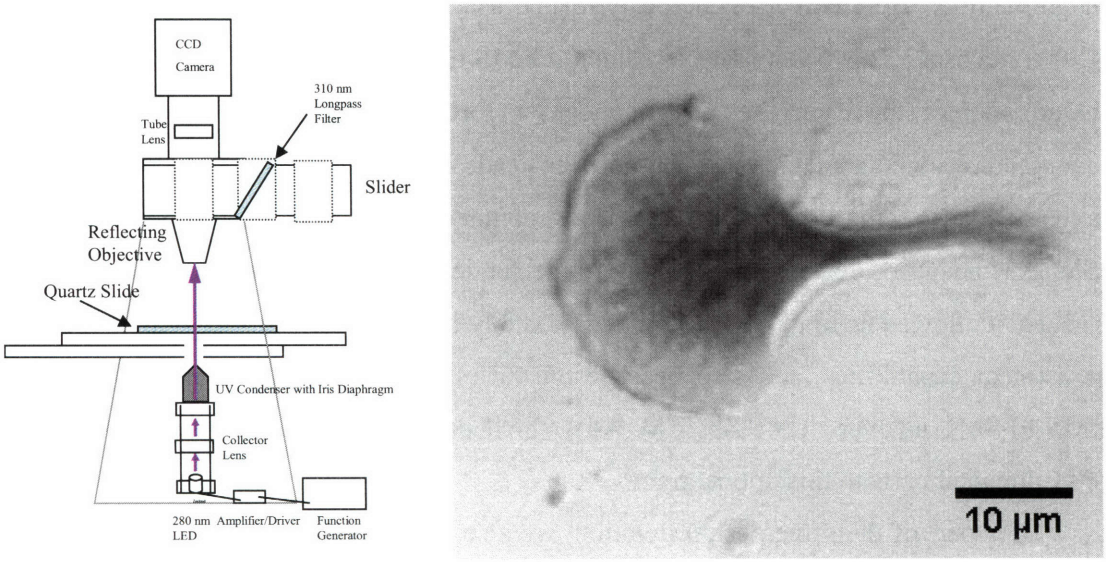


**Fig. 7:** Diagram of, and image produced by, our straight-through UV transmission microscope design with the new condenser.

## 2.3 Fiber Optic Input

The solution to this lack of modularity came in the form of an excellent suggestion from Matt Lang, who advised us to couple the light source into the scope using a multi-mode fiber. We obtained 0.22 NA high OH graded index multimode fiber from ThorLabs (BFH22-910) with reasonably high transmission below 300nm and a large (0.91mm) core diameter. The fiber had standard SMA connectors which we could easily interface to cage mounts and SM1 tubes using an SM1SMA adapter. We found that simply close-coupling the fiber to the LED was adequate, although we also built more complex coupling assemblies with x-y translation for the LED and lens, and z-translation for the fiber. However, we found that this only led to a small improvement over close coupling. The LED manufacturer also offers pigtailed LEDs but at a significantly higher cost, so we did not explore this option. The fiber may have helped eliminate the coherence effects that were a possible cause of some of our ringing artifacts. Conceptually, the fiber represented an abstraction barrier between the light source and the microscope, allowing us to switch between different LED light sources or even use visible lamps, all while having the light enter the optical train of the microscope at a constant position and relatively constant size and shape. From a practical and mechanical point of view, the fiber allowed us to set up our light sources in a convenient location near the scope with plenty of room, rather than trying to force them into a position dictated by the optical train. Overall, the fiber was a huge step forward.

Around the same time, we incorporated a polarizing beamsplitter cube/pickoff device (described in chapter 5) to our setup. The scope arrangement with fiber input and this polarizing beamsplitter cube, and an example image, are shown in **Fig. 8**.

## 2.4 Ultrafluar Objective

The next key iteration to the scope involved the objective. Up to this point, all the images were taken with an Ealing 36X reflecting objective. We wanted higher

magnification in order to study chromatin effectively and to realize the spatial resolution benefits of deep UV light. Moreover, the reflecting objective had a very low NA (0.5) and introduced some aberration into our images. Finally, meeting with Shinya confirmed that such an objective would not be effective for polarization work since reflection off the curved mirrors would introduce significant artifacts. Prior literature suggested that the Zeiss Ultrafluar objectives had been extremely effective for deep UV, but all Zeiss had available for sale was a 10x for $4.9k and a 100X optimized for 360nm-370nm for $14.2k. Neither of these were appealing options. We then got quotes from the major microscope companies for their DUV objectives made for semiconductor work. Leica quoted us $130k for a 200X objective and $25k for a 150X, both of which were monochromatic and designed for 248 nm. Olympus has a 100X DUV objective for $30k. Optics for Research had a few UV objectives, but these had very low NA (0.5 max) and seemed to be designed for laser focusing rather than imaging. Shinya Inoué graciously

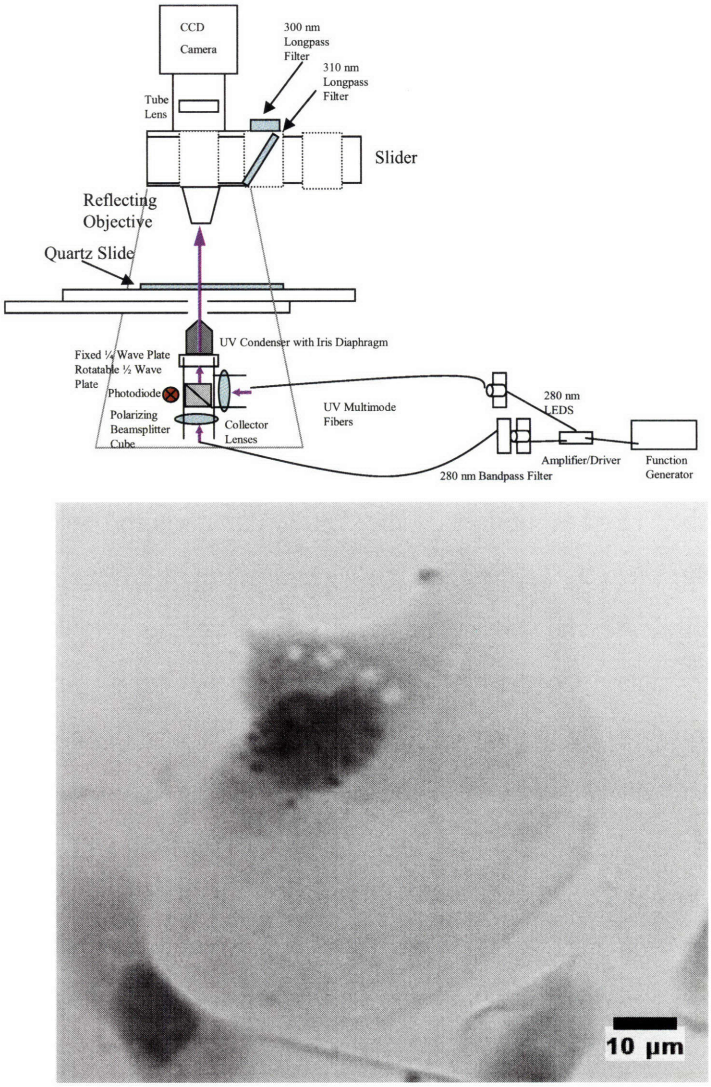


**Fig. 8:** Diagram of, and image produced by, our UV transmission microscope design with fiber optic input and the polarizing combiner condenser.

loaned us a Leitz 300X quartz objective with a 0.85 NA, but the transmission was low at 280nm. After investigating various options, it still seemd that the Zeiss Ultrafluars were best. Calls to a variety of microscope resellers and specialty vintage shops only confirmed what we already knew: that these objectives were extremely difficult to find. Finally, in desperation, we set up alerts on eBay to notify us when an Ultrafluar was up for sale. Just a few weeks later, we received notice that both a 100X and a 32X Ultrafluar were available. Despite a flurry of last minute bids from others, we managed to win the 100X auction with a bid of $394. We just barely lost the 32X with a bid around the same amount. In retrospect we should have bid much higher for both!

The 100X Ultrafluar (46-20-64) arrived a few days later, in pristine condition. It was a 1.25NA glycerol immersion designed for a 160mm tube length. Although our system was designed for infinity-corrected objectives, we were still able to focus an image – we just had to use a different working distance. While the reflecting objective had been an air objective, this one required glycerol immersion media so we obtained spectrophotometric grade glycerol (Acros, Belgium) to ensure high transmission in the UV. The resulting images were sharper and better focused than those taken with the reflecting objective, and of course the magnification was higher. There were some drawbacks – in addition to the drastically reduced working distance, this objective also seemed to accentuate an artifact – a bright white spot in our images. Nevertheless, the Ultrafluar was a tremendous improvement over the reflecting objective. See **Fig. 9**. We also later obtained an older 100X Ultrafluar (10-11-19) on eBay as a backup, but it had poorer image quality.

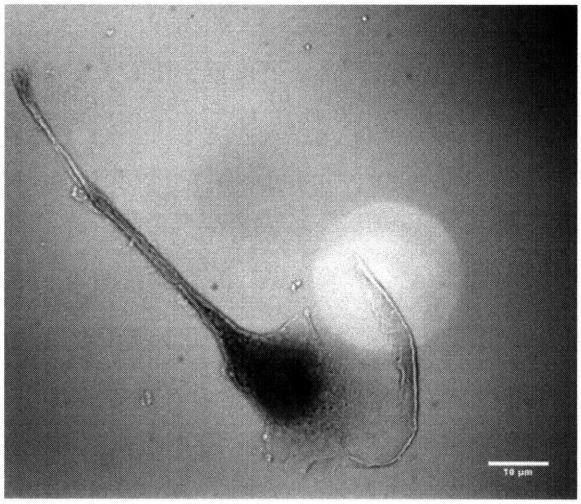


**Fig. 9:** Image produced by our UV transmission microscope design with the Ultrafluar objective.

## 2.5 CCD Camera

We had long been aware that our Hamamatsu Orca 4742-95-12NR camera had dismal quantum efficiency in the UV – we estimated only ~3% at 280nm. However, replacing the camera required a significant investment – over $20k. We developed one lower-cost option based on an old Princeton Instruments MicroMAX camera that had been generously loaned to us from the microscope facility by Nicki Watson. While this camera had zero quantum efficiency below 400nm, we discovered that the Princeton Instruments service department was willing to apply a UV coating to the camera for a cost of approximately $2k. This would give ~10% quantum efficiency at our wavelengths of interest. While we did not end up following this route, it could be extremely useful for a lab starting a UV imaging program on a tight budget.

We also had access to a fairly old and low quality image intensifier. While there are intensifiers available that can take UV images as input and produce visible output, the one we tested induced a honeycomb pattern. While it is possible that higher quality image intensifiers could be useful for deep UV imaging, we did not choose to follow this route either.

Fortunately, we had written and received a grant from the US Air Force Office of Scientific Research for "Deep Ultraviolet Laser Imaging for Biology," (PI Dan Ehrlich) and we were able to use some funds from this to acquire a new camera. Selecting a camera was approximately a 5-month process. In addition to high UV sensitivity, we also wanted a camera with relatively small pixels (so we could achieve high spatial resolution images) but we also wanted high signal-to-noise ratio (so we could measure small differences in intensity from different polarizations) which meant a large full-well capacity and small read noise. There was a tradeoff here since smaller pixels have a smaller full-well capacity. Speed was also a factor – we wanted a camera that could image at a rate faster than 10Hz in order to do synchronous detection with our polarization modulator, and to take extremely short exposures to minimize UV toxicity. We narrowed the search down to three manufacturers – Princeton Instruments/Photometrics, Andor, and Hamamatsu. See **Table 1** for our comparison of the specifications. While the Hamamatsu camera had higher quantum efficiency, it also had larger pixels and slower speed. We felt that the Andor or PI PhotonMAX cameras

were more versatile. These cameras also had both traditional amplifiers and electron-multipliying CCD amplifiers which had potential for the native fluorescence measurements discussed later. The Andor and PI cameras had similar specs, but we had positive experience with PI support in the past, and PI was more aggressive in lowering the price. We therefore chose the PI PhotonMAX 512B/UV camera.

| Company | Princeton Instruments | Photometrics | Andor | Hamamatsu |
|---|---|---|---|---|
| Product | PhotonMax 512B/UV | Cascade 512F | DV887-ECS-UVB | C4742-98-26LAG |
| QE | 35%, 200nm-350nm | 12%, 200nm-350nm | 35%, 200nm-350nm | 42%-60%, 200nm-350m, |
| Frame Rate (full frame, no bin) | 29FPS (full frame, no bin) | 29FPS (full frame, no bin) | 35FPS(full frame, no bin) | 6.34FPS (high speed readout) |
| Controller/Software | PCI Card, WinXTest | | | |
| Well Depth | 200k traditional, 800k gain | 200k traditional, 800k gain | 220k,800k | 230k |
| Read Noise | 8/15 traditional, 45/60 gain | 10/15 traditional, 45/60 gain | 7/22, 45/62 | 7 (highprecision readout) |
| Pixel Size | 16umx16um | 16umx16um | 16x16 | 24x24 |
| Array Size | 512x512 | 512x512 | 512x512 | 512x512 |
| Special Features | On Chip Multiplication Gain | On Chip Multiplication Gain | | |
| Digitization | 16-Bit at 10Mhz,5Mhz,1Mhz | | 14bit,16bit@1Mhz | 16 bit at high precision, 12 bit high speed |

**Table 1:** Comparison of UV camera specifications.

The camera was well worth the investment. The order of magnitude improvement in quantum efficiency was noticeable in higher signal to noise ratio and improved image quality. The camera also had BNC inputs which allowed us to trigger it from external sources and also BNC outputs that allowed us to trigger the LEDs from it. These features gave us increased control over the timing. Finally, the expanded wavelength range allowed us for the first time to image at 260 nm. **Fig. 10a** shows the old camera after a 10 second exposure at 280nm, while **Fig. 10b** shows the same cell imaged on the new

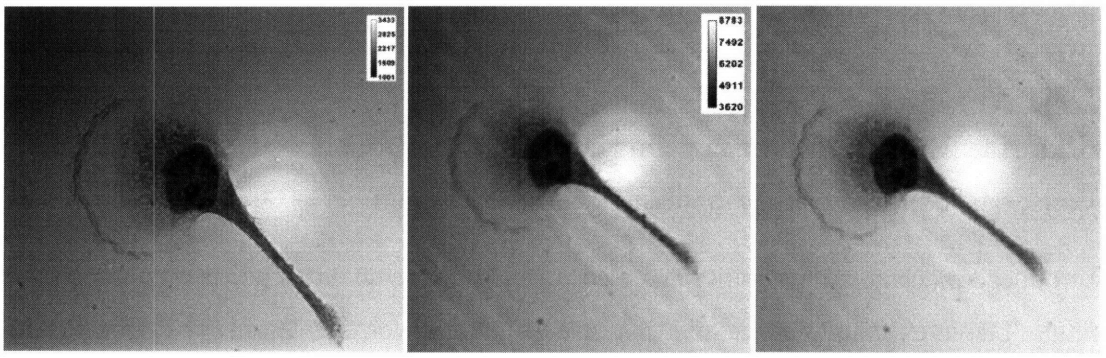


**Fig. 10:** (**a**) 280nm transmission images acquired by our Hamamatsu camera with a 10 second exposure, (**b**) and by our new PhotonMAX camera with a 500ms exposure. (**c**) 260nm transmission image acquired by our new PhotonMAX camera. The PhotonMAX images have higher intensity due to the increased quantum yield, but less detail because the chip is 512x512 16μm pixels as opposed to the 1200x1024 6.7μm pixel chip in the Hamamatsu.

camera for just a 500ms exposure – demonstrating significantly higher intensities (although slightly poorer focus). **Fig. 10c** shows a 260nm transmission image of the same cell taken with the new camera, a wavelength not achievable with the old camera. One drawback to the change was that our old camera had 6.7μm pixels on the chip, while the new one has 16 μm pixels. So our pixel size went from 79nm to 190nm. In anticipation of this problem we had designed a fused silica transfer lens and tube to go before the camera in the optical train which was able to approximately double the magnification as determined with a Ronchi ruling and shown in **Fig. 11**, but this system

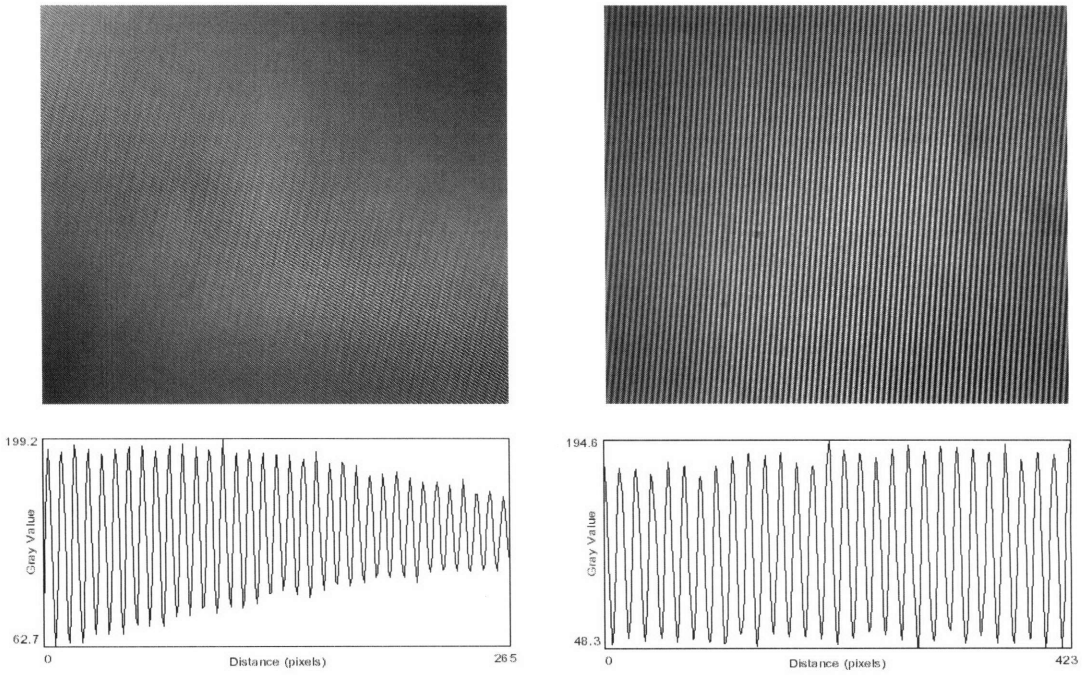


**Fig. 11:** The improvement in magnification from our fused silica transfer lens, as illustrated on a Ronchi ruling with 600 lp/mm.

introduced mechanical instability and also reduced image quality since it was based on a single biconvex lens, so we did not use it. However, we partially corrected the magnification problem by removing the tube lens as described below.

We are also constantly evaluating new camera systems that may help improve our microscope. Hamamatsu does offer a camera (C4742-98-26LAG) with a QE peak of ~85% at ~250nm, but this camera has 24μm pixels which would significantly degrade our spatial resolution with the current magnification system. Sarnoff Imaging (formerly

RCA Labs) is launching a camera in April 2006 (1m-30-FT) that has a QE of 50%-80% throughout the deep UV, down to wavelengths as short as 193nm, and 10μm pixels which would actually improve our spatial resolution. Drawbacks are that it is only 12-bit, noise may be higher, and there may not be well-developed software to run it. Nevertheless, the high QE and small pixel size would be an improvement over both our current camera and Hamamatsu camera.

### 2.6 Increased Wavelength Flexibility

The new camera allowed us to expand our range of wavelengths to those shorter than 280nm. Shortly before the new camera arrived we had acquired a 260nm LED, and the new camera allowed us to image at this wavelength with the same QE as at 280nm. We also acquired and set up LEDs at 320nm and 340 nm in order to do scattering correction as discussed later.

### 2.7 Improved Filter Technology

It was necessary to include a filter directly before the camera in order to block any native fluorescence and also to block out the small amount of visible light that the LEDs appeared to also emit. Initially we had been using a 280nm bandpass filter from Oriel with a transmission efficiency of ~12% and a 260nm bandpass filter from Melles Griot with a similar transmission efficiency. However, after fully exploring our situation with Chroma Technology, we were able to obtain a 280/20x bandpass filter that had nearly 50% transmission at 280nm, and ~10% transmission at 260nm. This was better because it allowed us to use the same filter at both wavelengths, reducing artifacts due to different coatings and thicknesses. The 4X improvement in 280nm transmission allowed us to significantly reduce our exposure time. However, these transmission efficiencies are still not ideal. We have just received a 290sp filter from Chroma with better than 65% transmission at 260nm and better than 75% transmission at 280nm, with an average OD3 between 300 and 390nm. However, the problem with this filter is that it has high transmission about 400nm, which means we will need to combine it with a second filter – we have obtained a 400nm shortpass filter from Edmund Optics for this purpose but this two-filter combination may introduce reflection artifacts as well as distortion from the

thickness of material. We also tried an ACT5 filter from International Light and a Corion ion-plated water purifying filter from Newport, but both allowed significant leakage at visible wavelengths. Recent literature includes several new technologies with promise for UV filtering. These include silver-silica transparent metal structures [56] and macroporous silicon structures [57]. The latter are being developed by Lake Shore Cryonics, and are not yet ready for commercial sale. A personal communication [58] revealed that they have a theoretical transmission of 18% and have a theoretical transmission of 45%. Perhaps the long-term solution may be a custom-made UV shortpass filter. Barr Associates quoted us such a filter (with an average transmission greater than 80% from 270nm-300nm, and an OD3 or greater from 320-700nm). However, the $6.5k price is a significant drawback.

### 2.8 Removal of Tube Lens Improves Magnification and Eliminates White Spot

With all the aforementioned developments the scope was producing very high quality images, but they still suffered from a serious white spot artifact as seen prominently in **Fig. 12**. To eliminate this spot we systematically removed each part of the optical train to see what effect it had. We removed the polarizing beamsplitter and left it out, replacing it instead with additional apertures to more closely approximate Koehler illumination. However we could not exactly replicate Koehler illumination because of a slight angle problem in the mechanical mounting which meant that when the scope was set for Koehler the field was not uniformly illuminated. We therefore set up the scope for Koehler illumination and then adjusted the condenser again for uniform field illumination. In any case, these changes did not eliminate the white spot. Finally, we reached the last component in the optical path – the Zeiss quartz tube lens. Removing this from the path eliminated the white spot artifact as seen in **Fig. 12**. We believe this spot was a result of a reflection. In retrospect, the tube lens was not necessary since we use a fixed tube length objective. Moreover, removing the tube lens also doubled our magnification, so while the pixels were previously 190nm they became 92nm. This change allowed us to realize the spatial resolution benefits of deep UV wavelengths. Removing the tube lens was a big win overall, but we did pay a price in terms of reduced working distance, just barely enough to focus through a 0.25mm coverslip. This is

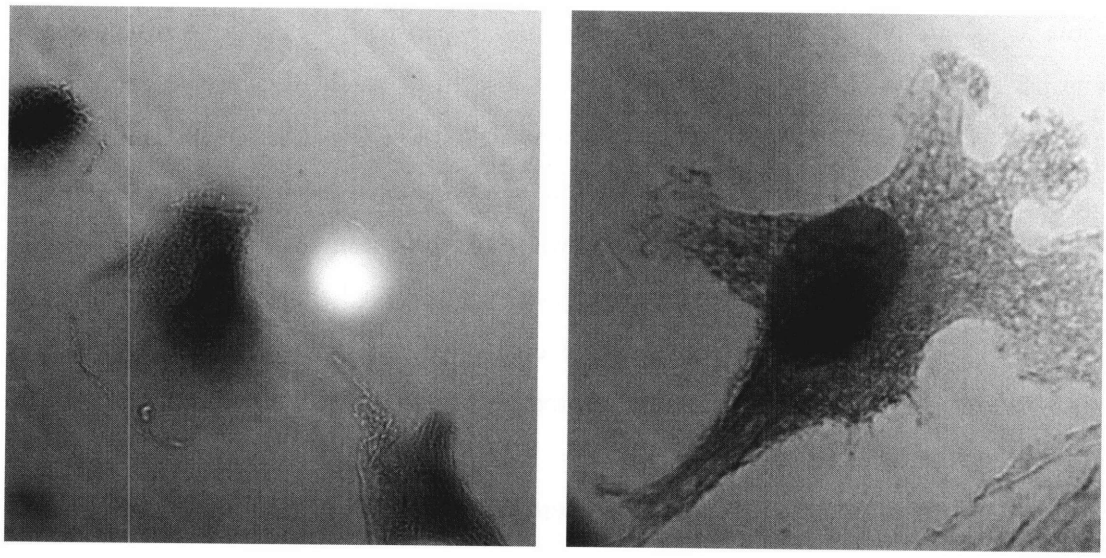

**Fig. 12:** Images of different cells immediately before removal of the tube lens showing the white spot artifact, and immediately after removal of the tube lens – showing no white spot.

because the objective is being used with a much longer tube length (over 300mm) than the 160mm tubes for which it was designed. This may also introduce some chromatic aberration.

From the standpoint of optics, eliminating the white spot was the last key step for transmission imaging. More hardware work was done to adapt for live-cell imaging, as described in chapter 5. A number of improvements currently in progress are described in chapter 13. A few general issues, not directly related to the optics, required significant attention and contributed to the effective use of the microscope.

### 2.9 UV Safety

Our initial focus was on preventing UV exposure to eyes and skin. We obtained UV safety goggles (Oriel 49126) with low transmission below 375nm, and very high transmission above 400nm. This allowed us to have unimpeded vision, a major improvement over some UV goggles which also have significant attenuation in the visible spectrum. To protect facial skin from UV exposure we used a polycarbonate face shield (McMaster-Carr) since polycarbonate is known to have low UV transmission. We obtained UV protective gloves (Oriel 49123), although these appear to just be made of

black polypropylene and could be obtained less expensively. Finally, to protect skin on arms, sleeves were rolled down (or in the case of short-sleeve shirts, a lab coat was worn). This protective gear was worn whenever the UV was on. For the UV amplifiers that were triggered by a TTL pulse, we initially considered the LED to be off as long as there was no TTL input. However, there was one incident in which an LED remained on in the absence of a TTL pulse, possibly because of a signal shorted by the metal optical table. As a result of this incident, we connected the LED amplifier to a separate powerstrip, and took all appropriate UV precautions whenever the powerstrip was on, not just when the LED was triggered.

While these safety precautions were necessary, they were also bulky, hot, and uncomfortable. Combined with a dark room necessary for sensitive measurements, it had a sensory deprivation effect which made experiments unpleasant. A few initial attempts at imaging samples with collaborating colleagues revealed that this uncomfortable experience was actually discouraging collaboration. This problem was solved in an unexpected way. Around the same time another colleagues was moved into the same room, which meant that we had to obtain an optical curtain to split the room optically so that we could do dark or light experiments independently. Working with the Kentek Corporation, we designed a custom curtain that would completely seal the two halves of the room – sealing against the walls and bench with Velcro. The curtain ran along a track that needed to be connected to the wall at either end, and to the beams above the suspended ceiling in the middle. While it seemed like a simple job, installing it properly took an entire morning for the work crew. With the curtain installed, we were able to move the computers controlling the scope outside the curtain, along with the powerstrip controlling the LEDs. An experiment could be set up and the curtain closed, then from the outside the operator could activate the LEDs and run the experiment. While a seemingly simple change, this modification made experiments much more comfortable (and safer) for the operator and collaborating colleagues.

One drawback of the curtain was its effect on ventilation. The thermostat sensor and air output were on one side of the curtain, and the air intake was on the other side. The curtain sealed so well that it actually created two separate rooms in terms of air circulation. This situation exacerbated the already poor temperature control in the room,

creating a significant gradient which led to air currents every time we opened the curtain and undoubtedly exacerbated our focus drift problems. Although there was little we could do about it in our room, it is an issue to be aware of when designing such facilities in the future. Another problem was more easily solved – we subsequently had to have electricians wire separate switches for the overhead lights on either side of the curtain.

We also went to great lengths to obtain an optical table. This is important for eliminating vibration – particularly between multiple images which we overlay, and for images taken with long exposure times. Our lab had tables in a warehouse which we visited to inspect and found that they were 4 feet by 8 feet. This was too big to fit in the elevator. Our original plan was to remove the window from the room and crane the table in, but this was going to be extremely costly because the old windows were expensive and had to be insured. Ultimately, the riggers brought the table in via the elevator shaft, connecting it underneath the cab. The size of freight elevators and difficulty of removing windows are important factors to keep in mind when situating/constructing a research facility.

## Chapter 3: Native Fluorescence Imaging Development

### 3.1 Version 1

We first attempted to implement native fluorescence imaging in an epifluorescent arrangement, using a very thick UV reflecting slab as a crude dichroic. In order to mount this on the scope, we designed and had machined a custom beamsplitter holder to replace the phototube on the Axioskop. A photograph of this beamsplitter holder on the scope appears in **Fig. 13**. While the design served as an effective interface between the microscope, camera, and beamsplitter, it suffered numerous problems. First, the beamsplitter itself had no provisions for mounting the excitation LED, so we had to mount that separately on optical rods. As a result, it proved very difficult to mount the LED in a stable way and to position it perpendicular to the beamsplitter holder. Additionally, this beamsplitter holder was developed when we were using an extremely small and lightweight camera and so it was not designed to provide significant mechanical support. When we attempted to use a heavier camera with this arrangement it presented concerns both of mechanical vibration and also that the beamsplitter holder would actually snap at its weak point. The beamsplitter itself was an ultraviolet reflecting long pass filter (Oriel 66217) which was 6.4mm thick. This was not an effective dichroic for imaging because its thickness introduced distortion into the images. It was also made of crown glass, so it is possible that wavelengths at the reflection/transmission cutoff around 335nm could induce autofluorescence in the material itself. Finally,

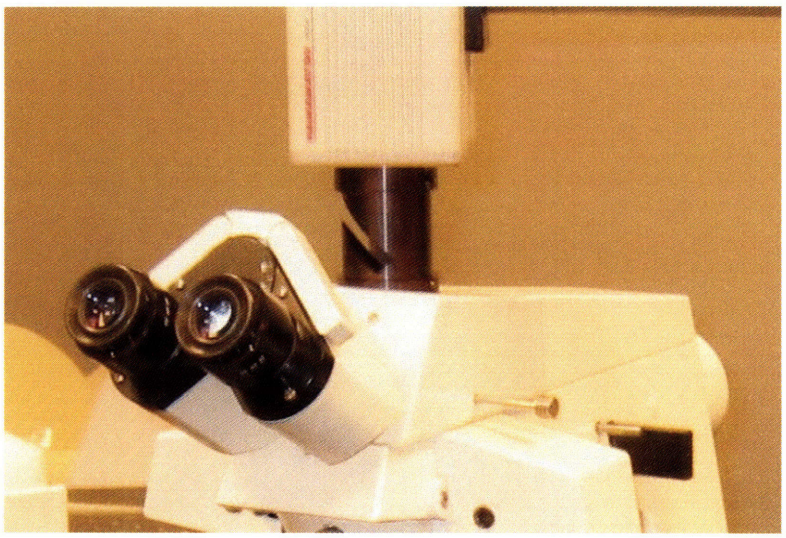

**Fig. 13:** Photo of our initial beamsplitter design for native fluorescence.

because this mount did not fully enclose the beamsplitter, a significant amount of stray light could leak in (even in the darkened room), hindering our ability to measure very weak autofluorescent signals. While we were able to image some lyophilized proteins with this arrangement (see **Fig. 14**), it clearly was not a sustainable or effective solution.

### 3.2 Version 2: Inverted Scope.

To circumvent these issues completely, and to avoid tying up the scope which was becoming increasingly useful for transmission imaging, we next attempted to set up native fluorescence imaging on a separate scope – a Zeiss Axiovert 10. The work at this point was helped by the efforts of a persistent and talented UROP student, Caroline Jordan. We attempted to use oblique flood illumination – focusing the LED output onto the sample from below and beside the microscope. However, directing this light onto the sample proved impractical because it required a mirror to be placed at an odd angle near the scope turret. Next, we attempted to flood illuminate obliquely from above the stage, but in this case the presence of the condenser meant that we had to use

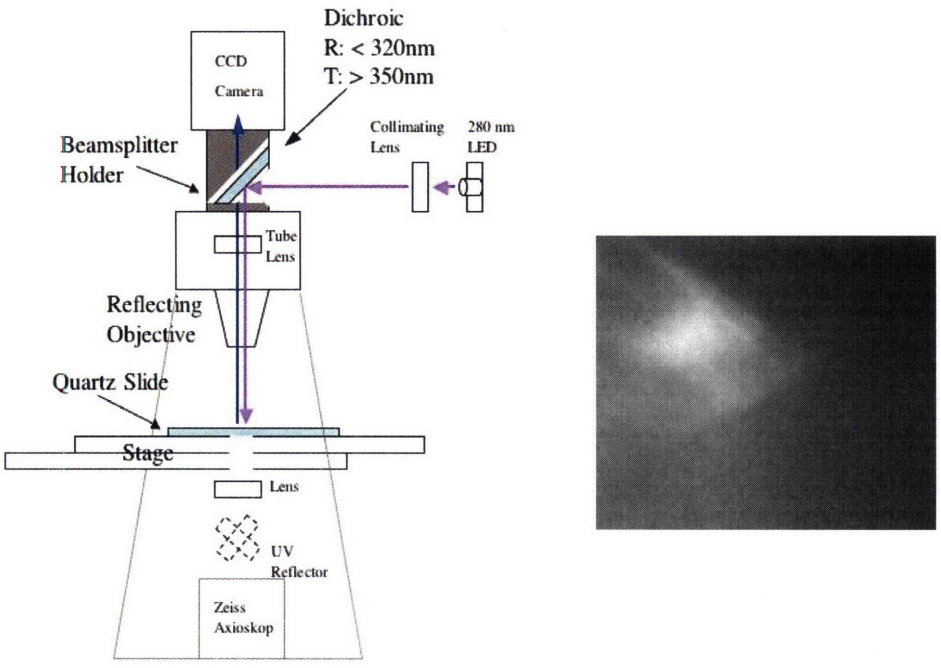


**Fig. 14:** Initial design of native fluorescence scope, and image of lyophilized proteins taken with this scope design.

a very steep angle which was ineffective. Caroline then suggested removing the condenser, which we were not using at that point, in order to have a less obstructed illumination path. This unexpected solution finally enabled us to focus a significant amount of excitation light onto the sample. This change improved our signal-to-noise ratio enough to begin seeing the outlines of cells, but the signal was still extremely weak. A chance discussion with the prior users of the scope revealed that the transmission, even in the visible was somewhat poor. This was likely a result of corroded and dirty surfaces on the aging scope. Moreover, this inverted microscope had a pentaprism which most likely had poor transmission even at the near-UV wavelengths of tryptophan autofluorescence. While characterizing the exact transmission of this microscope at various wavelengths proved challenging, our results were sufficient to convince us that further native fluorescence work should be pursued on the Zeiss Axiokop upright – the same microscope we were using for transmission imaging.

### 3.3 Upright with Oblique Bottom Illumination

Indeed the upright proved to have dramatically higher signal. The key lesson here is that native fluorescence is best imaged on a deep UV scope, since a significant portion of the emission is below 350nm and thus cut off by visible light scopes. We first attempted this flood illumination from below the stage. A photograph, diagram, and image of onion cells from the resulting scope are shown in **Fig. 15**.

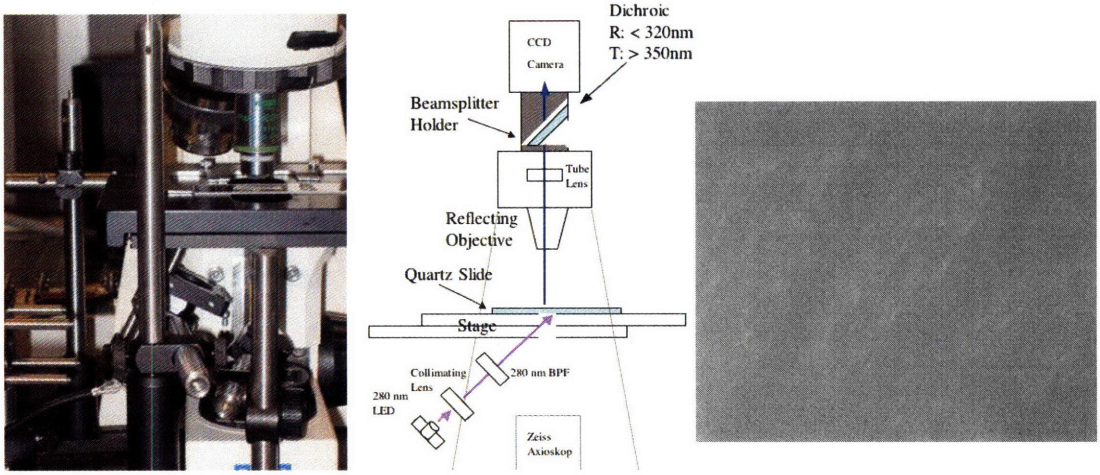


**Fig. 15:** . A photograph, diagram, and faintly visible image of onion cells from our native fluorescence scope with bottom oblique illumination.

### 3.4 Upright with Oblique Top Illumination

Illuminating from the bottom proved difficult because the condenser obstructed the light path and also the bottom portion of the stage blocked incident light. So we tried illuminating from above which was more successful. We were able to use 1 LED

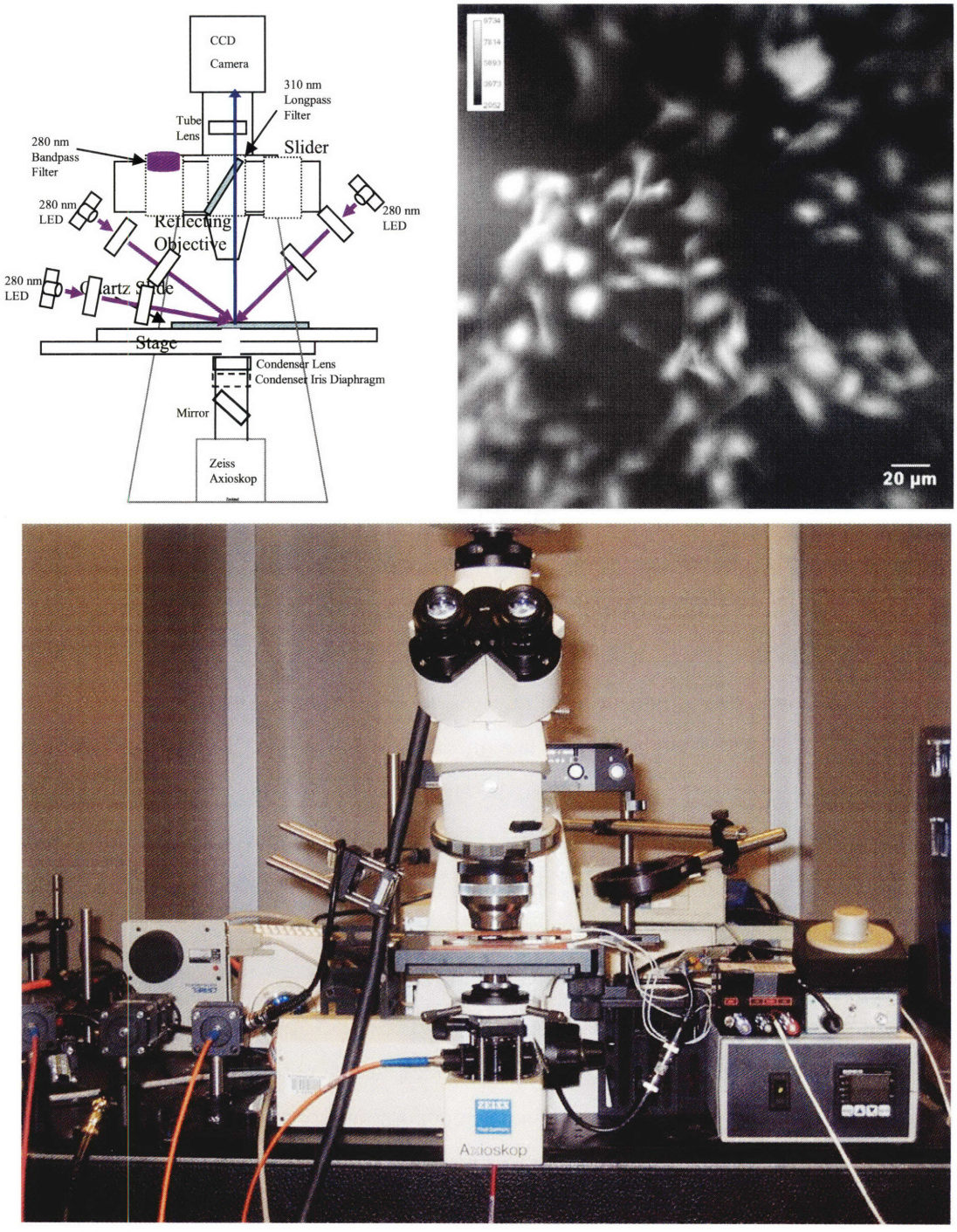


**Fig. 16:** A diagram, image of fixed IC-21 cells, and photo of our scope with oblique flood illumination from above, and the new internal dichroic filter.

or 3 focused onto one spot in order to achieve maximum excitation and signal. For this iteration we also obtained a dichroic filter (Chroma 310dcxxr) sized for the Zeiss filter slider, so we no longer needed the external beamsplitter. This new dichroic improved signal intensity and also significantly reduced noise since the upper portion of the light path was now enclosed and protected from incident light. See **Fig. 16** for a diagram, photo, and an image produced by this version of the scope.

### 3.5 3-D Data Collection.

At this point, we utilized our motorized stage in order to collect z-stacks of native fluorescence images. We then attempted to deconvolve them using a theoretical point-spread function in Huygens (SVI, Netherlands) and displayed the results in Imaris (Bitplane AG, Switzerland) as shown in **Fig. 17**. While the deconvolution helped improved the image somewhat, it was nowhere near the improvement often seen with deconvolution on visible light microscopy. We believe there are two reasons for this. First, our motorized stage is fairly inaccurate – it does not appear to have an encoder or any sort of feedback. Moreover, the calibration is somewhat suspect – we calibrated it based on the distance the stage moves with a full turn of the focus knob as reported in the Zeiss manual, but this calibration is only approximate. Therefore, the z-spacings may be both inaccurate and inconsistent. This can be solved with a newer motorized focus control or a piezo, and an accurate calibration method which we have yet to determine. At the time we could not use an external piezo because we were using a reflecting objective and so the unusually large width of this objective made it geometrically impossible to attach a piezo. However, with the new Ultrafluar objective this should no longer be a problem, so future work should include acquiring z-stacks using a well-calibrated piezo.

A second problem with the deconvolution, as revealed by discussions with Hans van der Voort of SVI, is that the theoretical point spread functions are designed for infinity-corrected scopes, so if we are using a fixed tube length it will not be accurate. This could be solved by measuring an experimental point-spread function, but doing so has proven challenging. We attempted to measure this using Fluoresbrite PolyFluor 345 Microspheres (Polysciences) which are 1 μm polystyrene beads with a fluorescent

compound having an excitation peak around 285 and emission around 345, fairly close to that of proteins. These beads produced a signal too weak to measure effectively when using the reflecting objective. This problem will likely be solved with the Ultrafluar. However, these beads were also too large to produce an effective point spread function. We got a quotation for custom 100nm beads with this fluorophore, but the $2.75k cost seemed excessive. We believe that a more cost effective solution may be to purchase standard 100nm carboxylated polystyrene beads, which are extremely inexpensive, and then nonspecifically absorb BSA to these. The spectrum of BSA will be accurate for protein. If we cannot bind enough BSA nonspecifically, there are protocols and chemicals available for covalent bonding. We believe that the combination of this approach with an effective piezo will allow us to measure a very accurate point spread function for the microscope's native fluorescence mode.

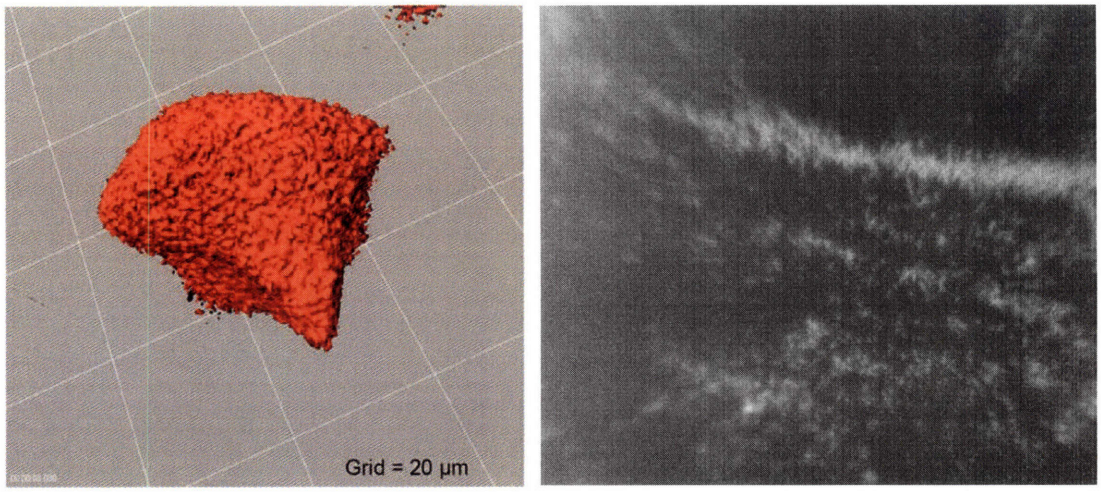


**Fig. 17:** 3D rendering of deconvolved native fluorescence image, and image of PolyFluor 345 microspheres (1µm diameter).

### 3.6 Epifluorescence

While the 3 LED flood illumination provided strong excitation, we still wanted a stronger signal and decided to try a more traditional epifluorescent excitation geometry. At this point we were able to implement epifluorescence in a more elegant way than the original external beamsplitter holder. Instead, we removed the Zeiss filter slider and replaced it with a cage system onto which we mounted a dichroic in a 45 degree mirror holder. This allowed us to inject light sideways into the scope and onto the dichroic, where the UV was reflected down and excited the sample, and the resulting native

fluorescence passed back up through the dichroic and onto the camera. We used a much better beamsplitter than in our original attempt at epifluorescence, a Chroma 310dcxxr which was extremely thin and cut to a 25mm diameter circle. The position of the LED and lenses on the cage system could be adjusted to either focus a bright image of the LED emitter element into the field of view, or have more diffuse and uniform illumination. A diagram of this arrangement is shown in **Fig. 18**, as well as images of the LED adjusted to focus an intense image of the emitter element onto the sample, and of the LED adjusted for uniform field illumination and overlaid with a visible transmission image.

The problem with this arrangement was that it limited the scope to only being used for native fluorescence. In order to take deep UV transmission images, the beamsplitter

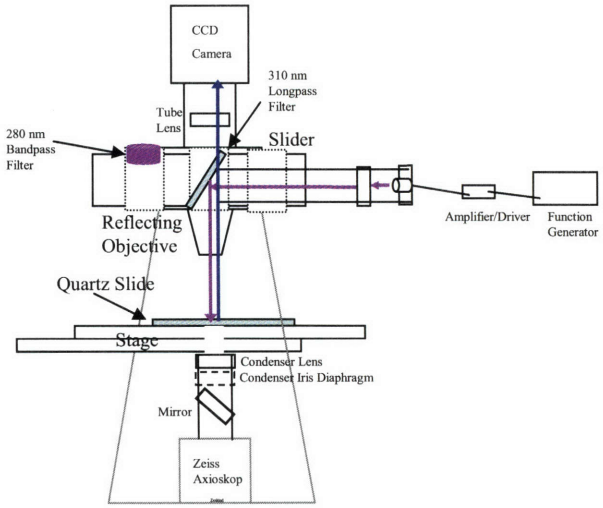


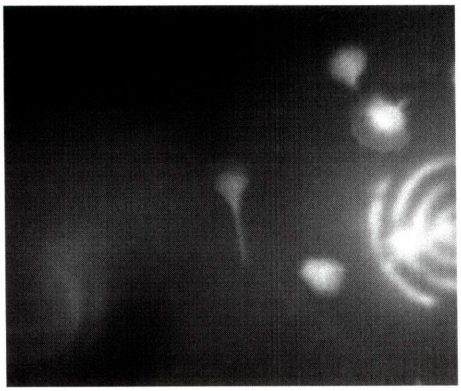

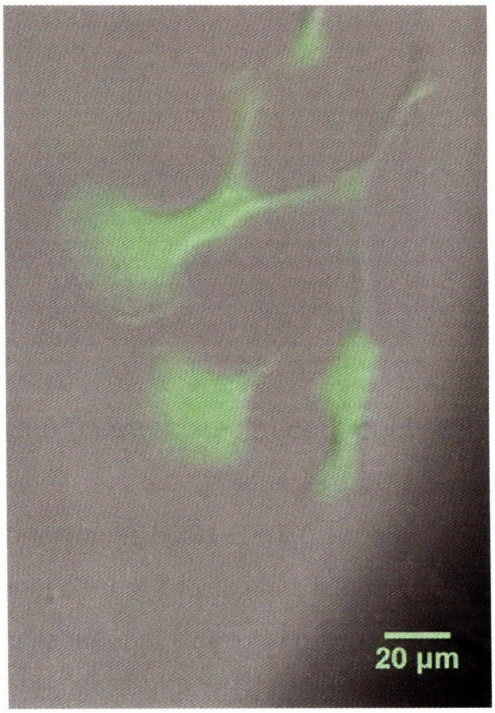


**Fig. 18:** Epifluorescent scope design for native fluorescence; **(right)** native fluorescence data with LED adjusted for uniform illumination (green) overlaid on visible transmission image (gray); **(bottom)** native fluorescence data with LED adjusted for max intensity: concentric circles are image of LED emitter.

and cage system had to be removed completely, and then putting them back and realigning was a time consuming process that also introduced variability into the data. There was a more fundamental problem as well. At this point, we were beginning to consider quantum yield imaging (discussed further below) but when using epifluorescence it was difficult to quantify the excitation intensity as a function of position.

### 3.7 Diafluorescence

The solution to both of these problems was elegant in its simplicity. We excited the native fluorescence using the same excitation path that we utilized for transmission images. This way, a transmitted light image of a blank field accurately quantified the excitation intensity for the native fluorescence (when corrected for filter efficiency as discussed later). The main challenge of diafluorescence is that it requires very effective filtering in order to block all the excitation light from reaching the camera. The dichroic alone was not sufficient to block all this excitation, but after exploring various options we found that a 320nm longpass filter (Melles Griot UG320) was extremely effective at blocking all the excitation and still allowing a strong signal from the native fluorescence. It was so effective that we stopped using the dichroic in order to reduce distortion from an additional unnecessary surface. A diagram of the resulting arrangement, and data from it, are shown in **Fig. 19**. We also tried a 305nm longpass filter, and this allowed more signal intensity but also much more of the excitation light, so it was worse overall. We used a longpass filter as opposed to a bandpass in order to collect all the native fluorescence so we could accurately calculate quantum yield. At one point we were concerned that wide range of wavelengths in the resulting signal were resulting in all of the image not being in focus at any given time. However, we conducted tests with 350nm and 360nm bandpass filters (Chroma and ThorLabs respectively) and found the focus to be approximately equal (see **Fig. 20**). We therefore stuck with the 320nm bandpass filter. Even with all these optimizations, it still required extremely long exposure times (on the order of 3 minutes) to produce an image with high signal-to-noise. Exposure times of this duration increase the likelihood error due to mechanical vibration.

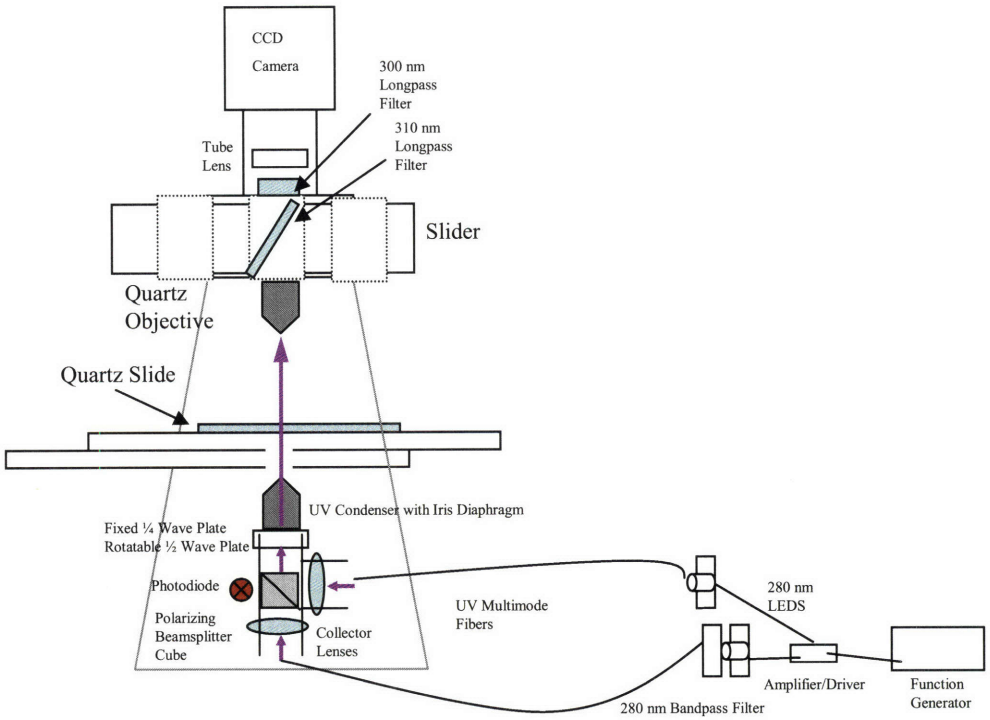


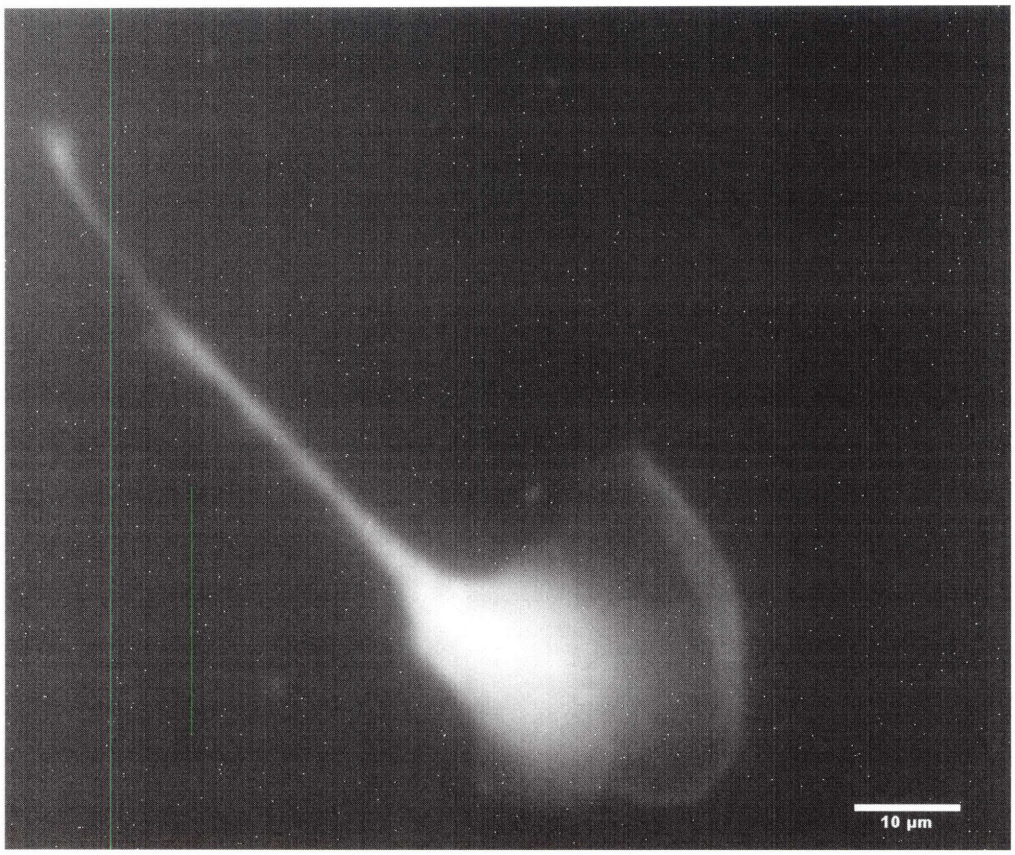


**Fig. 19:** Diafluorescent scope design and image for native fluorescence scope.

### 3.8 Eliminating Stray Light

Because the native fluorescence measurement involves signal at visible wavelengths, it is much more sensitive to stray light than the deep UV measurements. When making these measurements we attempted to cover all indicator lights, LEDs, and other sources of light near the scope. We also would turn off the computer monitor and have the operator sit in pitch blackness waiting for a timer to indicate that the run was finished. However, the installation of the curtain allowed us to isolate the computer (and operator) from the scope. It has, however, proven very difficult to isolate the scope completely from all sources of stray light. One option involves completely enclosing the stage. We have not yet taken the time and expense to completely surround the stage with a dark box. Matt Lang has generously loaned us

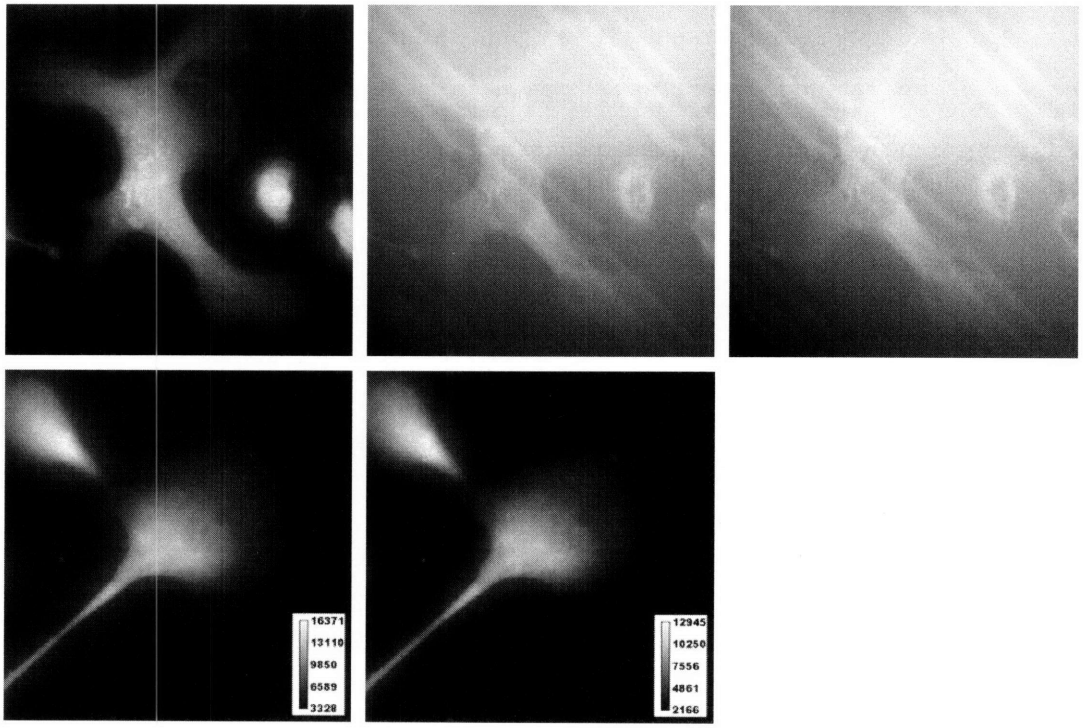


**Fig. 20:** Native fluorescence with various emission filters. (**top left**) 320nm longpass filter, 15 sec exposure; (**top center**) Chroma HQ350/20x bandpass filter, 5 min exposure; (**top right**) ThorLabs 360nm bandpass filter, 5 min exposure; (**bottom left**) 320nm longpass filter, 40 sec exposure; (**bottom right**) 385nm longpass filter, 40 sec exposure.

some low-lint curtain material as a more flexibly way to enclose the scope. We are still developing a sturdy way to install this while insuring that it does not contact the stage heaters at all.

### 3.9 Laser Scanning Confocal Native Fluorescence.

Another positive consequence of the grant we helped write from the US Air Force Office of Scientific Research for "Deep Ultraviolet Laser Imaging for Biology," (PI Dan Ehrlich) was funding to create a laser scanning confocal microscope. Dan has taken the lead on this project, which involves contracting with a company (Microcosm) to modify an old Zeiss laser scanning microscope to excite in the deep UV and detect native fluorescence emission. While there are many technical challenges involved, once these challenges are overcome this will produce an extremely useful instrument which should be able to image native fluorescence in 3-D, at extremely high spatial resolution, and at a high rate with little cell damage. This is an exciting project and the resulting instrument should enable many new experiments.

## Chapter 4: Polarization Modulator Development

Circular dichroism (CD) measurements are important in biology and chemistry, but have heretofore required an expensive instrument occupying over one meter of bench space. The size and cost of these instruments is primarily a function of two key components: the light source and polarization modulator. We have replaced the traditional light source with deep ultraviolet LEDs, which in turn enabled us to replace the traditional polarization modulator with a system that combines two orthogonally-polarized beams square-wave modulated 180 degrees out of phase. Here we report implementing this polarization modulation method using deep-UV LEDs, in order to detect CD in biological samples. This may lead to significant improvements in CD spectrometers and enable the integration of CD detection into a variety of sensors and imaging systems.

CD spectrometers typically generate light using a xenon lamp, which adds to the size, expense, and power consumption of the instrument and requires nitrogen purging. Lamp sources have been the only way to produce deep ultraviolet (UV) light, necessary because most biological molecules exhibit CD only at wavelengths between 200 – 300 nm. But recently, deep UV light-emitting diodes (LEDs) have come on the market, providing a small and inexpensive source of monochromatic deep UV.

Instead of the photoelastic modulator (PEM) used in typical CD spectrometers, we have combine two orthogonally polarized beams square-wave modulated 180 degrees out of phase, to produce a single beam of light that oscillates between two orthogonal polarizations. This concept was suggested by Mackey et al. [48] for the measurement of birefringence. We have improved upon the Mackey concept by using square wave modulation instead of sinusoidal modulation to provide a stronger CD signal, by using deep UV LEDs instead of semiconductor lasers, and by adding a quarter-wave plate with its fast axis aligned 45 degrees from either of the orthogonal polarizations to produce light that oscillates between left and right circular polarization at a user-selectable frequency. The result is an extremely compact and inexpensive instrument capable of detecting CD at deep-UV wavelengths. See **Fig. 21**.

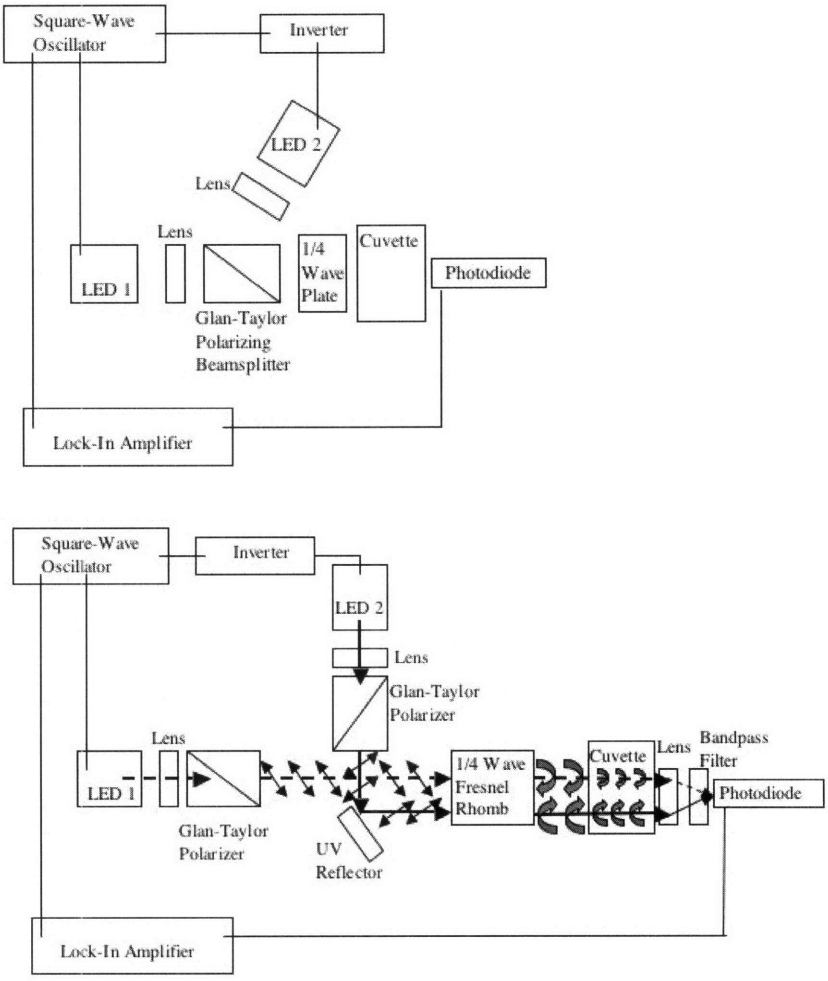


**Fig. 21:** Block diagrams of our polarization modulator setup, (**top**) with initial beam combination method, and (**bottom**) with mirror-edge beam combination method.

### 4.1 LED Driver Circuit

The LEDs were driven by a custom amplifier box built to our specifications by Roger Lam. This has two driver outputs, one of which is inverted so that one of the LEDs is driven 180 degrees out of phase with the other. This circuit also has a TTL output that is used to synchronize the lock-in amplifier (Stanford Research Systems SR530) in order to measure the resulting signal. The output from the UV sensitive photodiode is amplified by a custom amplifier before being sent to the lock-in. The lock-in communicates with a computer via an RS232 connection where a QBASIC program is used to store the output data in a text file.

### 4.2 Beam Combination Methods

Implementing this polariation modulator setup requires combining the two beams. Initially, we attempte to do this using a Glan-Taylor polarizer (ThorLabs), but this required injection of one of the beams at a 68 degree angle, which proved difficult to align and implement. Our signal was improved by an order of magnitude when we implemented Matt Lang's excellent suggestion and replaced the Glan-Taylor polarizer with a sharp-edged mirror, so that one of the beams passed just by the edge, and the other beam reflected off it (see **Fig. 21**). This allowed us to have a 90 degree intersection which enabled much more consistent and rigid construction. Finally, for the microscope condenser assembly, we used a 90 degree polarizing beamsplitter cube from Newport.

### 4.3 Alternate detection methods

One challenge is that our beams were fairly large and somewhat divergent, so the signal that we measured was dependent on the exact position of the photodiode. To verify this, we temporarily replaced the photodiode with our Hamamatsu camera, and imaged the pattern of the two beams. See **Fig. 22**. Clearly, the beams made a fairly large spot. We installed a lens prior to the photodiode to focus the light more closely onto it, and this signficantly increased the magnitude of the signal but did not fully solve the problem.

Another issue is that our system had no way to account for fluctuations in the LED output power over time. We planned to install beamsplitters in front of the LEDs to pick off a small portion of the output prior to polarization, but this was never implemented because it was not clear how to detect these since an analog-to-digital card was probably not sensitive enough, and the lock-in only had a featue for subtracting two inputs, not for ratioing them.

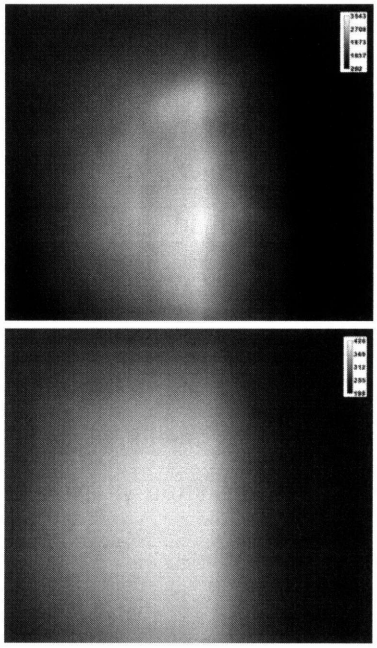

**Fig. 22:** Images of beams from polarization modulator for a cuvette of (**top**) water and (**bottom**) ~4mg/ml tryptophan.

### 4.4 Polarization Tuning

To verify our polarization modulation technique, we temporarily replaced the cuvette and quarter-wave plate with a second polarizer (analyzer) placed between the system output and the UV-sensitive photodiode. The two LEDs were driven at different modulation frequencies, and the photodiode output at each frequency was measured using a lock-in amplifier as a function of angle as the analyzer was rotated through 360 degrees in 20 degree increments. The results, shown in **Fig. 23**, demonstrate that there were in fact orthogonally polarized beams simultaneously incident on the photodiode.

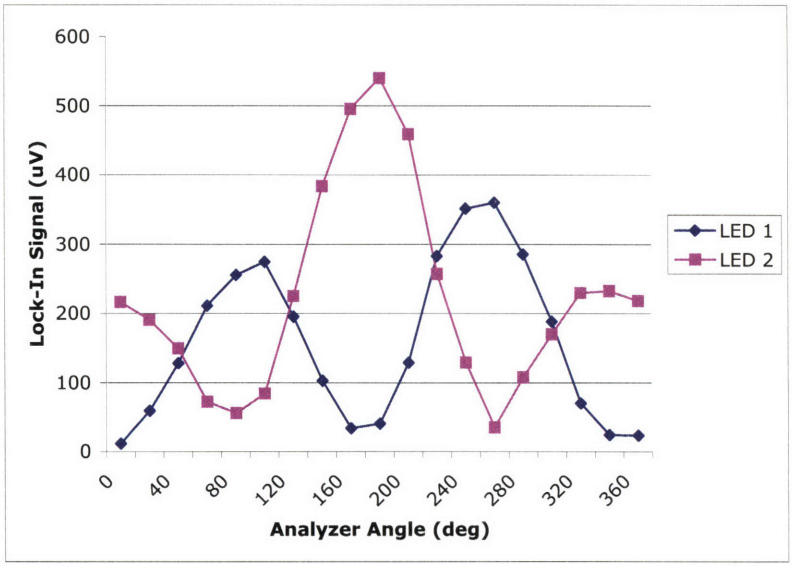


**Fig. 23**: Verification that the polarization modulator beams are orthogonally polarized. Varying peak heights may be due to a slight optical misalignment.

Using our system we have attempted to gather CD information on separate solutions of the four nucleosides adenosine, cytidine, guanosine, and uridine, each at a concentration of 0.05 mg/ml, as well as deionized water (a control assumed to have zero CD), and (1R)-(-)-10-camphorsulfonic acid (Sigma 282146), a control which has strong and well characterized CD. In addition to measuring the difference signal when both diodes were on, we also manually blocked each diode in order to measure total absorption of each circular polarization so as to calculate an average DC signal. The results are shown in **Table 2**.

| | Ben | Ben | Ben | Shimadzu | Ben | Jasco | Ben |
|---|---|---|---|---|---|---|---|
| | OD1 | OD2 | AVGOD | OD | CD (mdeg) | CD (mdeg) | A-B/A+B |
| Uridine | 0.71272928 | 0.67150461 | 0.69211694 | 0.76 | 1358.76527 | 3.59 | 0.02978158 |
| Adenosine | 0.42098765 | 0.40073569 | 0.41086167 | 0.414 | 667.504635 | -0.0788 | 0.02464572 |
| CSA* | 0.10152088 | 0.11028324 | 0.10590206 | 0.084 | -288.807523 | -189 | -0.04137013 |

**Table 2:** Representative values from polarization modulator. Progress is still needed as noise appears to dominate signal.

To calculate OD we take the log of the no-cuvette transmitted intensity over the sample transmitted intensity. The difference in ODs for the two diodes is then the circular dichroism, which can be converted to units of mdeg by multiplying by 32980 as directed in the JASCO Manual [59]; this number converts from radians to millidegrees and also uses a factor of *4 log e* to convert extinction to ellipticity [60].

We also measured circular dichroism values for nucleoside solutions on our JASCO J-715 spectrophotometer for nucleosides at the same concentration. See **Fig. 24**. However, many quantitative questions remain. For instance, adenosine has a slight negative value in our Jasco experiments but a positive value in our compact device. The diodes may emit a variety of other wavelengths – although they are centered at 280 nm, but averaging a variety of Jasco values still does not help significantly. Other possible explanations include the lack of sodium phosphate buffer in our solutions, error introduced by the quarter-wave plate being slightly off-angle, and problems with our data processing approach.

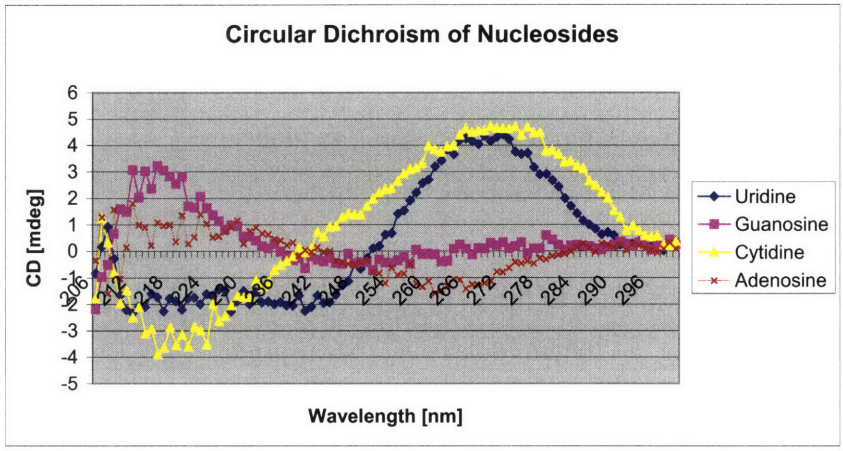


**Fig. 24**: Circular dichroism values for nucleoside solutions measured on our JASCO J-715 spectrophotometer. While the calibration of this instrument has been questionable, these spectra seem to qualitatively match those in [61].

Future work could further investigate these differences in several ways including designing a more effective way to measure the average DC value of the signal, and using a standard such as camphorsulfonic acid to calibrate the system to exact quantitative values of circular dirchoism via a procedure such as that of [62]. We anticipate that these steps will enable a quantitatively accurate CD measurement. Future work could also

apply this measurement to samples in microfabricated channels, and to photoacoustic detection.

In summary, we have demonstrated an extremely compact device for detecting CD in biological samples using deep-UV light-emitting diodes and a polarization-modulation technique combining two orthogonally polarized beams square-wave modulated 180 degrees out of phase.

### 4.5 Polarization Imaging Preliminary Work

Our initial plan was to use the polarization modulation apparatus described previously, and simply use a mirror to direct its output into the condenser. The initial modulator was on a huge breadboard adjacent to the scope (see **Fig. 25**), and we planned to couple its output into the scope using a series of mirrors or beamsplitters, but this proved optically challenging because there was significant loss along the longer path and slight differences in the alignment of the two beams. Instead, we implemented the polarization combiner in the condenser as show in **Fig. 26**, using a 266nm polarizing beamsplitter cube (Newport 05SC16PC.22) in reverse as a polarizing beam combiner, held in a beamsplitter cube holder (Newport CH-0.5) with fused silica collector lenses (Esco Products) mounted in lens holders connected to the beamsplitter cube holder (Newport CH-PORT and MLH-0.5). Conveniently, the threads on these holders also matched the threads from ThorLabs SM05 lens tubes, so we were able to add lens tubes and SMA fiber connectors directly. Above the beamsplitter holder we mounted a rotatable ThorLabs 266nm zero-order half-wave plate and a fixed ThorLabs 266nm zero-order quarter-waveplate. To verify the effectiveness of this arrangement, we utilized the long working distance of the Ealing 36X objective by placing a dichroic sheet polarizer (Oriel 27341) rated down to 270nm

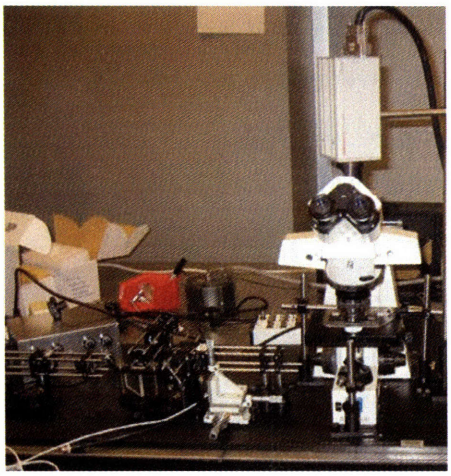

**Fig. 25**: Photograph of polarization modulator adjacent to microscope.

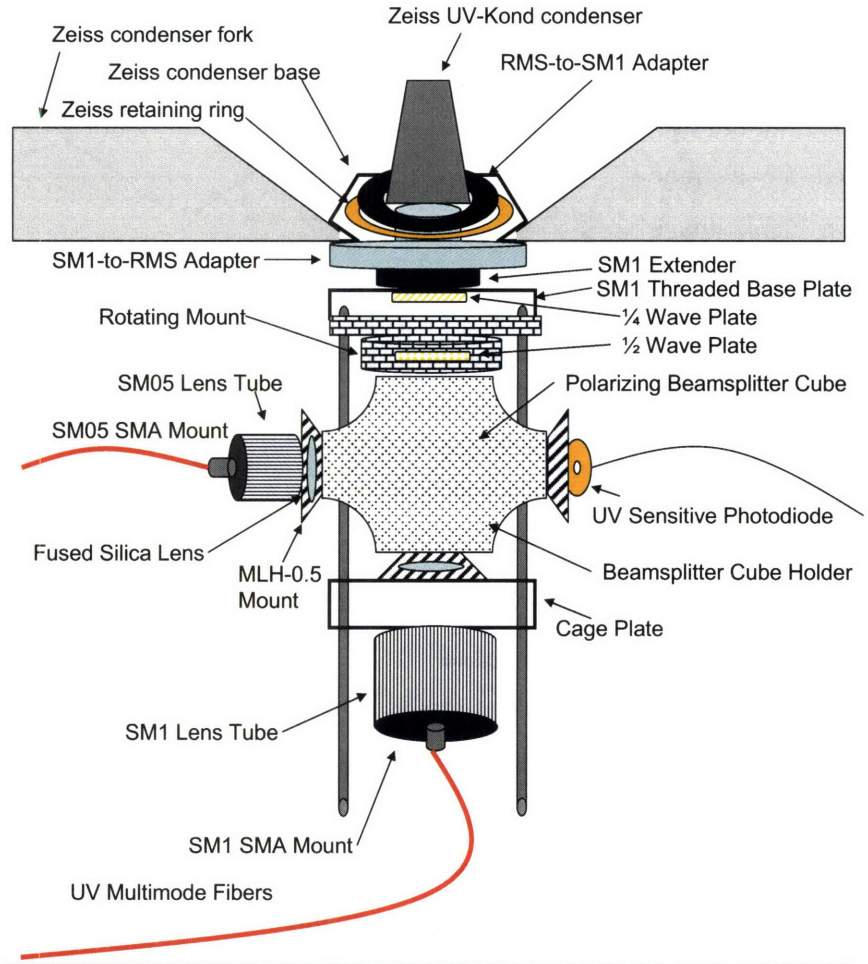


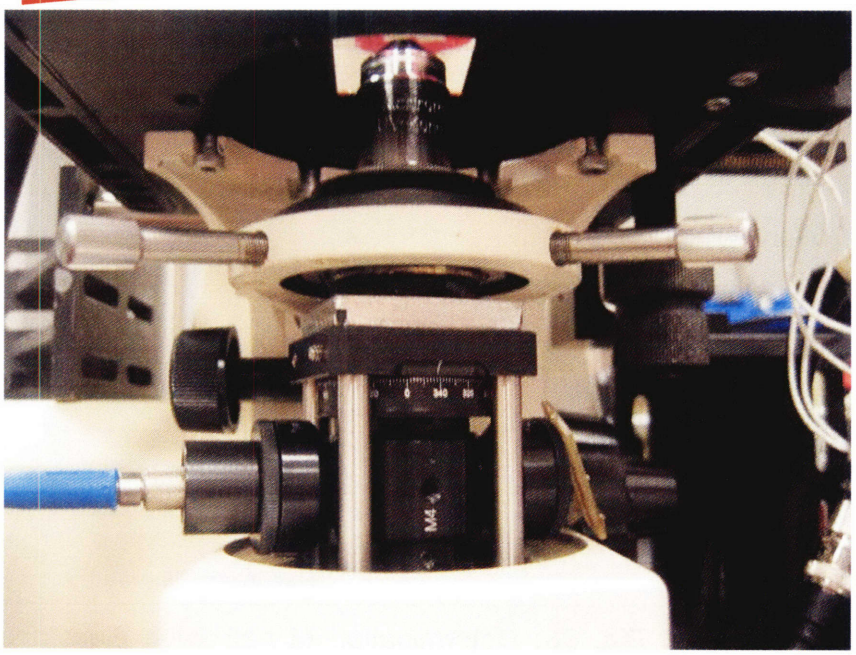

**Fig. 26:** Diagram and photograph of our polarizing combiner condenser.

between the sample and the objective. We then injected light into the bottom port and measured the average intensity of a blank image as a function of the half wave plate angle. Next we injected light into the side port and again measured average intensity of a blank image as a function of half-wave plate angle. The results are shown in **Fig. 27**, and confirm that the condenser indeed produces orthogonally polarized beams. Next, we sought to determine the correct position of the half-wave plate in order to produce left and right circular polarization. To do this, we took advantage of the fact that when light is circularly polarized, a linear analyzer should yield the same intensity regardless of rotation angle. Again using the film polarizer mounted between the sample and the objective, we collected an array of images varying both the half-wave plate angle and the analyzer angle, and identified the two half-wave plate locations that most nearly produced the same intensity regardless of analyzer angle. See **Fig. 28**.

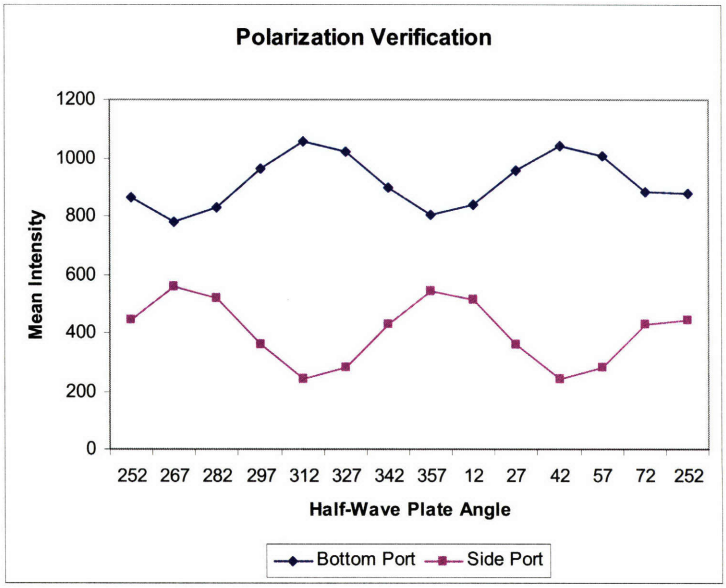


**Fig. 27:** Verification of dual-port orthogonal polarizations.

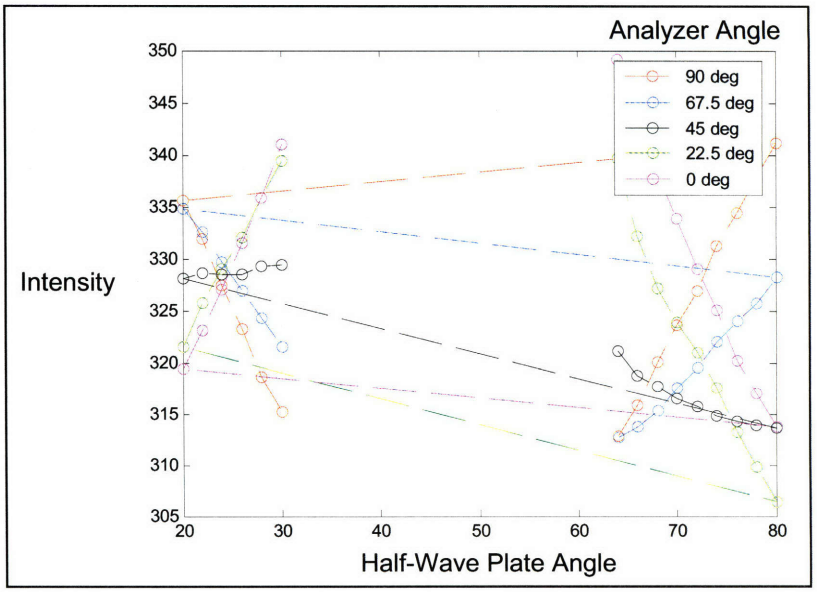


**Fig. 28:** Determination of half-wave plate angles for circular polarization.

A similar calibration was not possible with the Ultrafluar objective due to its short working distance. Instead, we obtained 3M HNP'B film from American Polarizer which is rated as a linear polarizer at wavelengths as short as 280nm. We cut six 25mm diameter circles from this film, and used a set of two Zeiss filter cube sliders to create a set of six different analyzer orientations in the emission pathway. The results are shown in **Fig. 29**, where the six lines represent six different orientations of polarizer film in the beamsplitter slider. These six traces intersect at approximately the same two half-wave plate angles as the previous calibrations, although this data is much noisier due in large part to imperfections in the polarizing film and mount.

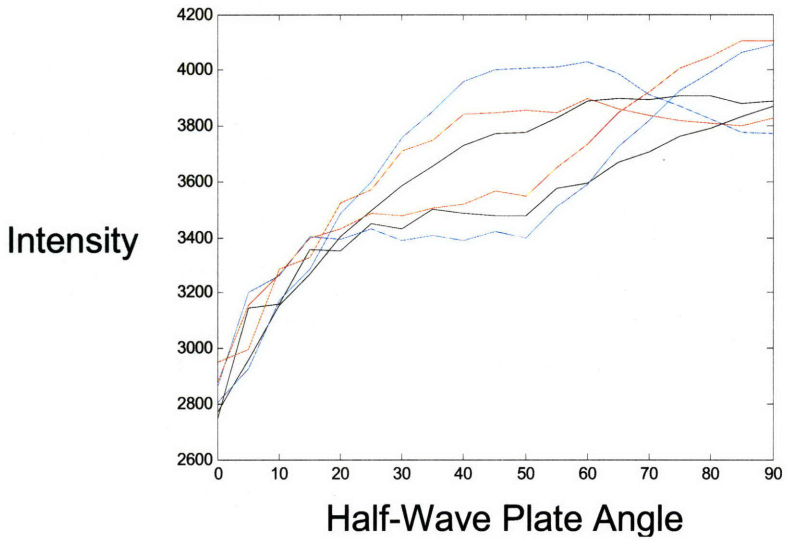


**Fig. 29:** Determination of half-wave plate angles for circular polarization with Ultrafluar objective.

### 4.6 Transmission Circular Dichroism Images

Our initial attempts to gather circular dichroism images occurred prior to the calibration for ideal half-wave plate rotation angle described in the previous section. Instead, we imaged CSA in a quartz microchannel, and water in a parallel quartz microchannel. For a variety of half-wave plate angles, we took images using both the bottom and side ports in an attempt to acquire roughly circular polarizations of opposite handedness. However, these images seemed dominated by lensing at the edges, and even though there were some differences in signal between the water and CSA, it was extremely difficult to calibrate or draw any conclusions based on these images.

See **Fig. 30**. We next tried sealing a small amount of CSA between a quartz slide and coverslip, but this also proved inconclusive, perhaps as a result of strain in the slide and coverslip.

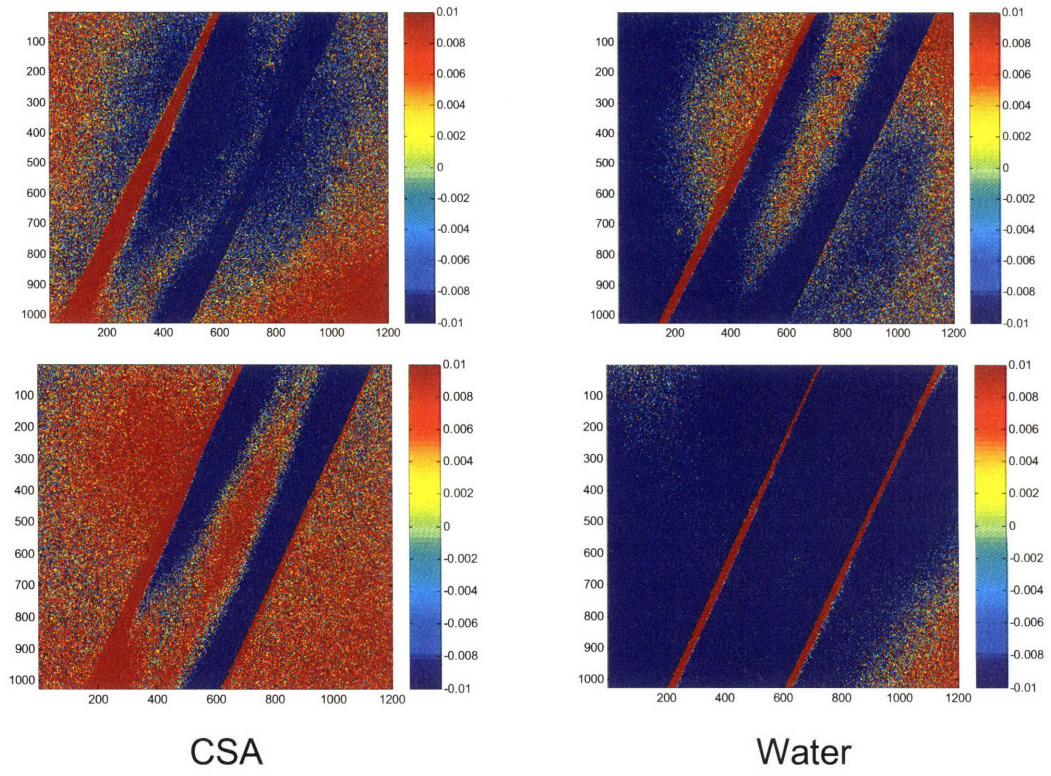


**Fig. 30:** Attempted CD images of CSA (**left**) and water (**right**) in quartz microchannels, units in mdeg, showing significant noise and inconsistency.

After having identified the ideal half-wave plate angles for opposite circular polarizations as described in the previous section, we acquired images of cells with the half-wave plate at each position, determined the OD of each image, and used this to calculate the CD in mdeg. See **Fig. 31**. We then acquired images of the same cells by keeping the half-wave plate in one fixed position, and directing the input through either the bottom port or the side port in order to get opposite handed circular polarizations. The results are shown in **Fig. 32**. The results from these two methods should match, but they do not. This fact, and the fact that we have been unable to effectively calibrate with CSA, mean that there are still significant challenges to achieving effective CD imaging. At Peter So's excellent suggestion we took two same-handedness images in a row and calculated the apparent

circular dichroism caused by noise. There was a significant amount. We have not yet developed an effective way to inject camphorsulfonic acid into the scope in order to calibrate this.

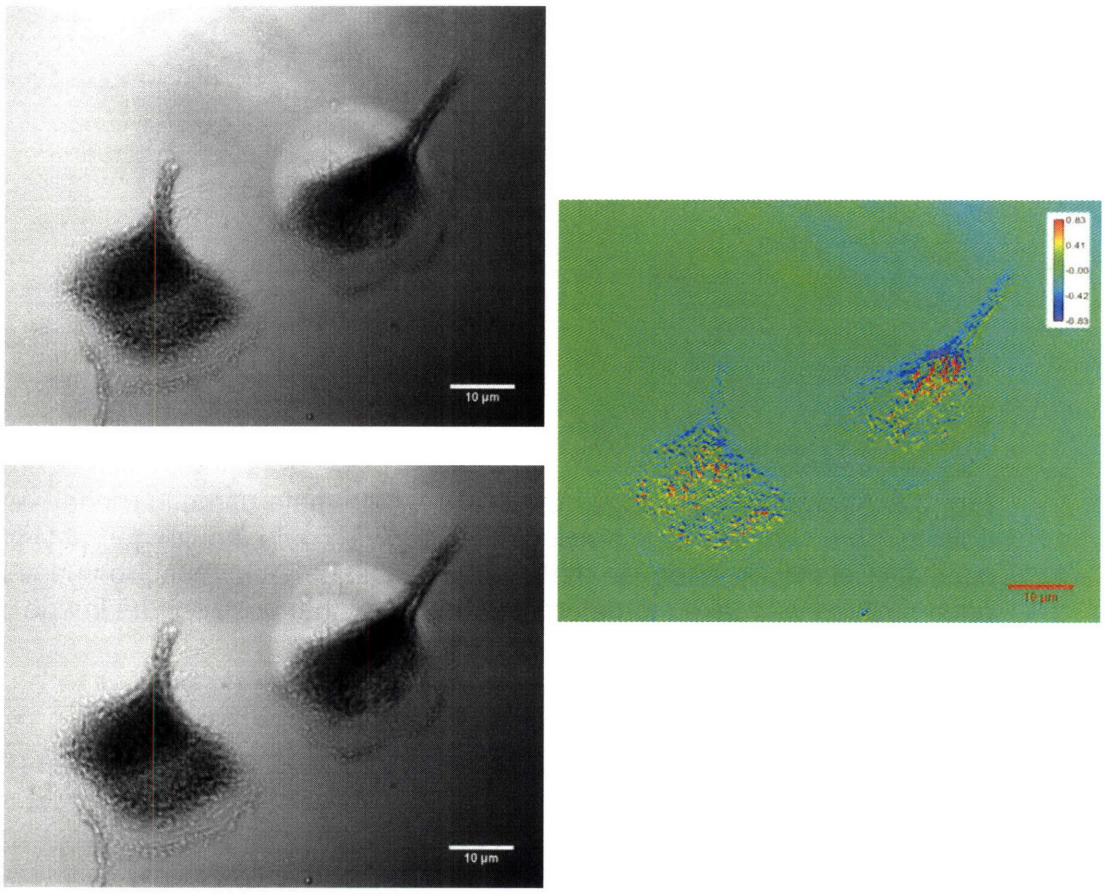


**Fig. 31:** Attempted CD images of IC-21s by manual rotation of quarter-wave plate. Left images are taken with the half-wave plate at each of the two angles determined to have circular polarization as shown in Fig. 29. Right image is the log of the ratio of these two images at each pixel, which equals the difference of the ODs, assuming constant field illumination.

### 4.7 Fluorescence-Detected Circular Dichroism Images

Using the exact same method of switching input polarization, and simply having a different emission filter, we measure the fluorescence-detected circular dichroism in **Fig. 33**.

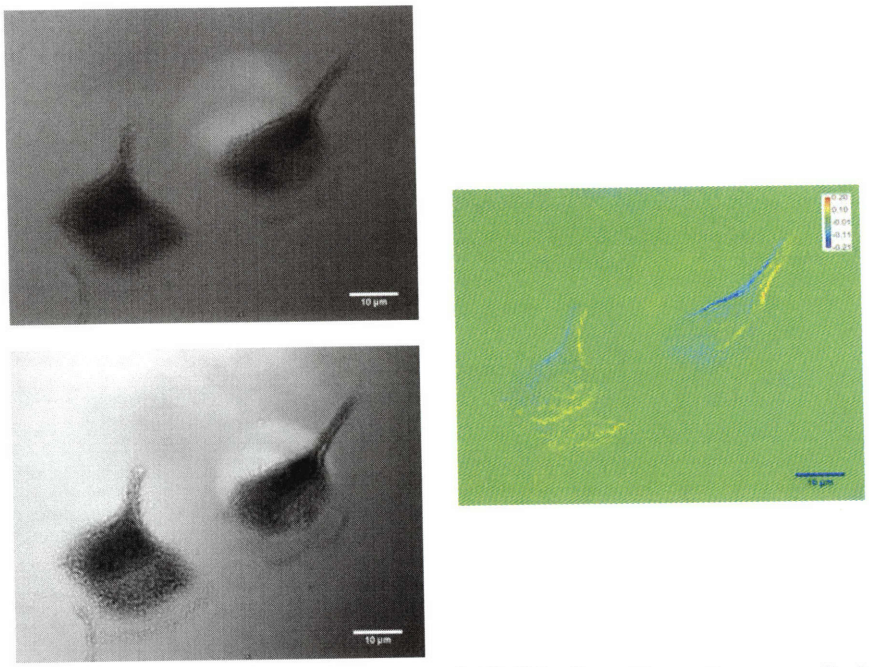

**Fig. 32:** Attempted CD images of IC-21s by alternate use of side port and bottom port. Unlike the previous figure, we could no longer assume constant field illumination, so the log of the ratio of background to image at each position was taken to determine the OD at that position; the image on the right is the difference of these two ODs.

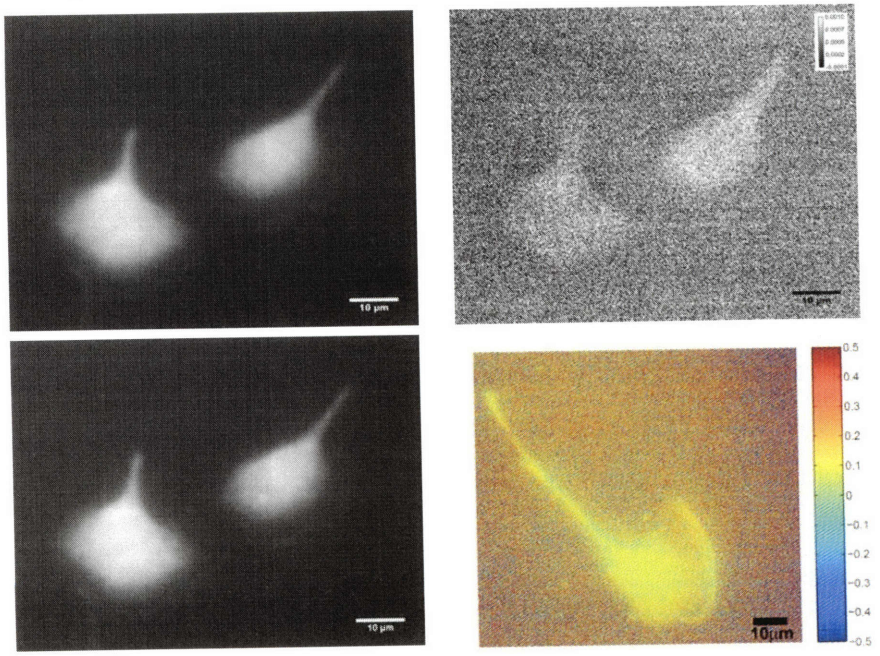


**Fig. 33:** Attempted FDCD images of IC-21s. (**top left and bottom left**) taken with the half-wave plate at each of the two angles determined to have circular polarization as shown in Fig. 29. (**top right**) Calculated CD from these two images by equations in the text. (**bottom right**) Another calculated FDCD image.

Obviously this is extremely high in noise and it is not clear if the signal exceeds the noise. It is necessary to develop ways to strengthen this signal. The image was calculated by dividing the difference of the two images by the sum of the two images, then multiplying by 2 using an equation from [63].

There is additional error because this measurement requires a manual rotation, and this also prevents it from being automated for time lapse images. We looked into acquiring a motorized rotator, but these are quite expensive. Another option may be to mount two differently oriented waveplates in a motorized filter wheel. But it would be ideal to use the modulator system, which would also improve the signal-to-noise ratio through synchronous detection.

### 4.8 Circular Dichroism at Shorter Wavelengths

One issue with the transmission circular dichroism measurement is that the magnitude of the circular dichroism at 280nm may be very small. It is also challenging to interpret circular dichroism at these wavelengths because the differences between different proteins and small and indistinct. Perhaps the most common wavelength for looking at circular dichroism is 222nm, where strong signals and clear differences allow the differentiation of alpha helices and beta sheets. Much of the CD in proteins decreases to zero at wavelengths longer than 240nm. Yet shorter than 240nm, there is a significant amount of information and several quantitative methods to extract protein secondary structure from CD measurements [64]. Unfortunately the lowest reported LED wavelength from Sensor Electronic Technology is 247nm [65]. We have just purchased a deuterium lamp (Ocean Optics) which should have constant output down to 200nm, and a 220nm bandpass filter (Melles Griot), and are preparing to test the scope at this wavelength. However, 220nm CD will present a number of challenges. First is the polarization optics. The shortest wavelength polarizing beamsplitter cube Newport offers is for 248nm. Thorlabs does not offer wave plates for these wavelengths either. We will most likely have to obtain polarization optics from smaller and less reliable specialty companies, or else expensive custom parts. Moreover, our fiber optics will have much lower transmission at these wavelengths. The behavior of our condenser and objectives

is also unpredictable. They may have low transmission at these wavelengths (some reports indicate that the Ultrafluars are only specified down to 250nm). Also, they may have strain which could introduce more error at these wavelengths. On a more positive note, our camera should behave well – it is specified to have constant QE down to 200nm. Finally, we may have difficulty finding imaging-quality bandpass filters at these wavelengths. We hope to overcome these challenges in order to implement circular dichroism imaging at 240nm and shorter wavelengths. Having done so, we would also like to take time-lapse circular dichroism images of cells moving and dividing.

### 4.9 Stable Scope Design

Although the circular dichroism proved difficult to validate, all these design iterations led to a relatively stable and robust scope design, pictured in **Fig. 34**, which is in principle capable of imaging in three modes: transmission UV imaging, native fluorescence imaging, and circular dichroism imaging.

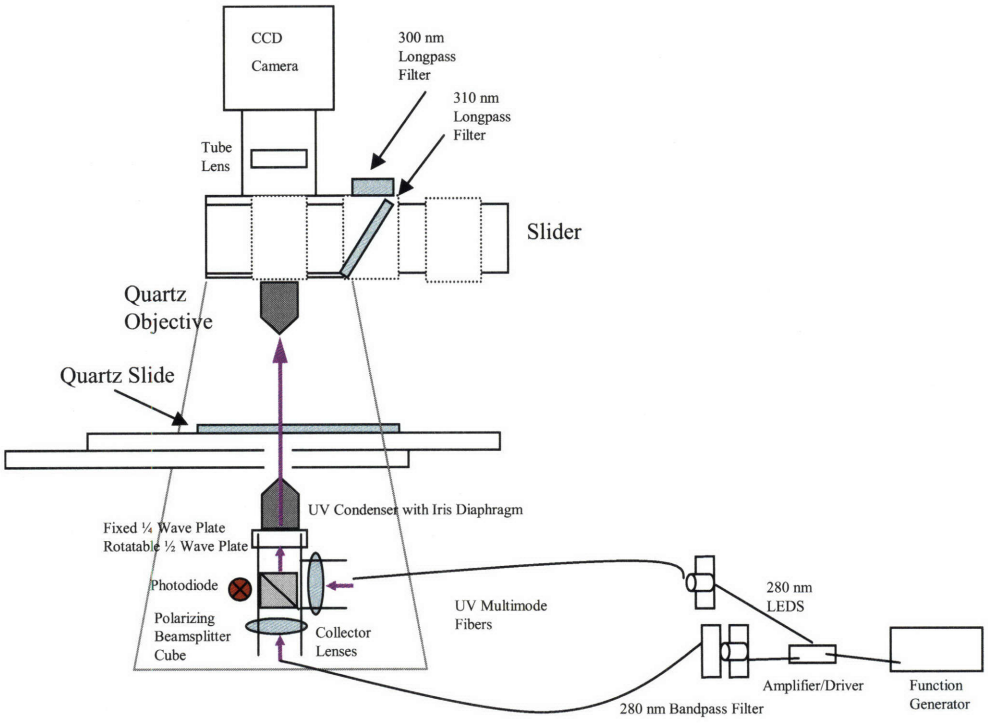


**Fig. 34**: Robust scope design.

## ACQUISITION AND ANALYSIS METHODS

### Chapter 5: Live Cell Imaging Methods

All the development work described in previous chapters was performed using fixed samples, which provided a constant reference sample independent of external conditions. In order to image dynamics in living cells an additional set of modifications was necessary.

### 5.1 Temperature Control

Most cultured cells die quickly unless they are kept at 37°C. A number of temperature control methods exist, all of which have been explored in depth by Winston Timp in our laboratory. One common solution on commercial scopes is a large, clear acrylic box which encloses the entire stage and most of the microscope, except for the eyepieces. The box is then heated and maintained at 5% $CO_2$. The Deltavision scope previously in our lab had such a box. Unfortunately, these boxes are quite expensive (on the order of $10-$16k). Our lab is also in the process of designing and having fabricated custom boxes, but this has proven an extremely time-consuming process taking many months. We therefore determined that an acrylic box was not the optimal solution.

Another interesting solution is offered by Bioptechs, which manufacturers a Petri dish with an imaging-quality bottom and a resistive heating element built into the dish. Unfortunately, the dish bottom is made of standard glass which is not UV-transparent, and we are unaware of any quartz-bottom options.

Another option involves using an objective heater in combination with glass-bottom Mattek dish. The objective heater was not a feasible option for the reflecting objective because of its large size, but could potentially work with the Ultrafluar objective. But this still presents a problem because our scope is upright instead of inverted. The heated objective is supposed to contact the glass surface to which the cells are adhering, but in order to do this we would have to invert the dish, and make sure it is filled completely, such that there is fluid in contact with the cells. This is not practical.

Moreover, Mattek dishes have a glass bottom. We attempted to produce homemade quartz Mattek dishes by removing the glass bottom and replacing it with a quartz coverslip, but this was time-consuming and the results were inconsistent and did not produce an even surface.

Another type of heating involves a hollow metal block through which water is passed at a regulated temperature. However, we were not able to find such a block sized for our stage, and additionally there were concerns that the moving water could introduce serious vibration into our high resolution images.

Finally, we developed a simple but effective solution. We heated the stage block directly by using adhesive heating elements (Omega, Stamford CT) controlled by a thermostat controller (Minco, Minneapolis MN). See **Fig. 35**. A temperature probe for thermal feedback was attached to the slide with tape. This solution kept the slide at a fairly stable 37°C. To insure a stable temperature for the cells and reduce thermal focus drift, we pre-heated the stage for at least an hour prior to putting samples on it. While the stage was being pre-heated, we placed a blank slide on it and lowered the objective into contact with glycerol, so that the objective would also be warmed via the glycerol.

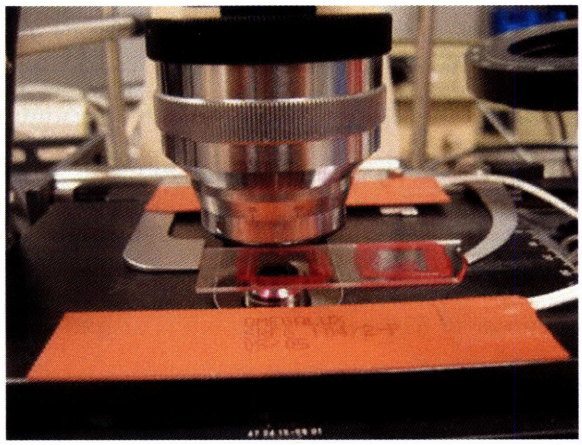

**Fig. 35**: Adhesive heating elements on stage.

To keep the cells in media and at balanced $CO_2$ concentration, we tested a number of different ways to create a sealed chamber. We tried creating a very thin chamber with Invitrogen Secure-Seal spacers but the resulting chamber was too small. Double-sided tape also proved challenging to work with. We considered but rejected the idea of metal holders for creating a two coverslip sandwich. Finally, many broken coverslips later, we settled on a robust solution -- creating a chamber by attaching a Hybaid Easiseal adhesive frame (Thermo-Electron Corp., Waltham MA) to a quartz slide (Chemglass, Vineland NJ or SPI Supplies). We then filled this chamber to capacity (approximately 26 μL) using

media that had just been taken from the incubator and was therefore temperature and $CO_2$ balanced. Live cells were plated onto quartz coverslips which we inverted onto this media-filled chamber. The result was a sealed chamber, with the cells inverted and exposed to media. One issue initially was that the wet coverslip would not adhere well to the chamber frame. To mitigate this problem, we would blot the edge of the coverslip with a kimwipe prior to attaching, and also place an adhesive ring (Invitrogen 13mm diameter Secure-Seal Adhesive Spacer S24735) on top to hold the coverslip securely in place. To reduce thermal shock to the cells, and also thermal variations that could cause focus drift, we kept the slides at 37°C prior to use, and also warmed the glycerol immersion media to 37°C. This entire procedure is diagrammed in **Fig. 36** on the following page.

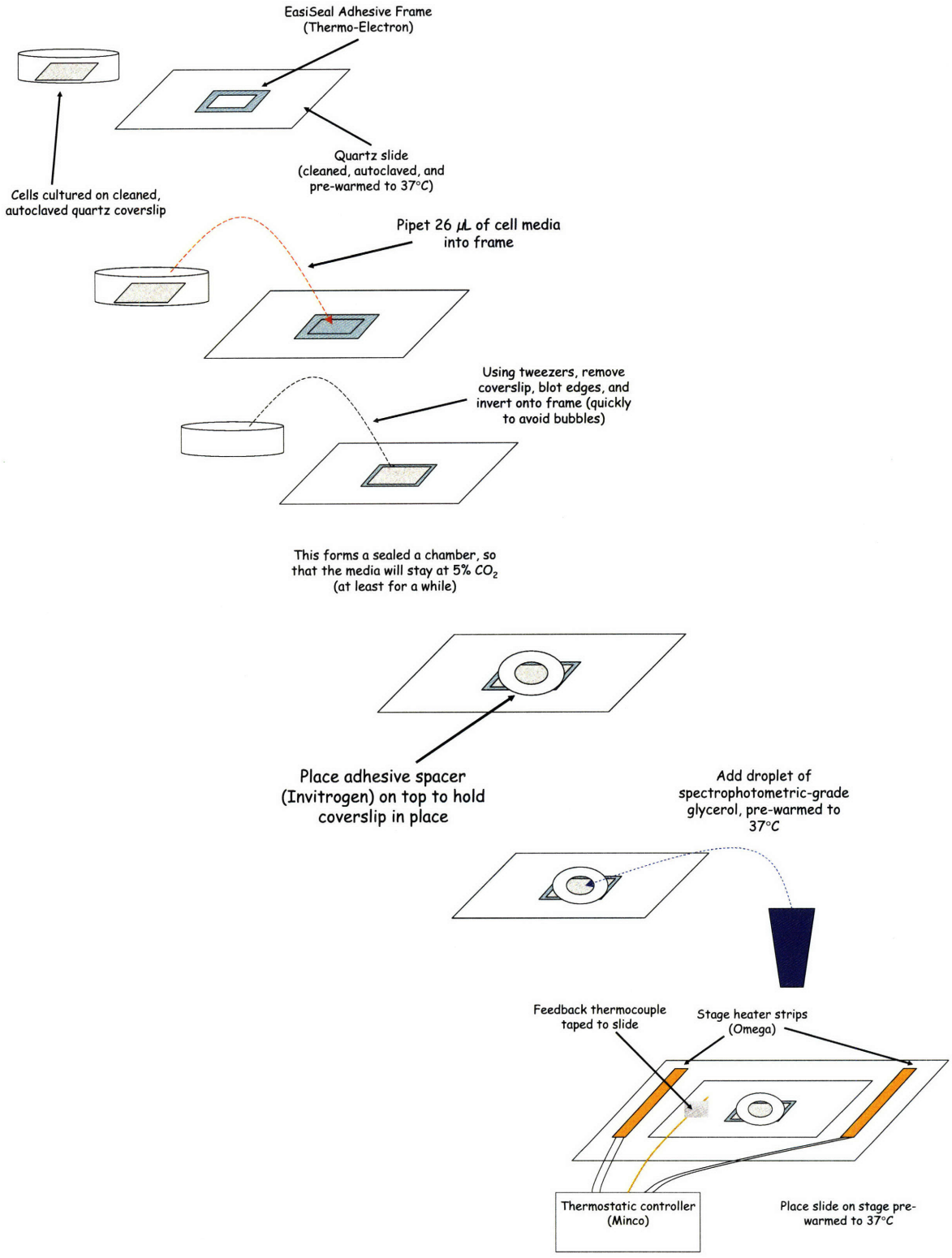


**Fig. 36**: Procedure for preparing live-cell samples.

One challenge with these chambers is that they are difficult to unseal once closed, and so we cannot add reagents in the middle of an imaging experiment. To enable this, we tried using Invitrogen Coverwell perfusion chambers (C18120 and C18139) which utilize a plastic coverslip material. While this material absorbs a significant amount of UV, it does allow enough transmission to produce images; albeit with longer exposure times. However, using these chambers with our upright scope was challenging, because we needed the cells to be on the plastic film, and so we had to adhere the chambers to slides, autoclave the assembly, pipet detached cells into the chamber during a split, and invert the slides so that the cells would settle and grow on the plastic surface. We were able to invert the slides across a Petri dish full of media, which kept the atmosphere moist so the media would not evaporate out the perfusion holes. While this complex arrangement may be necessary for certain experiments, we found it to be not worth the hassle most of the time.

### 5.2 Cell Preparation

Cells were grown in a 37°C incubator with 5% $CO_2$. IC-21 mouse macrophage cells (ATCC, Manassas VA) were cultured in RPMI (Mediatech, Herndon VA) with 15% FBS (Invitrogen, Carlsbad CA) and approximately 1-2% penicillin-streptomycin (Mediatech, Herndon VA). HT-1080 (human epithelial fibrosarcoma) cells (ATCC, Manassas VA) were cultured in DMEM (Mediatech, Herndon VA) with 10% FBS (Invitrogen, Carlsbad CA) and 1% penicillin-streptomycin (Mediatech, Herndon VA). All cell types were cultured on quartz coverslips (Chemglass, Vineland NJ or Electron Microscopy Sciences, Hatfield PA or Structure Probe, West Chester PA).

### 5.3 Coverslips and Slides

For our initial experiments we used coverslips and slides straight out of their sealed packaging, but even this brand new quartz often appeared to be dirty. So we finally adopted a time-consuming but effective procedure. Each new slide and coverslip was opened, the dust blown off with an air can, and rinsed. Each was then wiped with windex on a cotton swab, then rinsed again and dried carefully to avoid streaks using

Ross optical tissue. Finally, the clean dry slides and coverslips were autoclaved for sterility. We considered sterilizing by UV radiation, but were concerned that this may select for UV-resistant bacteria or leave other microorganisms alive.

### 5.4 Timing for Live-Cell Imaging

Long exposures to UV are toxic, as we demonstrated by using exposure times of 10 s separated by 10 s of dark time to image an IC-21 (mouse macrophage) cell for ~361 exposures – just over 2 hours including ~ 1 hour of total UV exposure. As shown in **Fig. 37**, this causes dramatic necrosis. In contrast, we can significantly reduce the toxicity with 100 ms exposures at 1 min intervals. Using these shorter exposure times to reduce damage, and longer intervals to permit damage repair, an IC-21 remains alive and motile after 361 exposures – over 6 hr including 36.1 s of total UV exposure as shown in **Fig. 38**.

A key aspect of this short-exposure imaging is that the LED is synchronized with

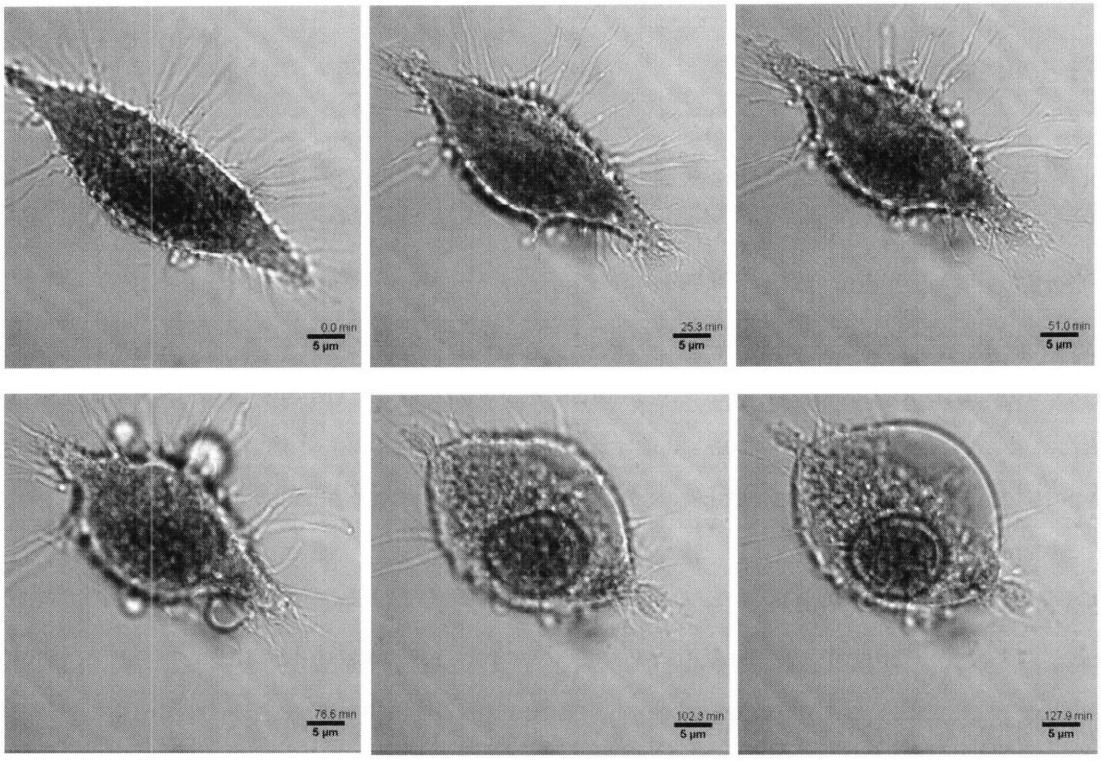


**Fig. 37**: Time-lapse image of IC-21 subjected to 10 second UV exposures with 10 second delay in between, showing dramatic necrosis.

the CCD camera so that the cells are only exposed while the camera is actually recording an image. As described earlier, we designed LED amplifiers that are triggered by TTL input pulses. Our PhotonMAX camera has a shutter-out BNC that sends a positive TTL pulse when the camera is recording. This output is designed to trigger a mechanical shutter, but it works just as well for triggering our LED amplifier. We also believe that having a sufficiently long interval between exposures is important in order to give the cells time to repair photodamage and neutralize any free radicals that may be generated.

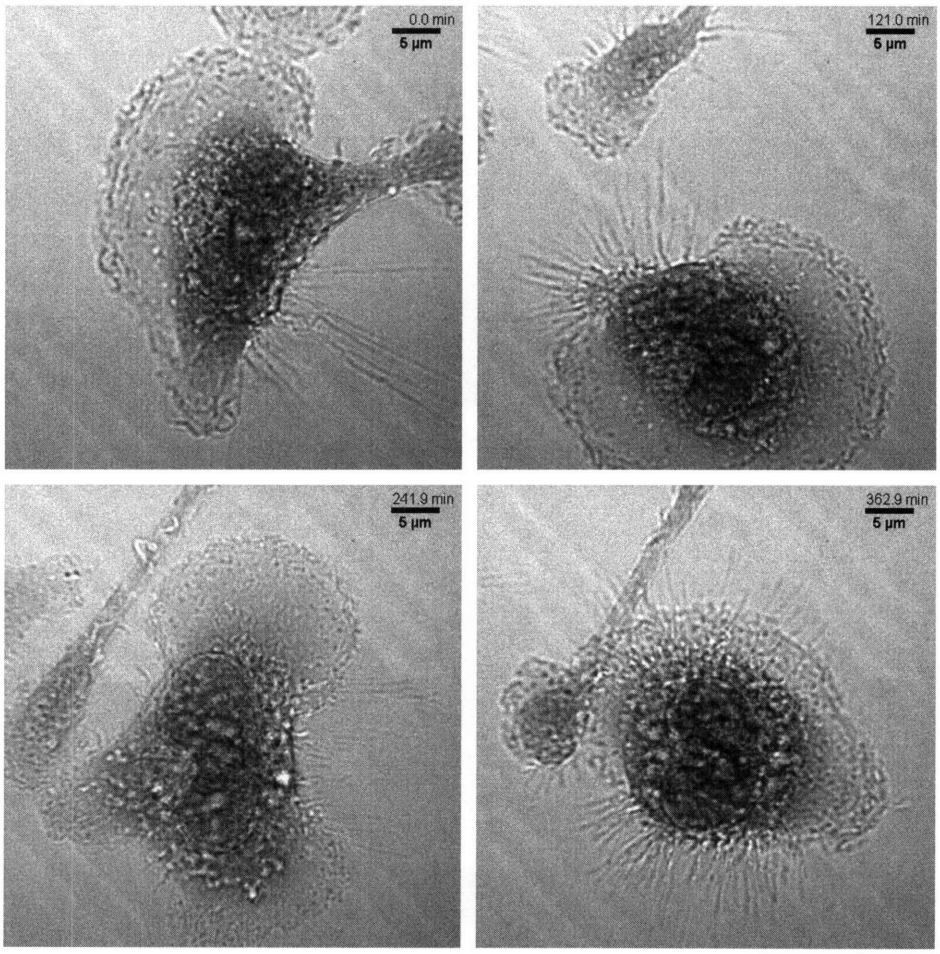


**Fig. 38**: Time-lapse image of IC-21 using 100 msec UV exposures with 60 second delay in between, showing no visible harm after six hours.

## 5.5 280nm Live-Cell Imaging of Motility

Using this timing to reduce damage, we were able to capture 280nm time-lapse images of IC-21 motility as shown in **Fig. 39** [66]. The ruffling region at the leading edge of the cell and the retraction fibers at the trailing edge are clearly visible. We were also able to image motility in an HT-1080 (human epithelial fibrosarcoma) cell as shown in **Fig. 40**.

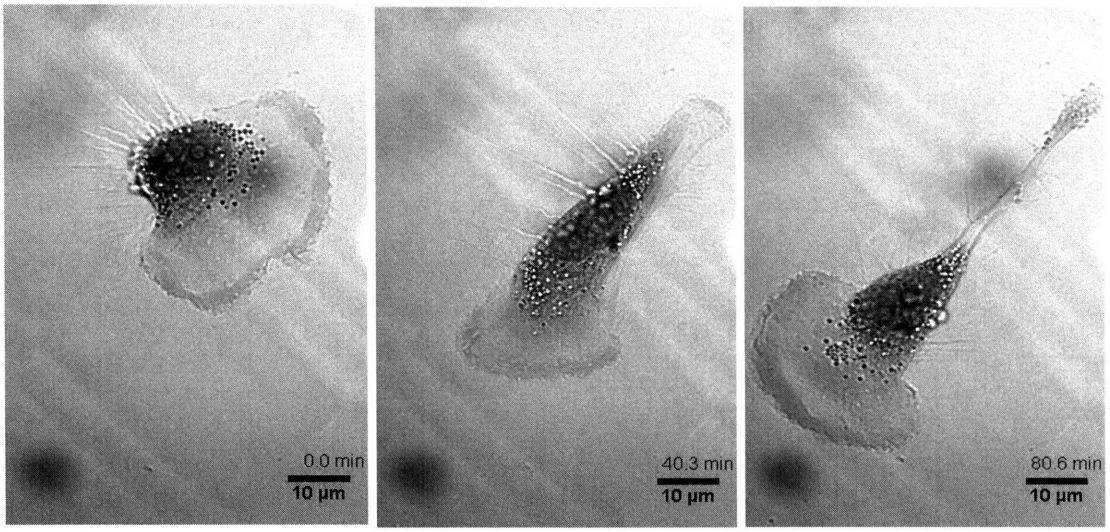


**Fig. 39:** 280nm time-lapse images of IC-21 motility.

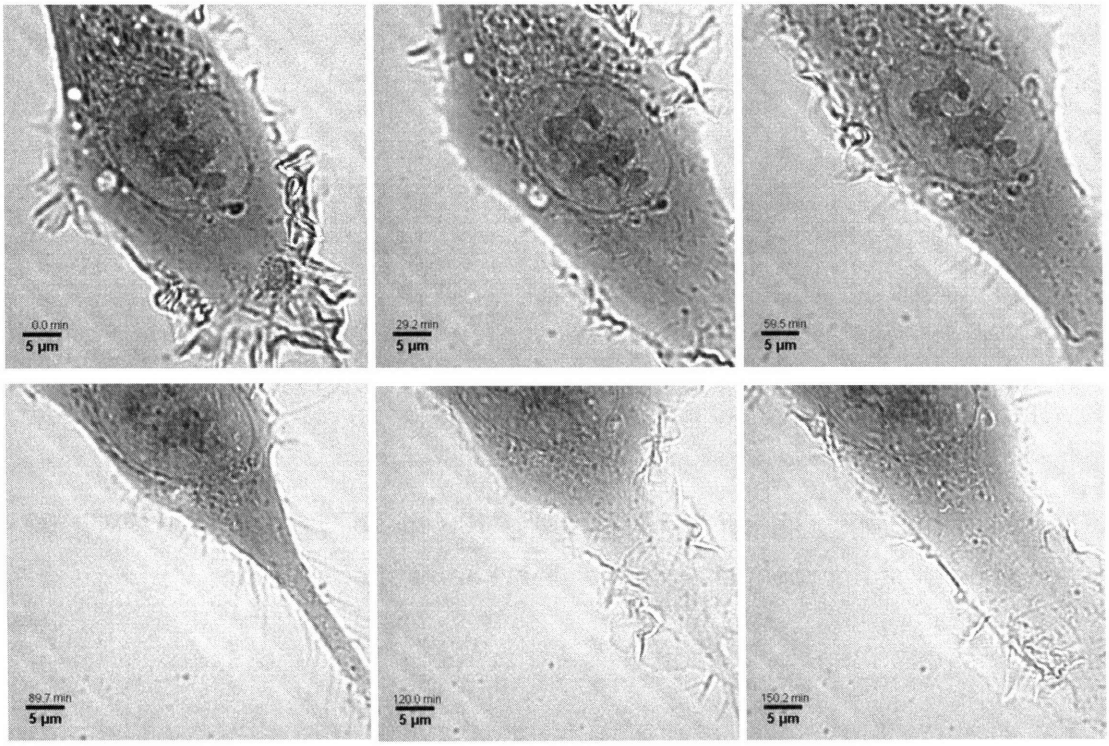


**Fig. 40:** 280nm time-lapse images of HT-1080 motility.

## 5.6 280nm Live-Cell Imaging of Mitosis

We have also succeeded in capturing 280nm time-lapse images of mitosis in HT-1080 cells as shown in **Fig. 41** [66], which captures the chromosomes separating with high contrast and spatial resolution. **Fig. 42** shows another HT-1080 dividing, and **Fig. 43** shows a third, with the colors inverted to make the chromosomes more visible and a small amount of gamma correction applied.

The cells may experience DNA damage and could manifest serious effects during longer-term studies, but for shorter-term processes such as motility and mitosis they exhibit no visible changes in dynamics or structure.

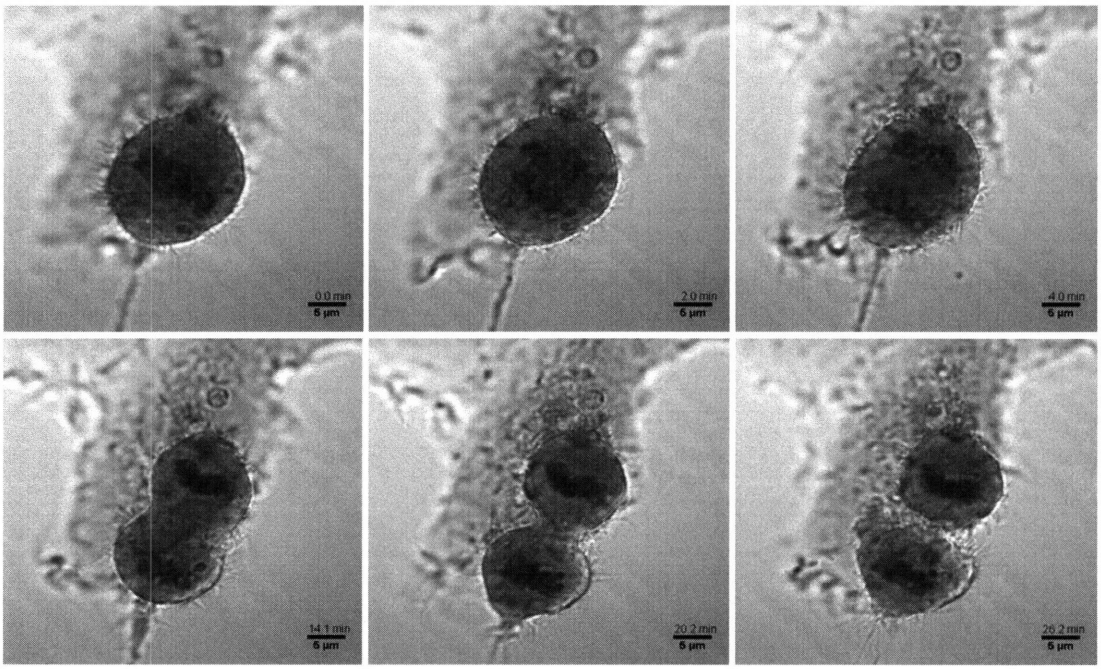


**Fig. 41:** 280nm time-lapse images of HT-1080 mitosis.

## 5.7 Estimation of Power Output

We also are able to prevent necrosis because the camera is so sensitive, and because we are using relatively low power levels. The 280nm LEDs are specified at 1mW, and the 260nm LEDs are specified at 0.1-0.2 mW. However, the fiber coupling is very inefficient and so we believe the actual power is much lower. We attempted to measure the power using a ThorLabs PDA155 photodiode which comes with an

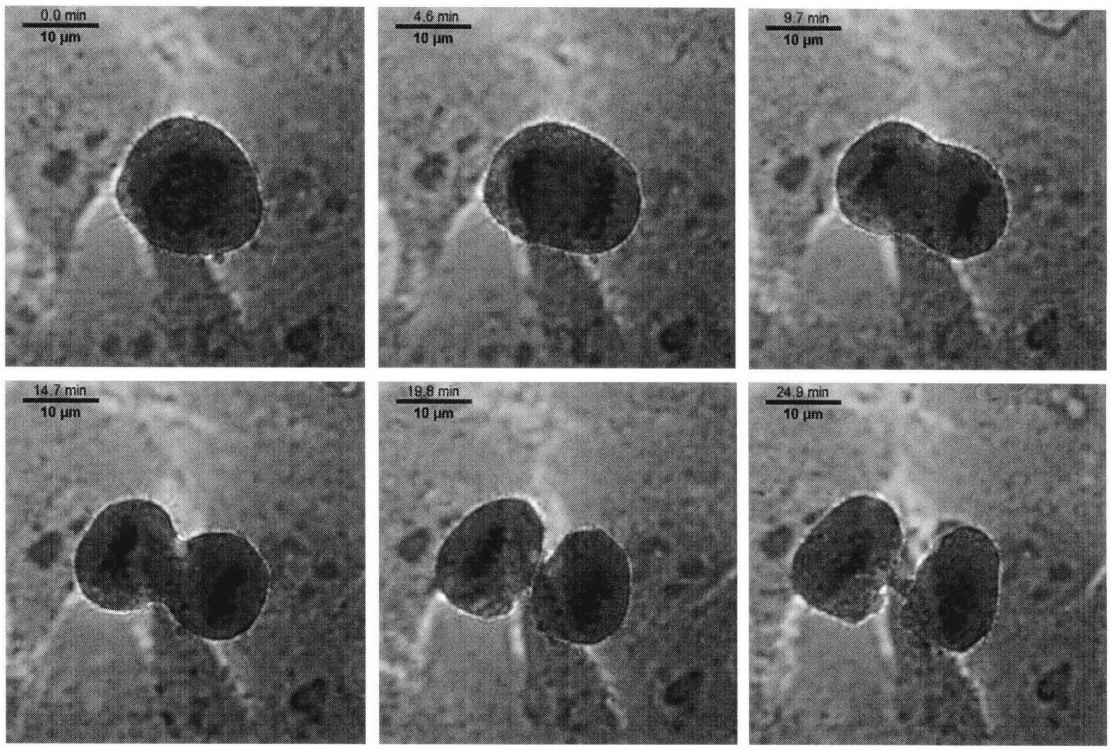


**Fig. 42:** 280nm time-lapse images of another HT-1080 undergoing mitosis.

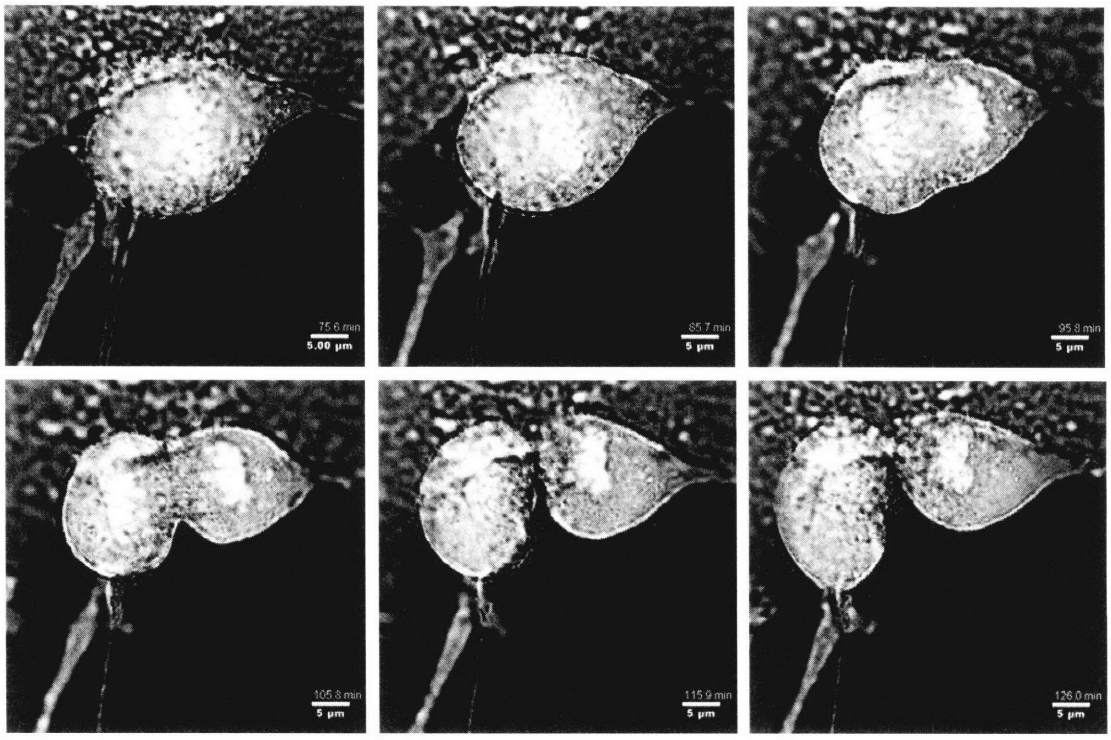


**Fig. 43:** Inverted, gamma-corrected 280nm time-lapse images of a third HT-1080 undergoing mitosis.

approximate calibration curve. By putting an SMA fiber connector onto this photodiode and attaching it to a multimeter, we were able to read a voltage and use the calibration to convert it to an approximate power. Using this method, we measured the 280nm LED power after fiber coupling and passing through a 0.5 meter fiber to be ~0.0036 mW. The photodiode has a 0.8mm$^2$ active area so the power per unit area is 0.0045mW/mm$^2$. However, these numbers are somewhat questionable because the signal is very small – just 1.8mV on top of 13.9mV dark value. The signal decreased even further after end-coupling to another fiber, to ~0.0019 mW. Finally, after another 0.5 meter fiber, collector, condenser, and quartz slide we measured ~0.0004 mW. However, this number is even more questionable because to make the measurement the detector was held by hand on the stage, and signal is just 0.2 mV on top of ~14.1 mV dark value.

In a series of follow-up experiments, we used a 1-junction 260nm LED with close coupling instead of the lens coupling we had been using previously. With this new LED, after 0.5m of fiber we measured 22.3mV which converts to .0176 mW, and an 8-junction 280nm close coupled measured 21.2 mV which converts to .0154 mW.

### 5.8 Live/Dead Kit Experiments

While the rounding up of the cell is a dramatic indication of necrosis, it would be beneficial to have a more sensitive indicator of cell viability. The UV action spectrum and phototoxicity literature has a number of promising tests such as clonal viability [67], but these remain challenging to implement particularly for a single cell or small group of cells that has been illuminated. We also attempted to use a Live/Dead kit (Invitrogen L3224) which assesses membrane permeability as an indicator of cell viability using calcein AM (which glows green in the presence of esterases in living cells) and ethidium homodimer which fluoresces in the red when bound to DNA – which it can only do when the nuclear membrane is permeable which occurs in dead cells. In order to overlay these images, we adapted the scope to excite and image visible light fluorescence. For a light source, we used the mercury lamp from our Axioskop (Zeiss 44-72-16 housing, driven by Opti-Quip Model 1500 power supply), which we mounted on the optical table in front of a filter holder and SMA fiber connector. As an excitation filter we used a 480nm BPF (Chroma D480/30X) which was close to the 494 nm excitation peak of calcein AM, and

also an acceptable wavelength for exciting ethidium homodimer since at this wavelength it has an absorbance greater than 50% of its peak value which is at 528nm (according to the manufacturer's chart). Between the mercury lamp and the filter we mounted an electromechanical shutter (Oriel 71456) which we were able to drive with the same TTL pulse normally used to drive the LED. For calcein AM we used a 535 nm emission filter (Chroma D535/40M) which is close to the 517 nm emission peak. For ethidium homodimer we first attempted to use a 630nm bandpass filter (Chroma D630/60M) which is close to the 617 nm emission peak. However, this filter also had transmission around 480 nm which made it unacceptable in our diafluorescence arrangement (something which is not a problem for epifluorescence because of the dichroic). We then found a red glass filter of unknown origin in the lab which enabled us to carry out our experiments, and have since ordered a new bandpass filter (Chroma D620/40M) which is closer to the excitation peak and has no adverse transmission at shorter wavelengths.

Our goal was to first image in the deep UV and then add the live-dead kit to assess cell viability. We first tried using perfusion chambers as described above, but the process of removing the media, rinsing with PBS, and adding dye was sufficiently disruptive that it was unlikely that the same cell would remain unperturbed in the field of view. We found it much more practical to use our standard imaging chambers and to add the live/dead stain to the media before the chamber was sealed. Although this presented the risk that the stains would interfere with our UV images, it was worth this risk in order to test the effectiveness of the kit in a reliable way.

During our experiments, the cells glowed green as expected when living. As expected and as shown in **Fig. 44** – the green still dominated after 69 exposures of 100ms each, separated by 1 minute intervals. However, we then exposed the cell to 181 10-second exposures separated by 1 second each, and the green still dominated the red signal even though the cell appeared visibly dead. The cell had clearly undergone necrosis, but the only red signal was a slight one that appeared to be bleed-through. We then took a time-lapse of red images over the next 2.5 hours, during which time the nucleus slowly glowed brighter and brighter red. By the end of this time, the red signal was on par or greater than the green. Even with our imperfect filter setup, the conclusion here is still clear – it takes some time after the cell dies for the ethidium homodimer to diffuse into

the nucleus and form a fluorescent compound. We saw similar behavior on dead cells which appeared green initially, but when left cold overnight glowed bright red in the nucleus. We therefore concluded that examining the cell morphology was a faster and

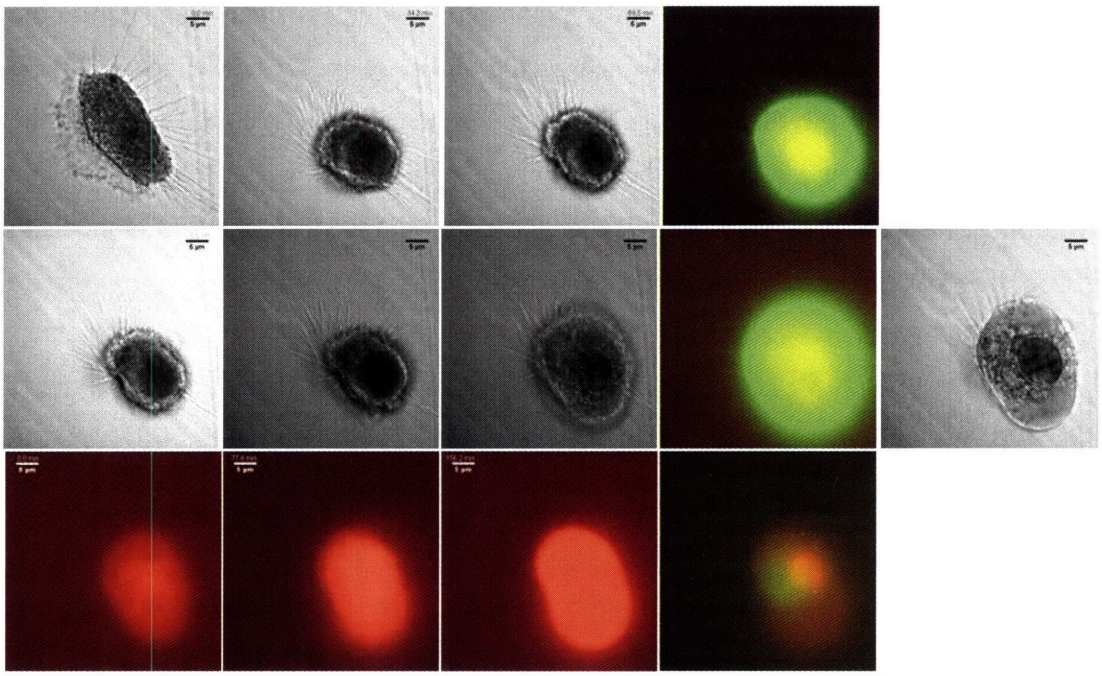

**Fig. 44:** Data from live/dead kit experiments, showing that cell morphology is a faster determinant of cell death than the live/dead kit. (**top row**) Time lapse images of 69 100ms exposures, followed by a live/dead image. (**second row**) Time lapse images of 181 10sec exposures with 1sec in between, followed by a live/dead image and an image after 11 more 10 sec exposures. (**third row**) Time lapse of ethidium homodimer (dead kit) over ~2.5 hours, followed by a live/dead image.

more accurate means than the live-dead kit for determining whether the cells were alive or not.

### 5.9 Live-Cell Native Fluorescence

**Fig. 45** shows time lapse images of IC-21s imaged in native fluorescence mode using 10 second exposures, the very minimum necessary to produce an image of any value. Even with this long exposure time, the images do not have particularly high signal-to-noise ratio, yet the long exposures cause necrosis of the cell. We are still working on

ways to increase the signal and decrease the noise sufficiently to enable live-cell native fluorescence imaging.

Another source of noise for live-cell imaging is protein in the media surrounding the cells. Standard DMEM has 16mg/L of tryptophan[68], which is small compared to the concentration of protein in cells, but a bigger problem seems to be the Fetal Bovine Serum which is added to the media and has many proteins. We have tried replacing the media with PBS which does reduce the background significantly, but the cells do not live long in just PBS and have very altered behavior. We will also look at artificial media to reduce this background. Many challenges still need to be overcome in order to successfully produce live-cell native fluorescence images.

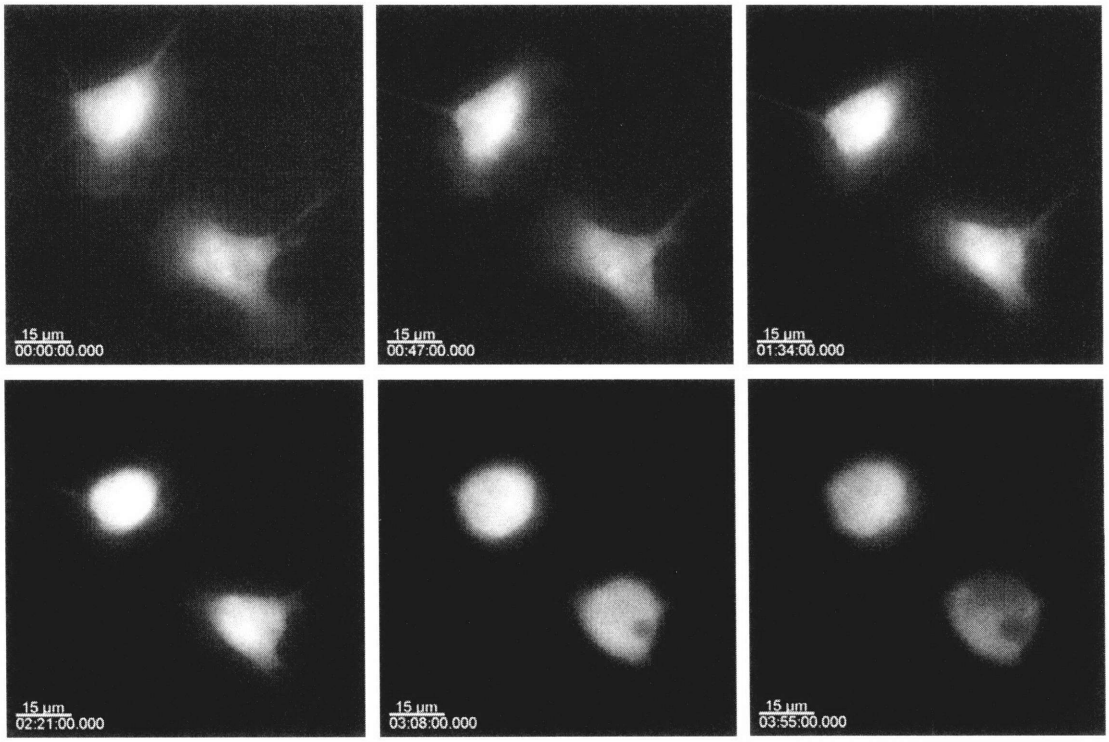


**Fig. 45**: Time-lapse images of IC-21 native fluorescence using 10 second exposures separated by 60 second dark time. The cells clearly undergo necrosis. It is interesting to note that the background noise decreases, possible due to bleaching of proteins in the media.

## Chapter 6: Protein and Nucleic Acid Mass Mapping

### 6.1 Mapping Theory and Implementation

Deep UV microscopy intrinsically records quantitative molecular information. In a deep UV transmission image the intensity of a given pixel, $I$, and the intensity of the same pixel in a blank field of view, $I_O$, together determine the optical density (OD) at that pixel, by the Beer-Lambert law typically used in spectroscopy:

$$OD_\lambda = \log_{10}\left(\frac{I_O}{I}\right) = \varepsilon_\lambda cl$$

The measured OD at wavelength λ is a function of sample concentration, $c$, pathlength, $l$, and extinction coefficient, ε. The terms optical density and absorbance (ABS) are often used interchangeably, but optical density can result from absorbance or scattering effects. For our initial work we assume that optical density equals absorbance, and discuss correction for scattering in chapter 8. Interpreting deep UV OD image data is more challenging than interpreting spectroscopy data because the pathlength is determined by the height of the cell which varies with position and because protein and nucleic acid both contribute significantly to the measured OD in proportion to their concentrations [20]:

$$OD_\lambda(x,y) = \varepsilon_\lambda^{\,protein} c^{protein}(x,y)l(x,y) + \varepsilon_\lambda^{\,nucleicacid} c^{nucleicacid}(x,y)l(x,y)$$

where λ is wavelength, $c$ is sample concentration, $l$ is pathlength, and ε is the extinction coefficient. To determine the mass of protein and nucleic acid at each pixel, we acquire transmission and background images at both 260nm and 280nm. We estimate that $\varepsilon_{260}^{nucleicacid}$ = 7,000 $M^{-1}cm^{-1}$ by averaging known extinction coefficients for DNA and RNA at 258 nm, [69] and because pure nucleic acid has $OD_{260}/OD_{280}$ =2.0,[17] we estimate that $\varepsilon_{280}^{nucleicacid}$=3,500 $M^{-1}cm^{-1}$. Next we estimate that $\varepsilon_{280}^{protein}$ = 54,129 $M^{-1}cm^{-1}$ and $\varepsilon_{260}^{protein}$=36,057 $M^{-1}cm^{-1}$ using the extinction coefficients for tryptophan, tyrosine, and phenylalanine at 260 nm (3,787 $M^{-1}cm^{-1}$, 582 $M^{-1}cm^{-1}$, and 147 $M^{-1}cm^{-1}$) and at 280 nm (5,559 $M^{-1}cm^{-1}$, 1,197 $M^{-1}cm^{-1}$, and 0.7 $M^{-1}cm^{-1}$) in neutral solution,[70]

an average 466 amino acid protein [71], and the tryptophan, tyrosine, and phenylalanine frequencies (1.4%, 3.2%, and 3.9%) [72]. Inserting these values into the above equation for each wavelength yields two linear equations that together determine the values of $c^{nucleicacid}l$ and $c^{protein}l$ at each pixel. Multiplying these concentration-pathlength products by the area of each pixel yields the quantity of each in moles. Using an average molar mass of 52,728 Da for protein [71] and of 330 Da for nucleic acid [73] yields the mass of each. Displaying this value at each pixel yields the nucleic acid mass and protein mass contained in the volume defined by that pixel projected through the cell, i.e. a nucleic acid map and a protein map, as shown in **Fig. 46** [66]. The values can also be plotted for a line section through the nucleus.

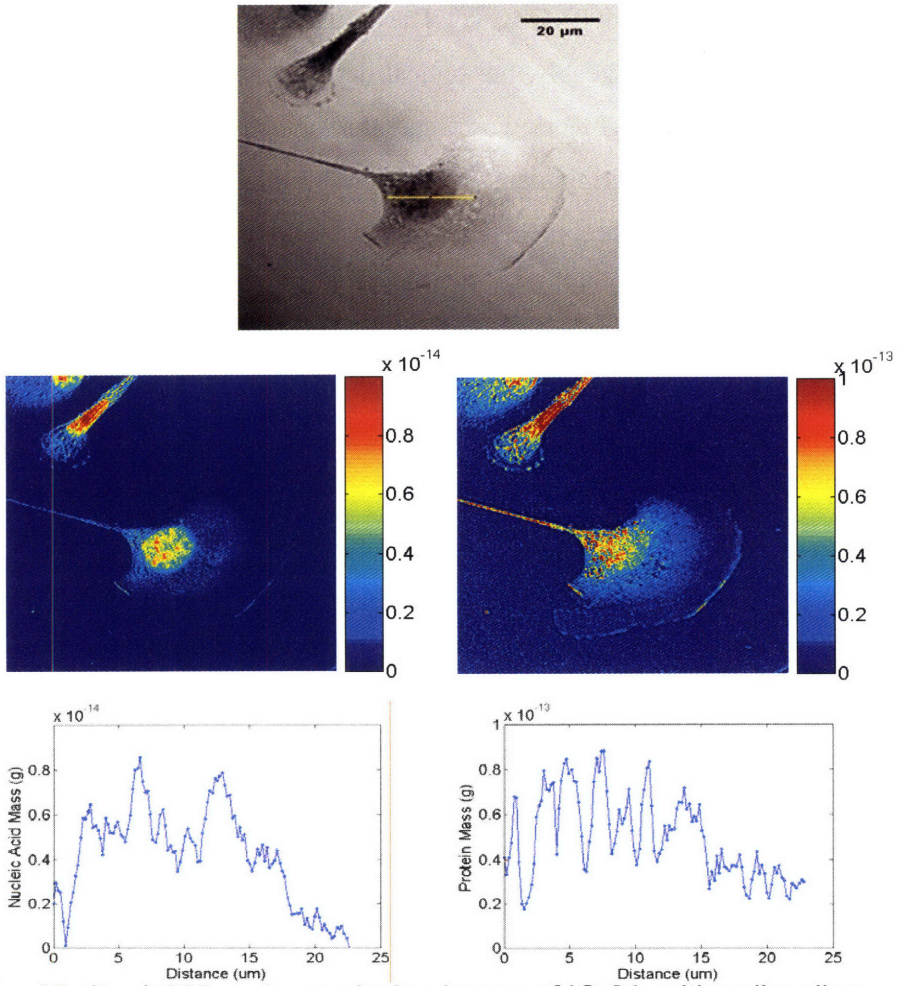


**Fig. 46:** (**top**) 280nm transmission image of IC-21, with yellow line indicating location of line plots in bottom row. (**middle left**) Nucleic acid mass map. (**middle right**) Protein mass map. (**bottom left**) Line plot of nucleic acid mass. (**bottom right**) Line plot of protein mass.

The maps show nucleic acid heavily concentrated in the nucleus with some in the surrounding area, while protein concentration is high in the nucleus but also throughout the cell and in the leading edge and tail. The line plots show sharp increases in protein and nucleic acid at different points in the nucleus, which may indicate the presence of chromosomes and nucleoli as well as other structures. While the mass values are pathlength-independent, we can convert them to concentrations in mg/ml using an assumed pathlength $l$ = 8μm for the nucleus. The concentrations then peak around 270mg/ml for protein and 27mg/ml for nucleic acid, values which compare favorably to published concentration estimates of protein (100-300mg/ml) and nucleic acid (26-46mg/ml) (see **Table 3**).

| **DNA** | **RNA** | **Protein** |
|---|---|---|
| ~ **15mg/ml** (6pg DNA per cell,[74] nucleus ~1/10 of cell volume $4x10^{-9}$ $cm^3$ typical)[75]<br>~**18.5mg/ml** (56mM nucleosome concentration,[76] 200 bp/nucleosome, 2bases/bp,1Mbase/330g.[73]<br>~**19 mg/ml** [77]<br>~**20-31 mg/ml** (8.1-12.5pg/cell,[78] nucleus ~1/10 of cell volume $4x10^{-9}$ $cm^3$ typical )[75] | ~**11 mg/ml** (5-25pg RNA per cell,[79] 18% in nucleus,[80] nucleus ~1/10 of cell volume $4x10^{-9}$ $cm^3$ typical).[75]<br>~**12-15mg/ml** (27.1-33.1pg/cell,[78] 18% in nucleus,[80] nucleus ~1/10 of cell volume $4x10^{-9}$ $cm^3$ typical).[75] | ~**106-215 mg/ml** in various regions of the nucleus.[81]<br>~**108mg/ml** (6pg DNA per cell,[74] protein mass 72X DNA mass and cell volume $4x10^{-9}$ cm3 typical).[75]<br>~**200-300mg/ml** in E.coli.[82] |

**Table 3:** Published concentration estimates of protein and nucleic acid in cells.

Maps were calculated by MATLAB software (MathWorks, Natick MA) using the equations described above. Code is in the appendix. Prior to calculation a mean offset ("dark value") of the camera was subtracted from each intensity. For the protein and nucleic acid maps, the maximum displayed values were set to $1x10^{-13}$ g and $1x10^{-14}$ g

respectively for the tube lens images with 190 nm pixels, and to $2x10^{-14}$ g and $2x10^{-15}$ g respectively for the non-tube-lens images with 92 nm pixels.

A question has been raised regarding how many proteins are in each volume element, and whether it is valid to use the approximate percentages. In a 92nm square pixel with an assumed pathlength of 8μm, the total volume is $6.7x10^{-14}$ $cm^3$ or ml. Using our estimated peak of 270mg/ml, this corresponds to $1.8x10^{-14}$ g of protein. With an assumed molar mass of 52,728 Da per protein, this corresponds to $3.5x10^{-19}$ mol of protein, or $2.1x10^5$ proteins. We believe that 210,000 proteins is enough that the statistics of amino acid frequency will remain valid.

### 6.2 Mapping Protein and Nucleic Acid Mass in Fixed Mitotic Chromosomes

We next acquired 260nm and 280nm images of fixed mitotic HMLER (oncogenically transformed human mammary epithelial cells generously plated for us by Sandy McAllister, MIT Weinberg Lab) during anaphase, in order to examine the distribution of protein and nucleic acid mass during mitosis. The results are shown in **Fig. 47**. The condensed chromatin in chromosomes appears as areas of extremely concentrated nucleic acid mass which correlate with a corresponding ten-fold higher protein concentration. Interestingly, while the chromosomes contain more protein by mass, the protein seems to define a narrow core region while DNA seems more dispersed. One theory is that this core region corresponds to the nonhistone protein scaffold visualized by electron microscopy in extracted chromosomes [2], which would lend support to the controversial idea that this scaffold exists in vivo [83],[84], but much more evidence is needed to prove this conclusively, since these patterns could also reflect scattering or other artifacts which would make the 260nm image appear more grainy, as discussed further in subsequent chapters.

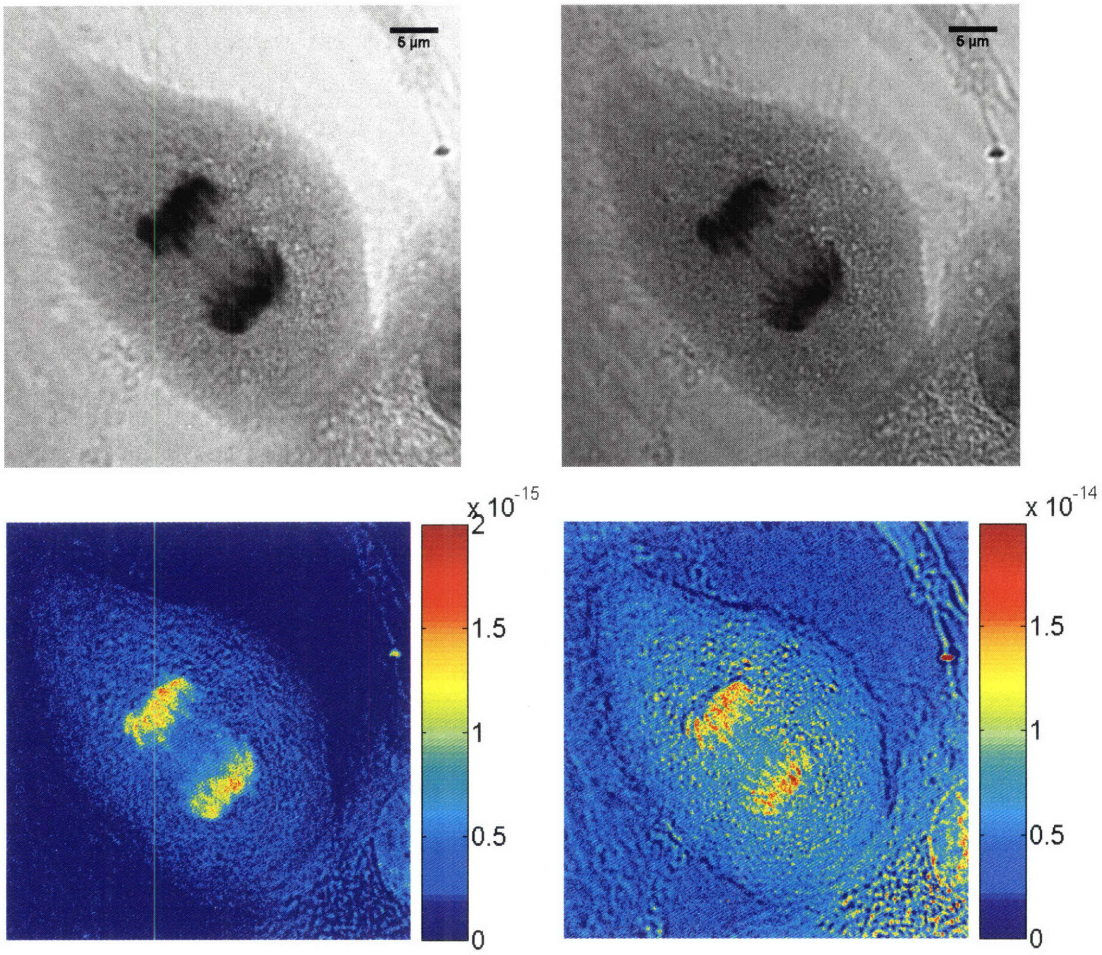


**Fig. 47:** (**top left**) 260nm and (**top right**) 280nm transmission image of fixed mitotic HMLER cell. (**bottom left**) Nucleic acid and (**bottom right**) protein mass map.

## Chapter 7: Quantum Yield Mapping

### 7.1 Mapping Theory and Implementation

Using a native fluorescence image we can then calculate the quantum yield, $q$, of protein at each pixel. The protein mass map is critical for this calculation because it allows us to calculate the $OD_{280}$ due to protein alone, independent of nucleic acid concentration. Protein quantum yield is commonly measured in solution to assay the molecular environment surrounding the fluorophore [31]. The contribution of tryptophan is dominant in our native fluorescence images because the next strongest fluorophore, tyrosine, is weaker, more easily quenched [69], and has an emission maximum shorter than the 320 nm cut-on wavelength of our filter. The fluorescence intensity, $I_{AF}$, is determined by the basic equation:

$$I_{AF} = q \cdot I_O \cdot \left(1 - 10^{-OD^{tryptophan}}\right)$$

However, we provide a few modifications since the native fluorescence measurements are made with a different emission filter and a different exposure time than the transmission images, and the fraction of native fluorescence that reaches the camera is determined by the objective lens collection angle:

$$I_{AF} = \left(\frac{T_{AF}}{T_{trans}}\right)\left(\frac{Eff_{AF}}{Eff_{trans}}\right)\frac{\sin^{-1}\left(\frac{NA}{n_{immersion}}\right)}{2 \cdot \pi} \cdot q \cdot I_O \cdot \left(1 - 10^{-OD^{tryptophan}}\right)$$

where $T_{AF}$ and $T_{trans}$ are the exposure times and $Eff_{AF}$ and $Eff_{trans}$ are the transmission efficiencies of the emission filters used for the native fluorescence and transmission images respectively. $NA$ is the numerical aperture of the objective lens and $n_{immersion}$ is the refractive index of the immersion media. The optical density due to tryptophan, $OD^{tryptophan}$, can be calculated from four values in the previous chapter: the $c^{protein}l$ value, the average number of amino acids per protein, the average tryptophan frequency, and the tryptophan extinction coefficient at 280 nm. The $I_O$ is the same for our transmission and fluorescence images since the microscope utilizes a diafluorescence arrangement, and can be determined from a transmission image of a blank field. The above equation then determines the quantum yield at each pixel, which can be displayed as a map or for a line section through the nucleus, as shown in **Fig. 48**. The images were calculated in

MATLAB (MathWorks, Natick MA) using code that appears in the appendix, and the quantum yield map display range was set from 0 – 0.12.

The map shows lower quantum yield in areas including the nucleus and leading edge of the cell. One untested hypothesis to explain this observation is that in these areas proteins are more densely packed and therefore experience more quenching. The line plot also is interesting when compared with the line plot for protein mass showing some peaks in quantum yield corresponding to valleys in protein mass.

In addition, the quantum yield values compare favorably to published values. For the line plot through the nucleus, the quantum yield centers around 0.04. Published values of $q$ for 20 isolated proteins [70] have a mean of 0.125± 0.071. One untested hypothesis is that our lower results reflect additional quenching in the closely packed environment of the cell. Another possibility is that the lower values are caused by scattering effects which would masquerade as absorbance due to tryptophan, lowering the quantum yield.

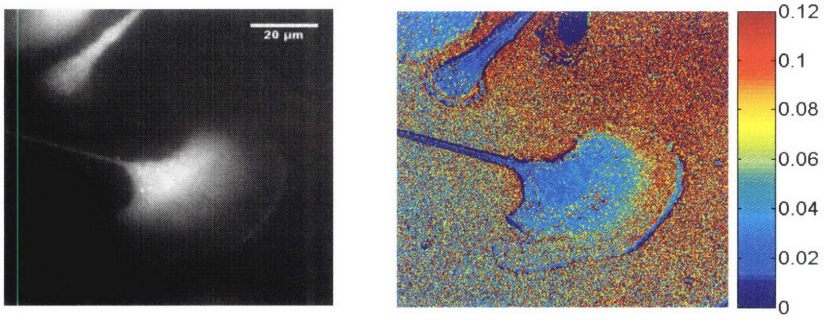


**Fig. 48:** (**left**) Native fluorescence image and (**right**) calculated tryptophan quantum yield image for the same fixed unlabeled IC-21 shown in the previous chapter.

The calculation described above assumes constant quantum efficiency for the camera over the wavelengths of interest. According to the camera manufacturer's specifications, this is true up to ~375nm, but at longer wavelengths the quantum efficiency starts to increase. However, this issue may be balanced out by another assumption built into our calculations – that the transmission efficiency of the bandpass filter for the native fluorescence measurement is a constant 92% independent of wavelength. This is true at most wavelengths of interest, but not right around the cut-on wavelength of 320nm. Since these two assumptions have opposite effects, we believe

that they may cancel each other out to some extent. Even if they do not completely cancel, they will only affect the absolute value of the quantum yield map, and will not affect the relative quantum yield map – so the relationships between the quantum yields at each pixel will remain unchanged. The quantum efficiency curve for the camera, transmission efficency of the long-pass filter used for native fluorescence emission, and the emission spectrum of tryptophan in solution are all shown in **Fig. 49**.

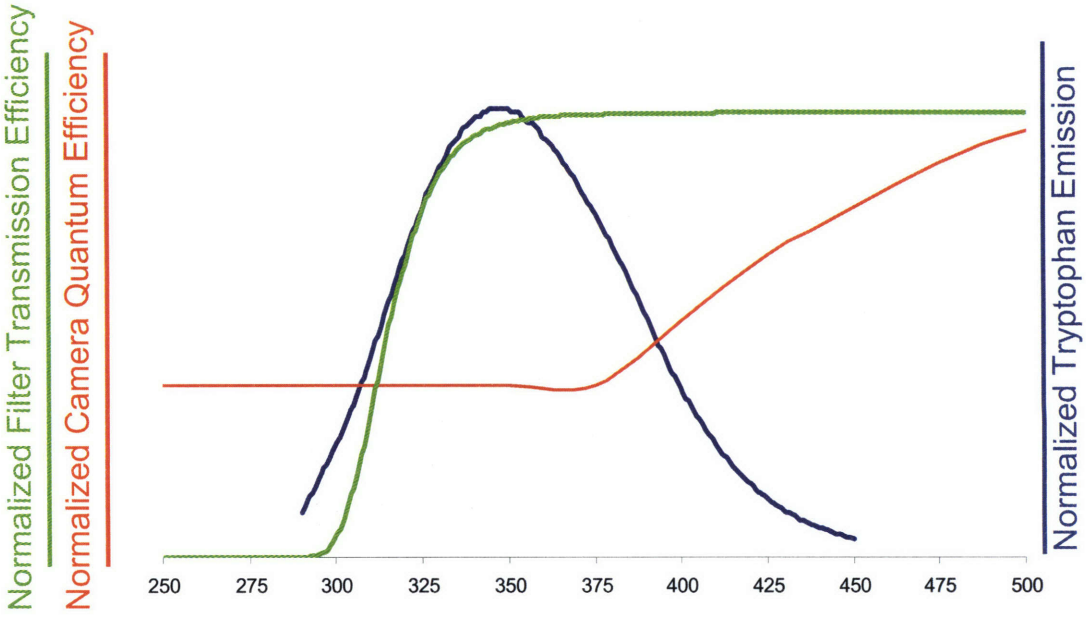


**Fig. 49:** (**red**) Normalized approximate quantum efficiency of our camera as a function of wavelength in nanometers, from manufacturer's specifications, (**green**) Normalized approximate transmission efficiency of our 320nm longpass filter from manufacturer's specifications, (**blue**) Normalized approximate emission spectra of tryptophan in solution, from our fluorimeter measurements.

Another analysis method we explored provided a way to estimate the approximate protein mass in the absence of a 280nm image. By assuming a constant quantum yield at each pixel and then working backwards from the native fluorescence image, it is possible to determine the mass of tryptophan and by extension the total protein mass. However, we believe this method will be less accurate due to the variations in tryptophan quantum yield.

We have chosen to call the phenomenon measured here "quantum yield" in order to match the spectroscopy literature and because we believe this term encapsulates the dominant phenomenon occurring. However, we note that an argument could be made for calling it "fluorescence yield" since this term might encompass a broader range of possible phenomena that could reduce the fluorescence.

## 6.2 Mapping Quantum Yield in Fixed Mitotic Chromosomes

We applied the quantum yield analysis technique to calculate the quantum yield of fixed mitotic HMLER (oncogenically transformed human mammary epithelial) cells during anaphase, in order to examine the quantum yield during mitosis. The results are shown in **Fig. 50**. The chromosomes appear to have significantly lower quantum yield than the rest of the cell. One untested hypothesis is that this represents quenching from the densely packaged environment. Another possibility is that these images could also suffer from scattering artifacts as discussed further in the next chapter.

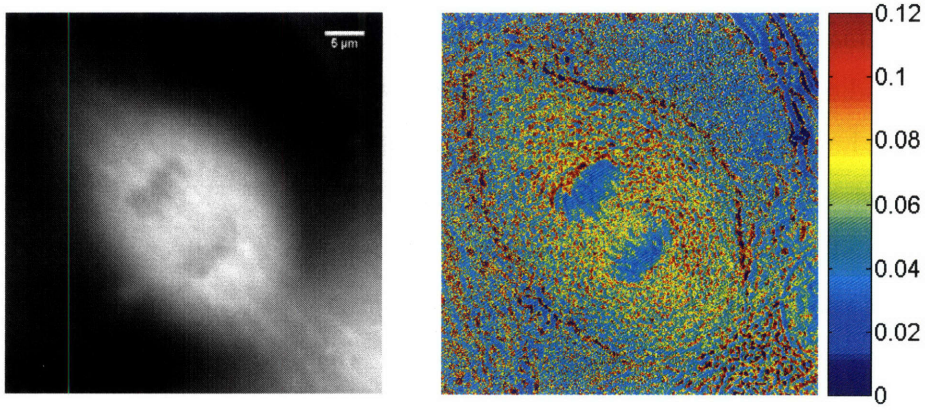


**Fig. 50:** (**left**) Native fluorescence image and (**right**) calculated tryptophan quantum yield image for a fixed mitotic HMLER cell.

## Chapter 8: Scattering Correction

In Chapter 6 we described a method for imaging cells at 280nm and 260nm, determining the optical densities at each wavelength, and then calculating the mass of protein and of nucleic acid at each pixel. This method relies on the stated assumption that optical density equals absorbance. Since optical density measures extinction which can be caused by both absorbance and scattering, we have implicitly assumed that scattering effects are negligible.

The same assumption is often made in spectroscopy studies, and scattering is rarely mentioned when spectra appear in literature associated with biological research. Nevertheless, several methods have been developed to characterize and correct for scattering effects in biological samples. Such corrections are important for imaging because measurements are made at much higher protein concentrations.

### 8.1 Rayleigh Scattering Corrections in Literature

The magnitude of the extinction caused by scattering is a function of several factors including the size of the scattering particles and the wavelength $\lambda$ of the incident light. In the limiting case when the particles are much smaller than the wavelength of the incident light, the extinction due to scattering is approximately proportional to $\lambda^{-4}$. This case is referred to as Rayleigh scattering. By measuring the optical density of a sample at wavelengths where it is known to have negligible absorbance, the optical density due to scattering at those wavelengths can be determined. Then, using the $\lambda^{-4}$ relationship, the contribution to optical density from scattering can be calculated at wavelengths where there is significant absorbance.

As a demonstration of this technique, Freifelder uses the extinction of bacteriophage from 325nm-400nm to determine that the optical density due to scattering is 0.4 at 260nm, roughly 7% of the total measured OD of 5.4 at this wavelength [69].

A slightly more robust way to characterize Rayleigh scattering assumes that the extinction due to scattering is approximately proportional to $\lambda^{-n}$, where $4<n<2$. Again, by measuring the optical density of a sample at wavelengths where it is known to have

negligible absorbance, the optical density due to scattering at those wavelengths can be determined and the value of *n* extracted [85].

A third approach is described in a review and attributed to Moberger, who measured optical density of freeze-dried cells at 315nm, and calculated the scattering at 265 nm using two relationships, $\lambda^0$ and $\lambda^{-4}$, which presumably represented the range of possible values [19]. Interestingly, Moeberger apparently found a much higher scattering contribution for freeze-dried cells than Freifelder did for bacteriophages – at a minimum about 20% of the total optical density at 265nm. Writing at around the same time, Caspersson has yet another approach to the problem, conducting an extensive analysis of scattering from cells before concluding that it should not significantly influence absorbance measurements as long as the particles are larger than $3\lambda$/(index of refraction) and other conditions are met such as the objective having a large numerical aperture [20].

### 8.2 Rayleigh Scattering Corrections for Imaging

Based on these approaches, we acquired transmission images of an IC-21 at 320nm and 340nm, wavelengths where there is negligible absorbance from protein and nucleic acid, in addition to 260nm and 280nm, and determined the OD at each wavelength as shown in **Fig. 51**. In order to extrapolate the contribution due to scattering at 280nm and 260nm, we first subtracted the OD340 from the OD320 value for a set of five images (more than 1.3 million pixels) but unexpectedly found that an average of 22% of the pixels had an OD340 value higher than the OD320 value, the opposite of the relationship expected from Rayleigh scattering. See **Fig. 52** for an example. This suggested that a significant portion of the pixels did not experience major Rayleigh scattering, and so applying such a correction would introduce an unacceptably high amount of noise into our images.

### 8.3 Mie Scattering Corrections for Imaging

The results from the previous section made it clear that the key assumption upon which the Rayleigh scattering equation was based, that the particles are much smaller than $\lambda$, was not accurate for a significant portion of our images. We then turned to the

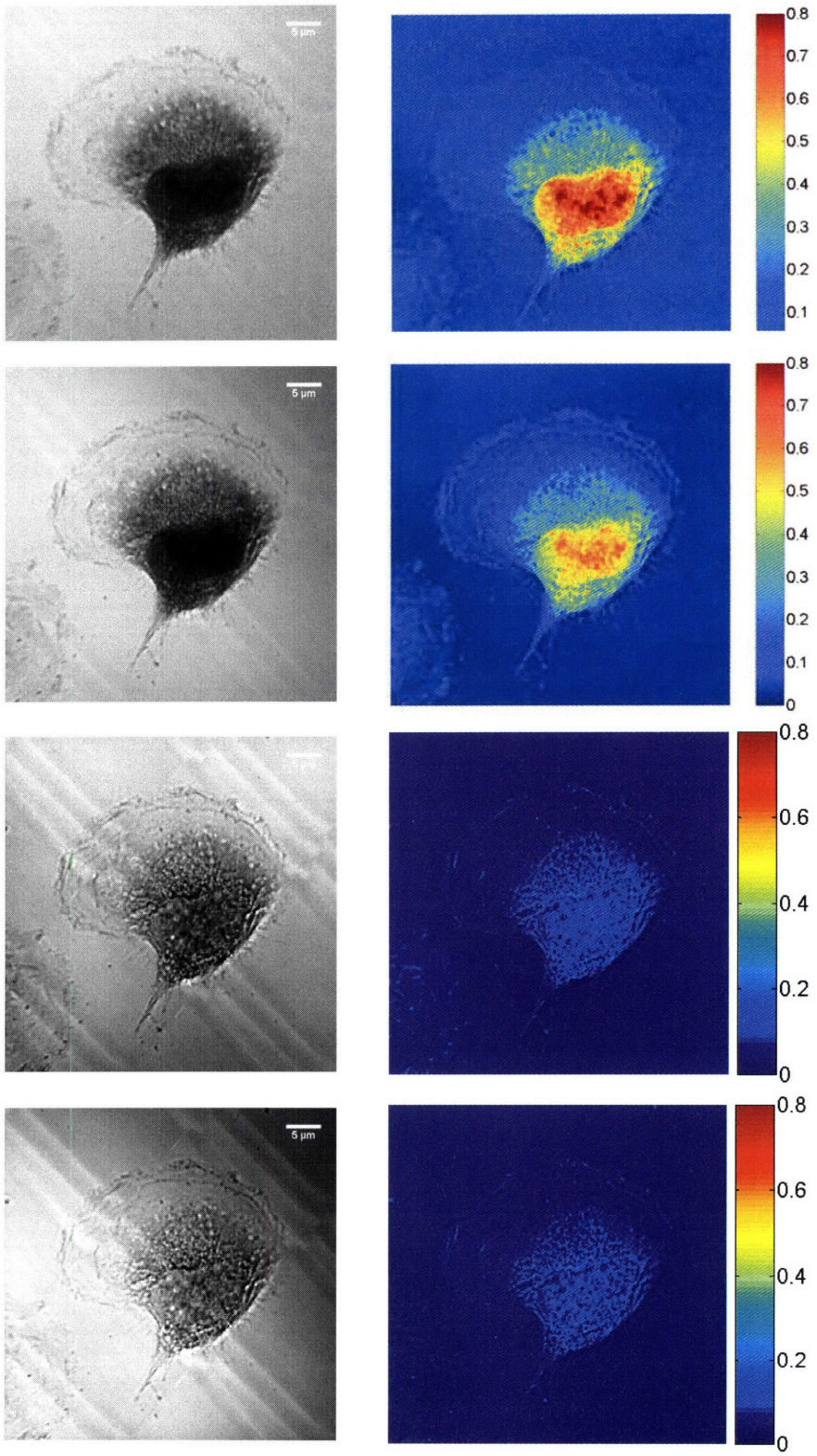


**Fig. 51:** (**left column**) Transmission images and (**right column**) OD images for (**first row**) 260nm, (**second row**) 280nm, (**third row**) 320nm, and (**fourth row**) 340nm.

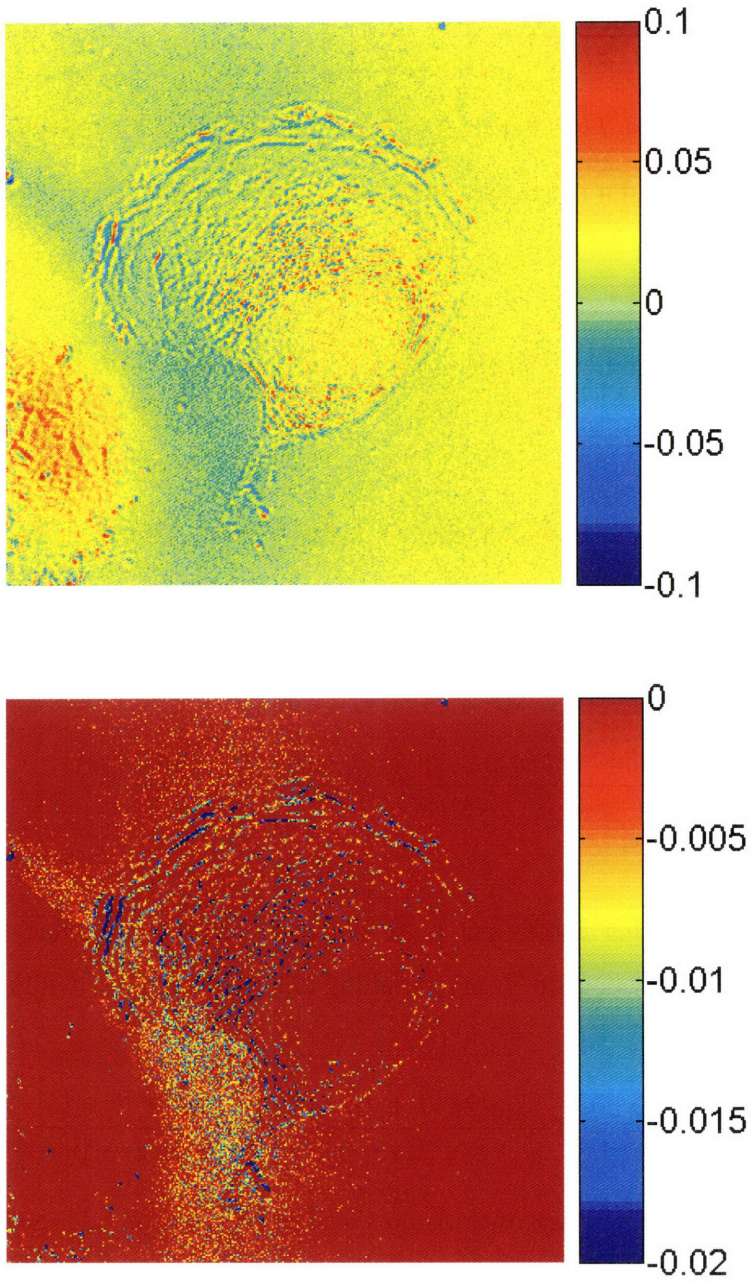


**Fig. 52:** OD320 minus OD340 at each pixel, for (**top**) a more complete display range, and (**bottom**) a display range set to emphasize location of of negative values. Future work could investigate why the negative values seem more prevalent in the thinner areas of the cell – somewhat contrary to what one would expect for a type of scattering caused by larger particles.

more general Mie scattering theory, using the Van de Hulst approximation for scattering cross section $\sigma_s$ as described in the literature [86]:

$$\sigma_s(\lambda,l)=\frac{1}{2}\cdot\pi\cdot l^2\left[1-\frac{\sin(2\delta/\lambda)}{\delta/\lambda}+\left(\frac{\sin(\delta/\lambda)}{\delta/\lambda}\right)^2\right]$$

where $\delta=\pi\cdot l\cdot n_c(n-1)$, $l$ is the diameter of the particles, $n_c$ is the refractive index of the medium (cytoplasm) and n is the refractive index of the object. Substitution of the value for δ yields:

$$\sigma_s(\lambda,l)=\frac{1}{2}\cdot\pi\cdot l^2\left[1-\frac{\sin(2\pi\cdot l\cdot n_c(n-1)/\lambda)}{\pi\cdot l\cdot n_c(n-1)/\lambda}+\left(\frac{\sin(\pi\cdot l\cdot n_c(n-1)/\lambda)}{\pi\cdot l\cdot n_c(n-1)/\lambda}\right)^2\right]$$

According to another paper which also uses the Van de Hulst approximation, for a collimated beam the scattering coefficient $\mu_s$ can be determined by multiplying the scattering cross section by the number density of spheres $N_s$ [87]:

$$\mu_s=N_s\cdot\frac{1}{2}\cdot\pi\cdot l^2\left[1-\frac{\sin(2\pi\cdot l\cdot n_c(n-1)/\lambda)}{\pi\cdot l\cdot n_c(n-1)/\lambda}+\left(\frac{\sin(\pi\cdot l\cdot n_c(n-1)/\lambda)}{\pi\cdot l\cdot n_c(n-1)/\lambda}\right)^2\right]$$

To convert the scattering coefficient $\mu_s$ to the more familiar εc value from the Beer Lambert law, we simply convert from natural log to log base ten by dividing it by 2.303:

$$\varepsilon_{scattering}c=N_s\cdot\frac{1}{4.606}\cdot\pi\cdot l^2\left[1-\frac{\sin(2\pi\cdot l\cdot n_c(n-1)/\lambda)}{\pi\cdot l\cdot n_c(n-1)/\lambda}+\left(\frac{\sin(\pi\cdot l\cdot n_c(n-1)/\lambda)}{\pi\cdot l\cdot n_c(n-1)/\lambda}\right)^2\right]$$

For the cytoplasm index of refraction we used a value of 1.35, and for the object index of refraction we used a value of 1.46 [88]. We wrote this equation in MATLAB (Mathworks, Natick MA) (code in appendix) and used a nonlinear fit command to extrapolate the values of $N_s$ and $l$ that best fit our measured OD320 and OD340 values the values at each pixel. We then used these values to extrapolate a

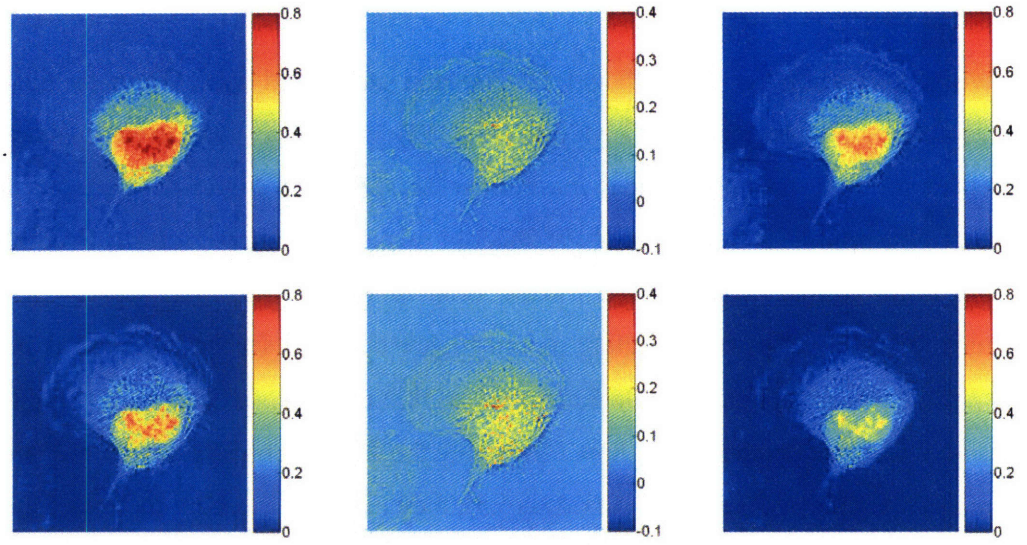


**Fig. 53:** (**left column**) Original OD value, (**middle column**) calculated OD correction factor, and (**right column**) corrected OD value, for (**top row**) 260nm and (**bottom row**) 280nm.

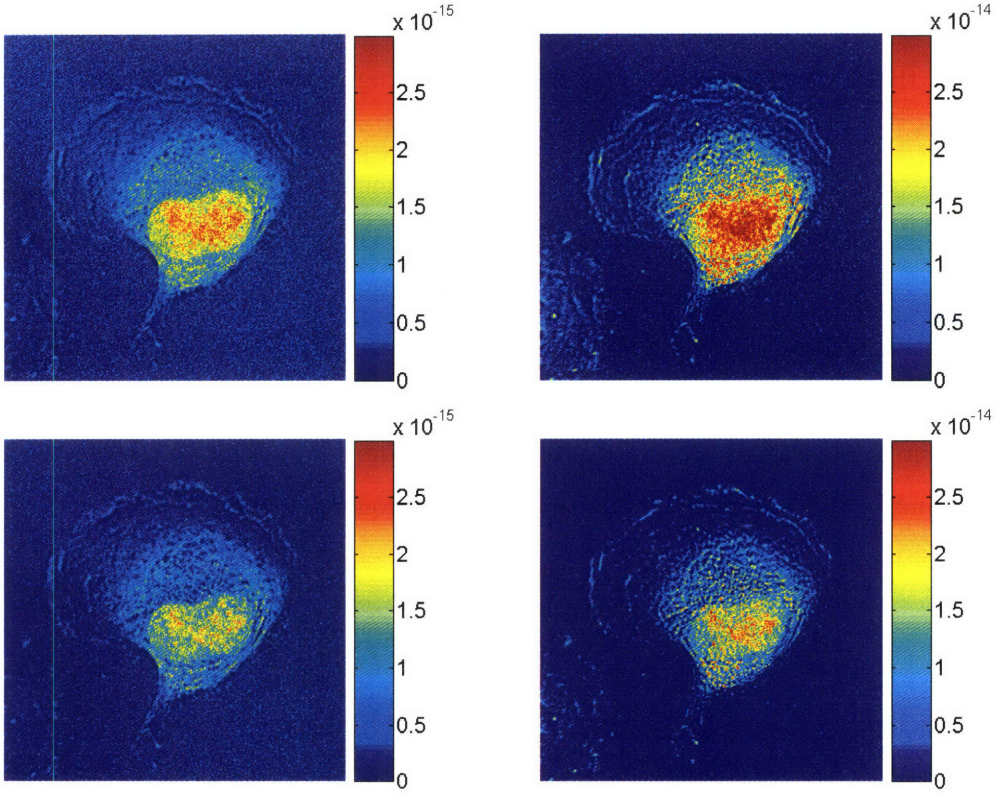


**Fig. 54:** (**top row**) Uncorrected and (**bottom row**) scattering-corrected mass maps in grams for (**left column**) nucleic acid and (**right column** ) protein.

scattering correction for OD280 and OD260 and subtracted these from original OD values to produce corrected OD values **(Fig. 53)** which we then used to determine corrected protein and nucleic acid mass maps as shown in **Fig. 54**. Because this is performing a nonlinear fit at each of the 262,144 pixels in an image, it takes over 3 hours to run on a "normal" computer (2.8 GHz Xeon processor, 3.37GB Ram, about 190.5 minutes to run). When run remotely on our higher powered servers, it takes as little as ~26.7 minutes (on Kahuna), while Karma takes 38.0 minutes. However, the duration is extremely variable depending on how effectively the fit converges. Because Kahuna and Karma run an older version of MATLAB (6.5), they display a warning message when the fit does not converge, which cannot be turned off and which slows the computation to the point that it is impractical to use the servers for most images. Future work could investigate using special processors or better fitting algorithms to accelerate this process.

### 8.4 Effect of Scattering Correction on Quantum Yield

We have not yet determined an effective method for scattering-correction of the native fluorescence images. This is more challenging because these images include a range of wavelengths, and because the geometry is different than it would be for transmission images. However, because these images are at longer wavelengths, it is likely that scattering has a less significant effect. Using uncorrected native fluorescence images, and the scattering-corrected protein mass map, we can determine a slightly more accurate quantum yield map as shown in **Fig. 55**. Generally, the scattering correction lowers the protein mass values which in turn elevates the quantum yield, bringing it closer to the literature values for proteins in solution. The scattering corrected quantum yield image also has much less noise in the background outside the cell.

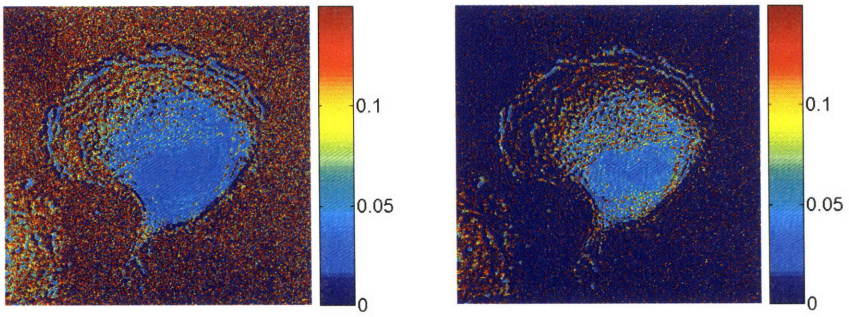


**Fig. 55:** Quantum yield map determined with (**left**) uncorrected and (**right**) scattering-corrected protein mass maps.

## 8.5 Error Sources and Future Directions

We believe that the resulting scattering-corrected images are an accurate reflection of the mass in cells. However, this correction rests on a number of assumptions. First, we have assumed that Rayleigh scattering from smaller particles can also be modeled by this Mie equation, an assumption which may introduce some additional error into our calculations. A comparison of the curve shapes produced by our equation and the Rayleigh equation for 10nm diameter particles is shown in **Fig. 56**. Secondly, this equation is based on a solution of spheres of uniform diameter. While each volume element contains many different sized scattering objects, the correction parameter we extract is essentially an averaged value. We assume that this does not contribute significantly to the error. Third, we assume that any NADH fluorescence excited by the 320nm and 340nm light is negligible. While this assumption seems reasonable for fixed cells, our work with live-cell scattering correction has found this to be a significant error source and so we are implementing bandpass filters in the emission path to avoid this. Finally, for the scattering corrected quantum yield, we assume that any scattering of the emitted fluorescence is negligible. Future work would attempt to quantify or eliminate the need for these assumptions, or in cases where these assumptions contribute significantly to error, it may be better not to apply such a correction, accepting the

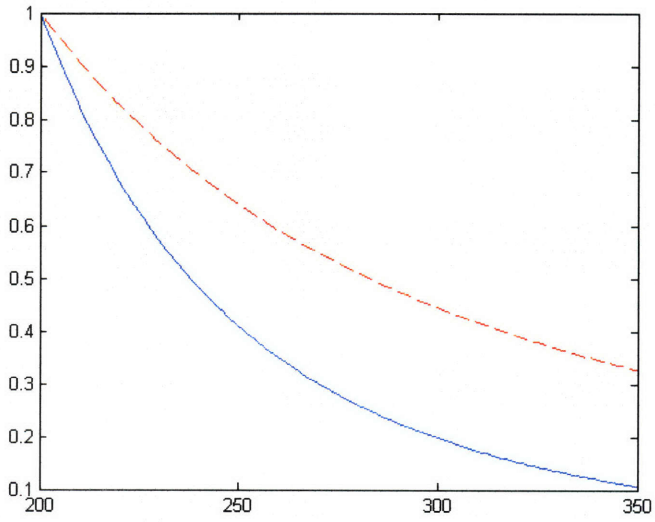


**Fig. 56:** For an object of diameter 10nm (much less than λ), curves comparing the shapes of scattering magnitude as a function of wavelength in nm, for (**red dashed line**) the Mie approximation equation and (**solid blue line**) the Rayleigh scattering ($\lambda^{-4}$) approximation; each independently normalized by its own maximum.

scattering error in order to remain closer to the raw data and avoid adding noise to our images.

Another source of error occurs when the nonlinear fit does not converge, in which case the correction values may be somewhat inaccurate.

### 8.6 Impact of Scattering-Correction on Fixed Mitotic Chromosome Images

We also applied this scattering correction to images of fixed mitotic chromosomes in order to determine the impact of this correction on the protein scaffold hypothesis, as shown in **Fig. 57**.

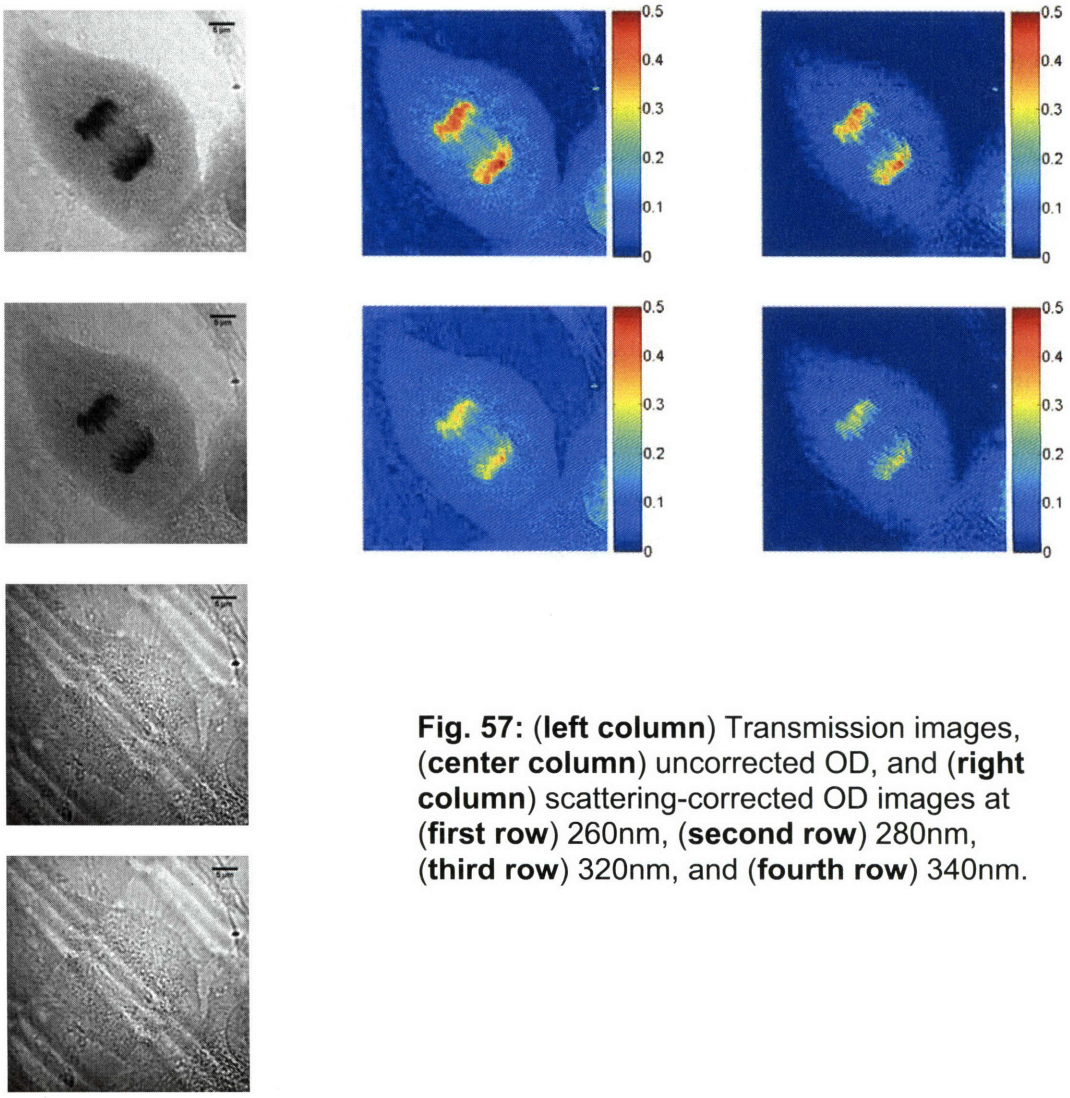


**Fig. 57:** (**left column**) Transmission images, (**center column**) uncorrected OD, and (**right column**) scattering-corrected OD images at (**first row**) 260nm, (**second row**) 280nm, (**third row**) 320nm, and (**fourth row**) 340nm.

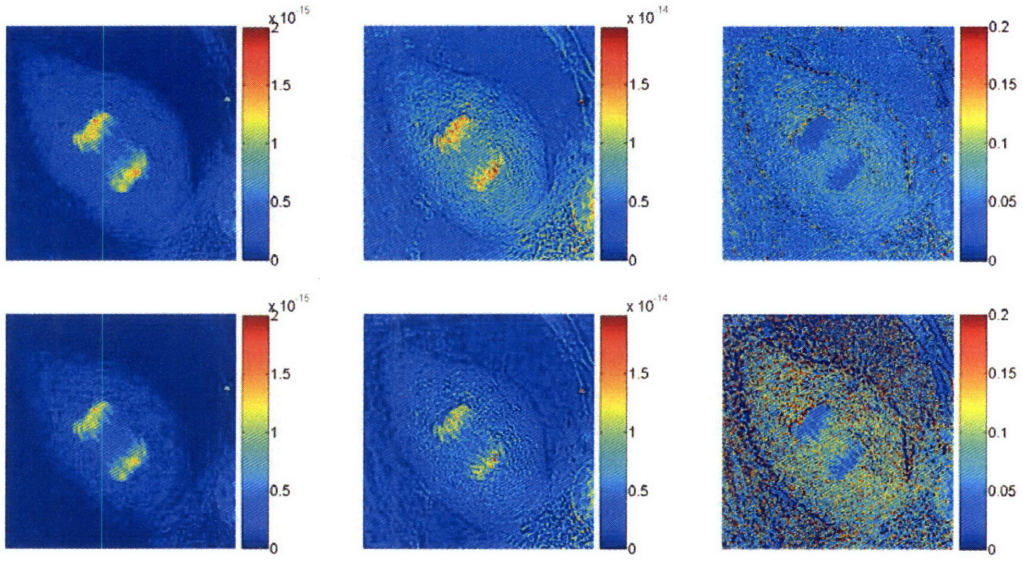


**Fig. 58:** (**top row**) Uncorrected and (**bottom row**) scattering-corrected maps of (**left column**) nucleic acid mass, (**center column**) protein mass, (**right column**) and tryptophan quantum yield.

Using these values, we then calculated scattering-corrected mass maps and quantum yield maps, as shown in **Fig. 58**. While this correction somewhat reduces the differences between protein and nucleic acid distribution, these differences still remain. To further explore how these newly scattering-corrected mass maps address the scaffold-hypothesis, we used several different approaches to analyze them. Because the protein mass values are approximately an order of magnitude higher than the nucleic acid mass values, we first subtracted the nucleic acid mass values from the protein mass values as shown in **Fig. 59 (left)**. However, this result appeared virtually identical to the protein mass values

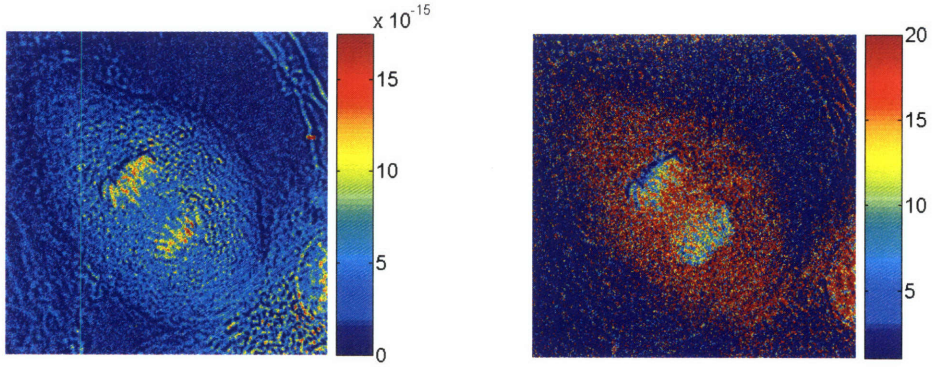


**Fig. 59:** (**left**) Protein mass minus nucleic acid mass, and (**right**) Protein mass divided by nucleic acid mass.

because the nucleic acid mass values are so small in comparison. We also tried taking the protein mass divided by the nucleic acid mass, but the results were fairly noisy as shown in **Fig. 59 (right).**

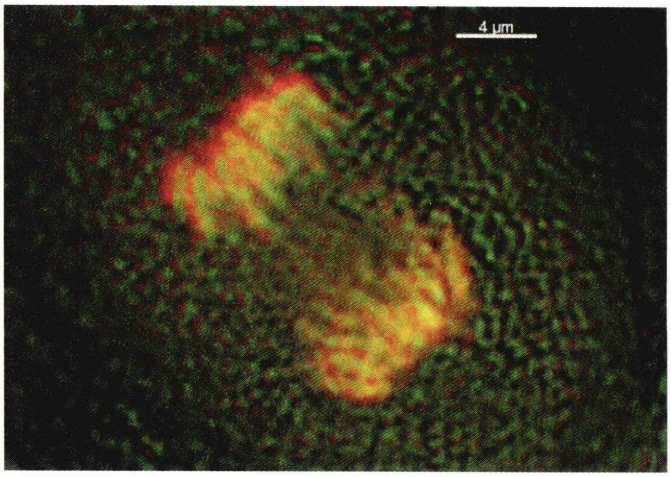


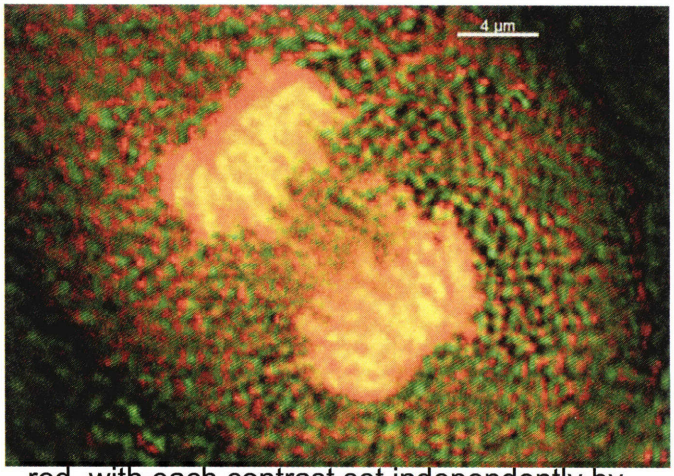


red, with each contrast set independently by autocontrast. (**bottom**) Same except contrast ranges set by hand.

We then multiplied each of mass maps by an arbitrary scaling factor (protein by $10^{18}$ and nucleic acid by $10^{19}$, and saved them out of MATLAB as 16-bit tiff files. We used Imaris to display them simultaneously, with nucleic acid on the red channel and protein on the green channel. The results varied dramatically depending on how the display range for each was set. See **Fig. 60**.

Finally, we opened the protein mass and nucleic acid mass images separately in ImageJ and took a line plot across the chromosomes for each one. We then took the values from these line plots, and normalized each one by its maximum value. The results are plotted together in **Fig. 61**.

Here, finally, the differences become more clearly visible. The protein values vary more sharply and over a shorter distance, while the nucleic acid values vary more slowly. The sharp, narrow protein peaks could represent a protein scaffold, or some artifact such as a wavelength-dependent response of the camera or filter. Also interesting is that in several

cases the protein peaks line up with nucleic acid valleys. This could be cause by areas of more protein versus areas of more nucleic acid, or could occur because the two images are slightly out of alignment due to chromatic aberration.

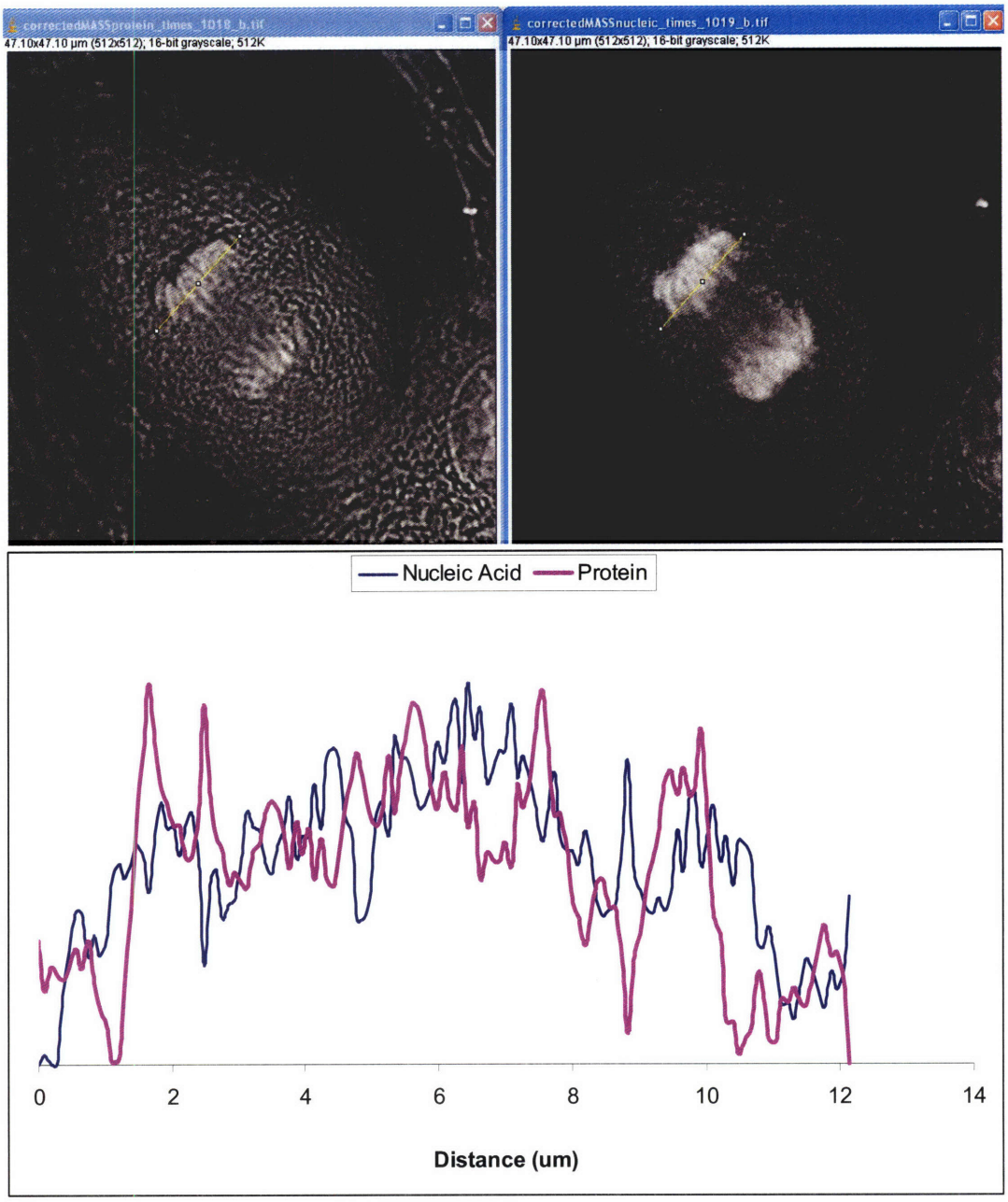


**Fig. 61:** (**top left**) Protein mass image showing location of line plot. (**top right**) Nucleic acid mass map image showing location of line plot. (**bottom**) Line plot of protein mass and nucleic acid mass, each independently normalized.

## Chapter 9: Live Cell Multiple Wavelength Imaging

### 9.1 Real-Time Live-Cell Protein and Nucleic Acid Mass Maps

Initially our live-cell time-lapse imaging work was restricted to 280nm, because the LED output at 260nm was sufficiently weak that very long exposures (on the order of 10 seconds) were necessary to produce an image with even a minimally adequate signal-to-noise ratio. The problem was caused primarily by the fact that the 260nm LED output is specified to be ~0.1mW – $1/10^{th}$ the output of the 280nm LED. This problem is exacerbated by lower transmission of the fiber, condenser, and objective at shorter wavelengths. We attempted to produce higher output power by using an 8-junction 260nm LED, but it proved difficult to couple the emission from all the junctions into the fiber simultaneously, and we found it equally efficient to use a single junction LED carefully coupled into the fiber. The 260nm LEDs also seem to have a shorter lifetime than the 280nm LEDs. We discovered the key to increasing the power somewhat serendipitously while using a special half-thickness (0.5mm) quartz slide (SPI supplies) rather than our standard 1mm thickness quartz slides (Chemglass, Vineland NJ). The result was a dramatically improved signal. While this may be due in part to less absorption from the smaller amount of quartz, we believe that the most significant effect is due to the fact that the shorter slide brings the sample closer to the focal point of the condenser. Because the condenser lens has a fairly short working distance, the thickness of the adhesive frame used to create the media chamber for live-cell imaging means that the sample is outside the plane of maximum intensity of illumination. Reducing the thickness of the slide diminishes this problem.

The second challenge that had to be overcome in order to implement time-lapse protein and nucleic acid mapping of live cells was switching the inputs. Our initial goal was to use a y-splitter fiber assembly and simply alternate which LED was turned on. A y-splitter assembly is three fibers that are all connected at one central point, so that the two leg fibers couple into a single fiber. It was important to have this design rather than the more common bifurcated cable assembly, in which two fibers are simply placed side-by-side in the same connector, because a bifurcated assembly would be illuminating the field of view from slightly different angles. We were able to obtain a custom y-splitter

assembly with a large diameter from Ocean Optics, but since the process of making the junction for the bifurcated cable is inefficient we found that the transmission efficiency from input to output was ~ 20%. This was not acceptable on our already limited power budget.

As a more practical option, we used a motorized filter wheel (ThorLabs, Newton NJ) and replaced the filters with SMA fiber connectors, and also placed an SMA fiber connector in the output path. As shown in **Fig. 62**, we connected a fiber from this output path to the microscope input, and attached fibers from each of the light sources to the fiber connectors in each of the filter positions. When a particular filter position was selected, light was close-coupled from one of the input fibers to the output fibers. While this close-coupling process is inefficient and causes ~50% loss, this was a better option than the y-splitter cable. The motorized filter wheel also can be computer-controlled via an RS232 cable, and has a BNC TTL output signal that can be set to trigger when the filter was in position. To utilize this arrangement, we wrote MATLAB code to control the filter wheel (see appendix), alternating between the 260nm LED fiber and the 280nm LED fiber at intervals controlled by the code. Each time the filter wheel reaches position, the TTL pulse is used to trigger the camera.

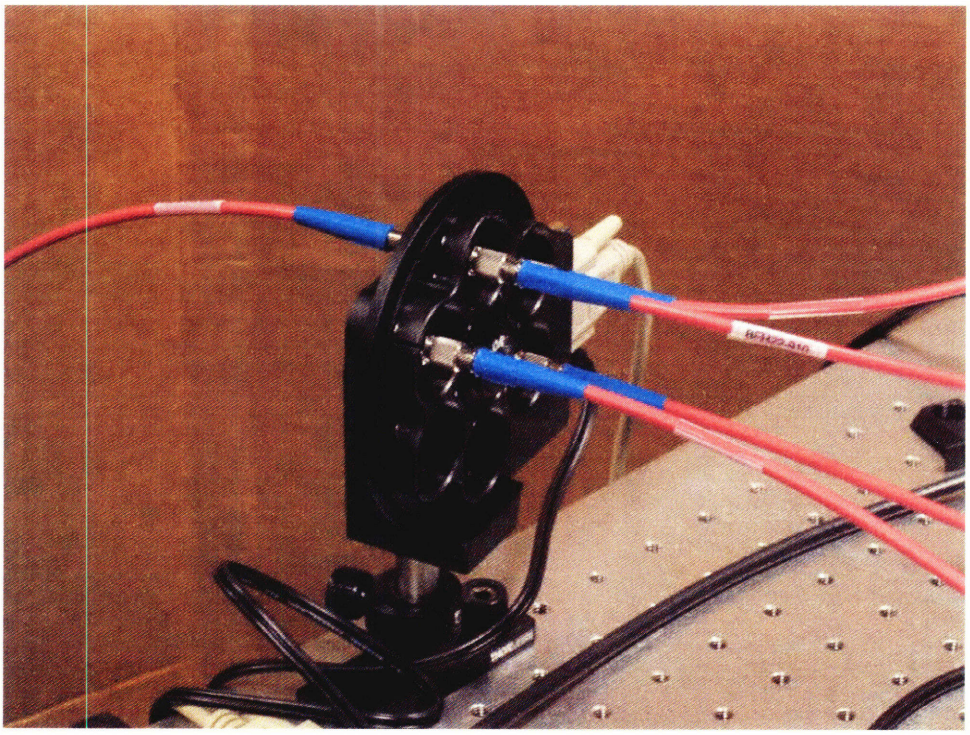

**Fig. 62:** Motorized filter wheel for switching fiber input.

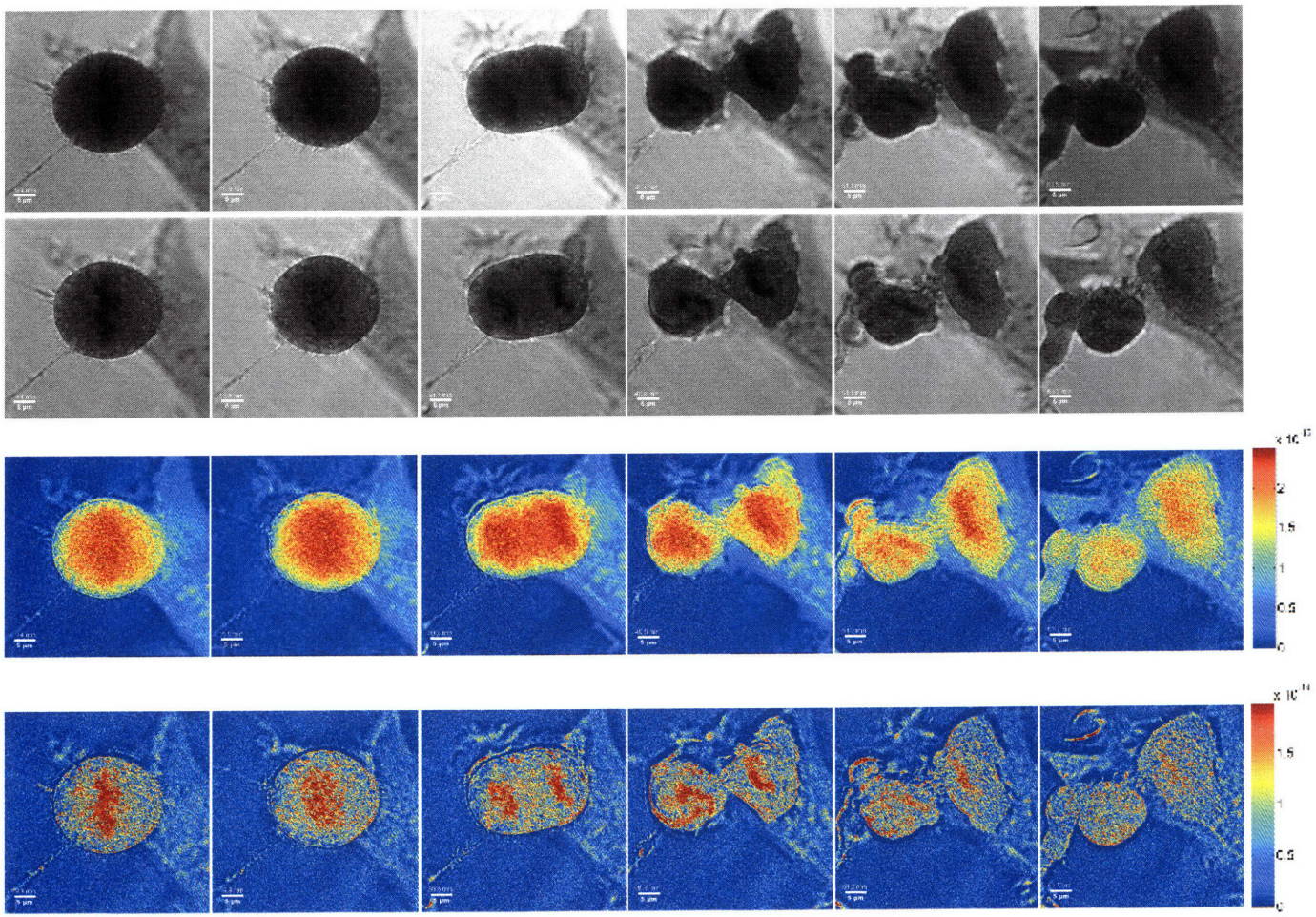

**Fig. 63:** 2λ Imaging of HT-1080 mitosis. (**top row**) Time-lapse 260nm images. (**second row**) Time-lapse 280nm images. (**third row**) Time-lapse nucleic acid mass map with units in grams. The DNA appears to be obscured by significant scattering effects. (**bottom row**) Time-lapse protein mass map with units in grams.

The camera software functions in such a way that the result is a single file of tiff images, with images that alternate between 260nm and 280nm, so we wrote additional MATLAB code to separate and write these out as separate tiffs.

Because the LED outputs vary somewhat over time, we took several measures to correct for these variations in excitation intensity. We took a blank field image for at least 10 exposures at each wavelength, and averaged these at each pixel in order to create a robust background. This robust background image represented the correct spatial distribution of intensity for the blank field, but may not have represented the correct absolute intensity. Next, we chose a square of pixels in the image which remains blank throughout the entire time lapse, and averaged the pixels in this square at each time point. Then, we divided the mean of the pixels in this blank square of the image file by the mean of the pixels in the corresponding square of the robust background image. The result was a unique scaling factor for each timepoint that we applied to the robust background image before calculating the OD at that time point. This successfully improved the consistency and corrected for variations in output.

Using this method, our MATLAB code calculates the protein map and nucleic acid map at each timepoint and writes them out as images. The results are shown in **Fig. 63**. Here the nucleic acid mass map seems desperately in need of scattering correction, but to do so requires imaging at additional wavelengths.

### 9.2 4 λ Imaging

In order to have the ability to drive 4 different LEDs, we rapidly constructed two additional driver circuits. Attaching these to the fiber-selecting filter wheel, we were able to alternate between the four wavelengths to collect the time-lapse images, but these were taken with no emission filter, so the 260nm and 280nm images contain error due to the native fluorescence of tryptophan and tyrosine, while the 320nm and 340nm images contain error due to the native fluorescence of NADH. To improve the accuracy we needed to include a motorized filter wheel in the emission path, but simply adding between the c-mount and the camera lengthened our tube and degraded image quality since the filters were so close to the camera and we do not have an infinity-corrected system. In order to more the filter wheel further from the camera, we removed the

camera tube and drilled a ThorLabs B2C threaded plate to match the screw locations of the Zeiss camera tube and used a hacksaw to cut the edges of the baseplate so it would fit. The result was an SM1 threaded adapter onto which we could mount a lens tube followed by a motorized filter wheel, then another lens tube and the camera. This allowed us to alternate between both excitation sources and emission filters as shown in **Fig. 64**.

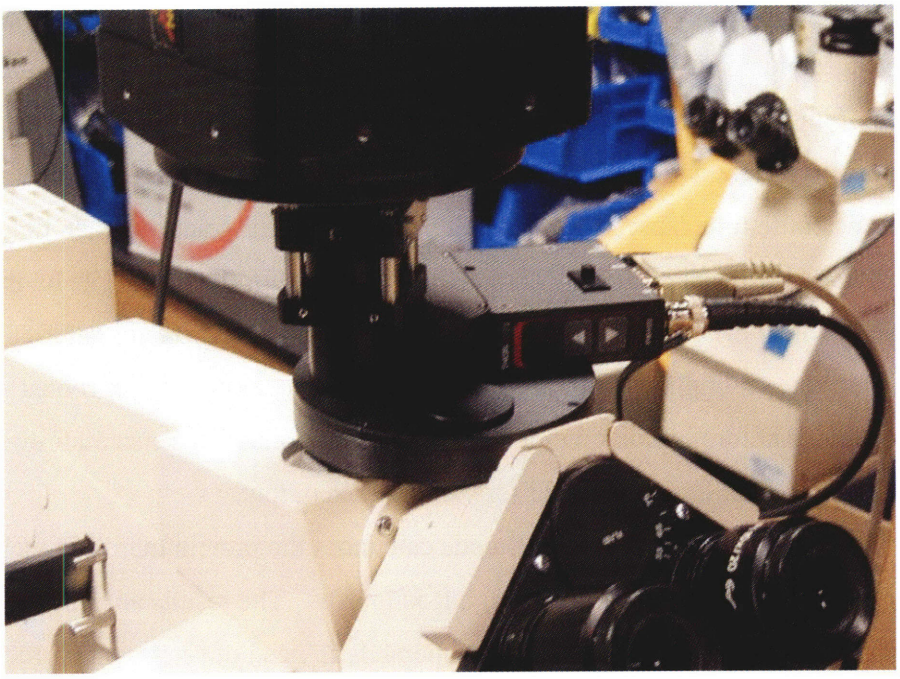

**Fig. 64:** Motorized filter wheel for switching emission filters.

We altered the timing so that the excitation filter wheel moves into position, and then after a 1.5 second pause the emission filter wheel moves into position and triggers the camera. We did this because there is less pressure on the emission filter wheel and so it will click into place with less bouncing. However, we still saw strong variations in excitation intensity, which could be a result of movement in the excitation filter wheel or else may be cause by changes in the LED drivers themselves. Relieving some of the strain on the fibers entering the filter wheel helped alleviate this issue. The results are shown in **Fig. 65 and 66.** However, the scattering-correction procedure suffers from significant lensing and NADH fluorescence artifacts so severe that in some cases the corrected mass is higher than the uncorrected mass. We have begun taking 4 wavelength live-cell images using 320nm and 340nm bandpass emission filters in order to block fluorescence, and are working to determine how effective this approach is.

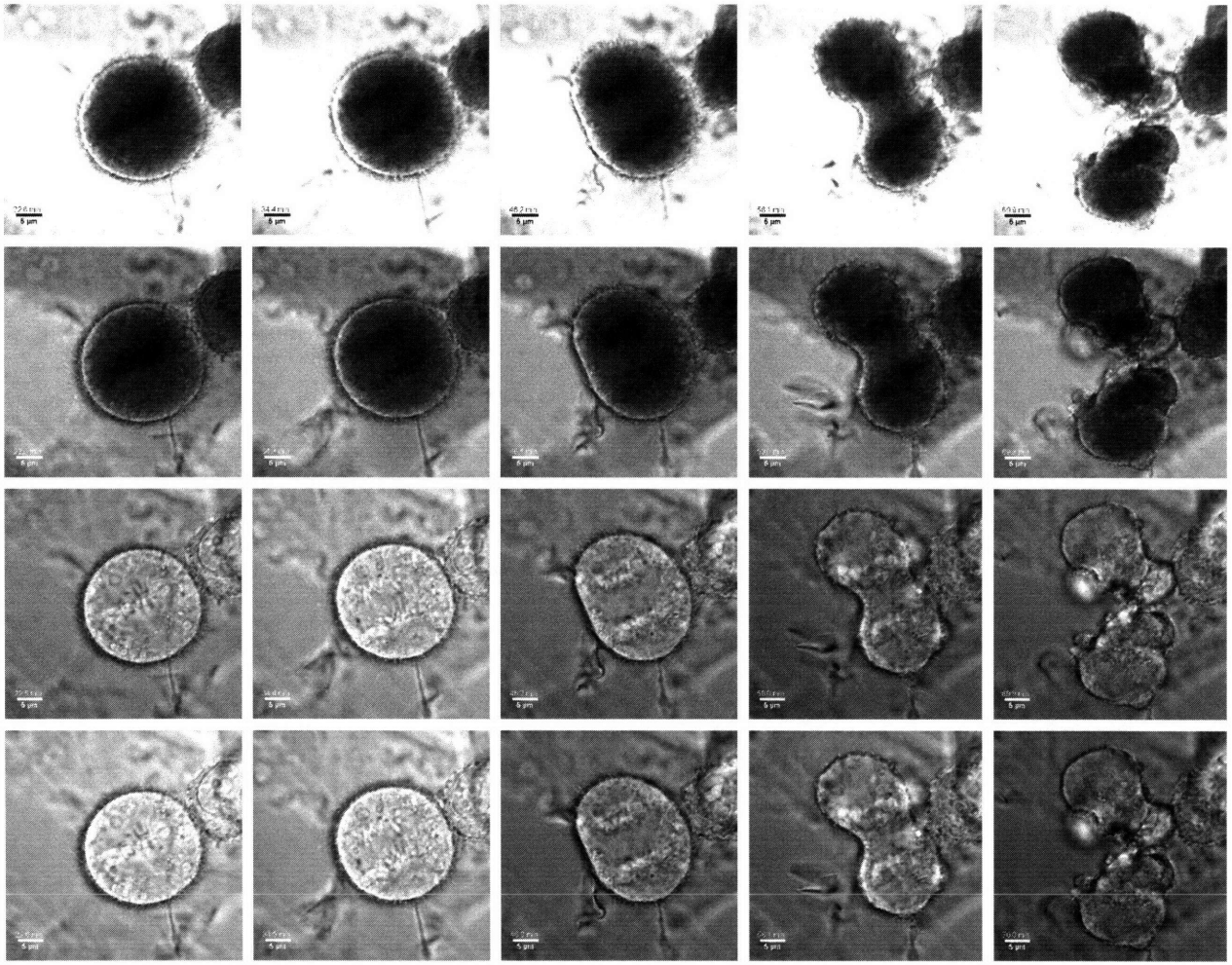

**Fig. 65:** 4 λ Time-lapse images of HT-1080 mitosis. (**top row**) 260nm, (**second row**) 280nm, (**third row**) 320nm, and (**bottom row**) 340nm.

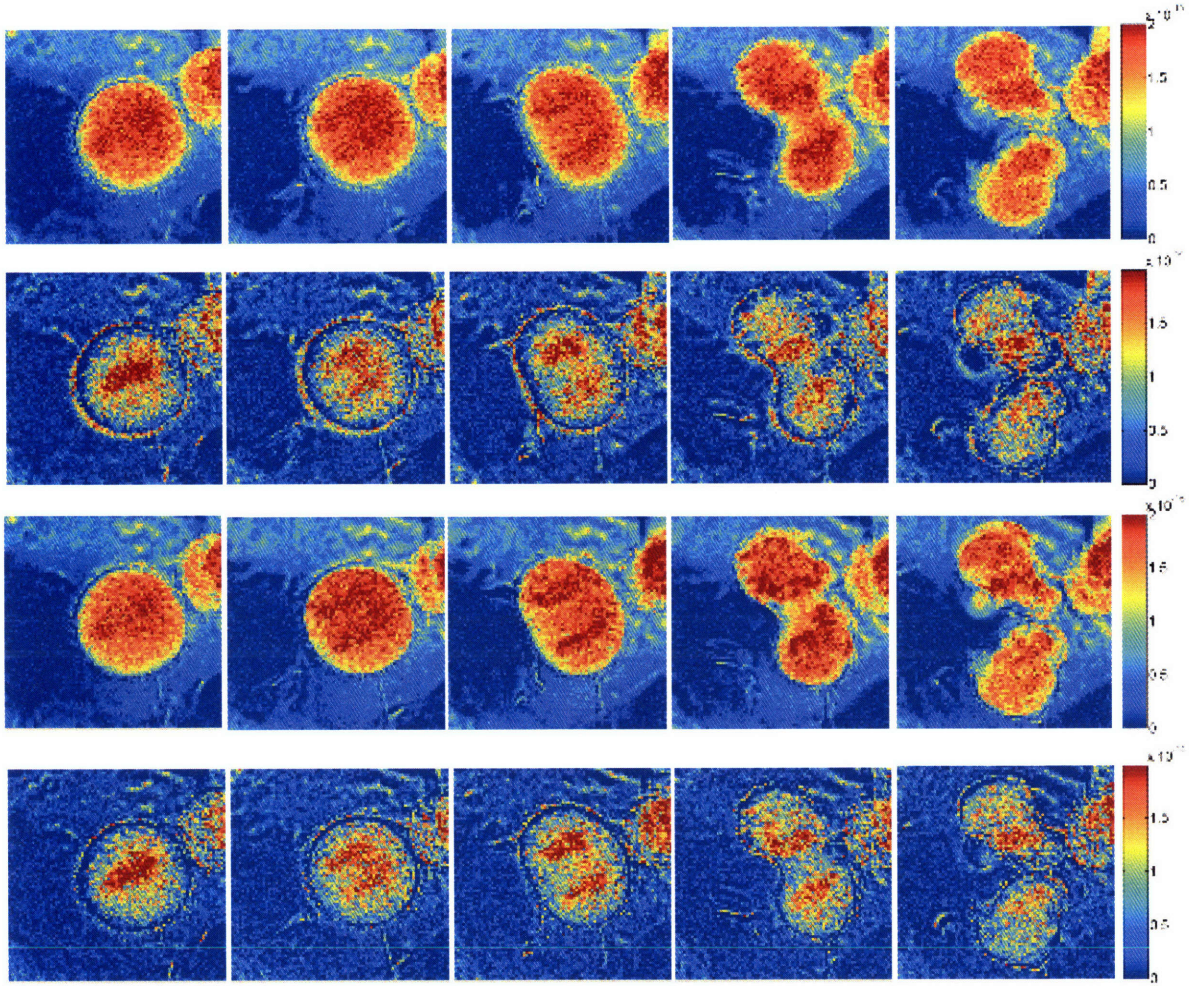

**Fig. 66:** Time-lapse mass maps of HT-1080 mitosis with units in grams. (**top row**) Uncorrected nucleic acid mass, (**second row**) uncorrected protein mass, (**third row**) incorrectly scattering-corrected nucleic acid mass due to NADH fluorescence and lensing, and (**bottom row**) incorrectly scattering-corrected protein mass due to NADH fluorescence and lensing.

## SYSTEM CHARACTERIZATION, VALIDATION, AND ERROR ANALYSIS

### Chapter 10: Validation Experiments in Channels

#### 10.1 Validation Procedure

Early scope validation experiments were performed using a channel etched in fused silica designed for electrophoresis. However, when we switched from the reflecting objective to the Ultrafluar, our working distance no longer allowed us to focus into the channel. Additionally, since the channel had a curved bottom there appeared to be some lensing effects which added error to our quantitation.

We explored other approaches to imaging solutions for calibration, including sealing them between a slide and a coverslip. When the solution filled the entire area underneath the coverslip, the results were inconclusive because there was nothing to focus on and therefore no way to set the focus properly. Caroline Jordan then suggested the idea of placing a very small volume of fluid between the slide and the coverslip so that the edge was visible. This was an improvement because it gave us something to focus on, but still was inconclusive because the pathelength was unknown, there was lensing from the edge of the spot, and the fluid seemed to quickly dry out and also change over time (perhaps with pressure from the objective. Sealing the edges with nail polish did not solve these problems.

Finally, we found a reasonably effective way to validate the UV absorbance measurements recorded by the UV microscope: measuring the absorbance and fluorescence of purified protein and nucleoside solutions in a PDMS flow channel device. Each channel was approximately 100μm in diameter and was plasma-bonded to a quartz coverslip (Electron Microscopy Sciences, Hatfield PA). The devices were skillfully and generously prepared for us by Johnson Hou in the Manalis Lab. An image of one of these devices appears in **Fig. 67**.

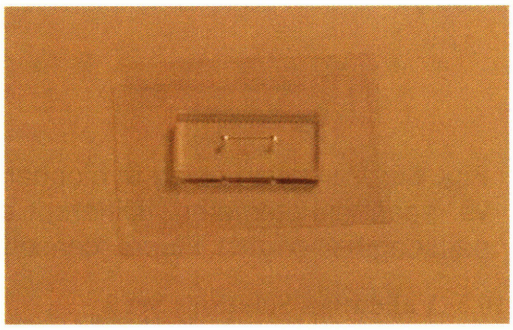

**Fig. 67:** PDMS/Quartz microchannel device.

The device was imaged on the stage and a syringe pump (Harvard Apparatus, Holliston MA) was used to flow solutions in and out. The channel was flushed with large volumes of purified water or PBS between readings. Our goals were to establish (1) that the optical density images match optical densities measured on a spectrophotometer, (2) that the native fluorescence images match fluorescence measurements made on a fluorimeter, and (3) to show that the quantum yield calculation is reasonable. Two sets of validation solutions were used:

### 10.2 Validation Solutions Set 1

Solutions of L-Tryptophan (Sigma-Aldrich, St. Louis MO) were prepared at approximate concentrations ranging from 0.5mg/ml to 4mg/ml in water and were characterized on a ND-1000 spectrophotometer (NanoDrop Technologies, Wilmington DE) and in a Fluorolog fluorometer (HoribaJobinYvon). Next, the solutions were imaged in the PDMS quartz flow channel with our deep UV microscope in 280 nm transmission and native fluorescence. Background images were obtained of the same channel filled with water. The mean optical density/fluorescence values were determined in each case for a 200 pixel square towards the center of the channel. The results are shown in **Fig. 68**. Both the native fluorescence and optical density values match well.

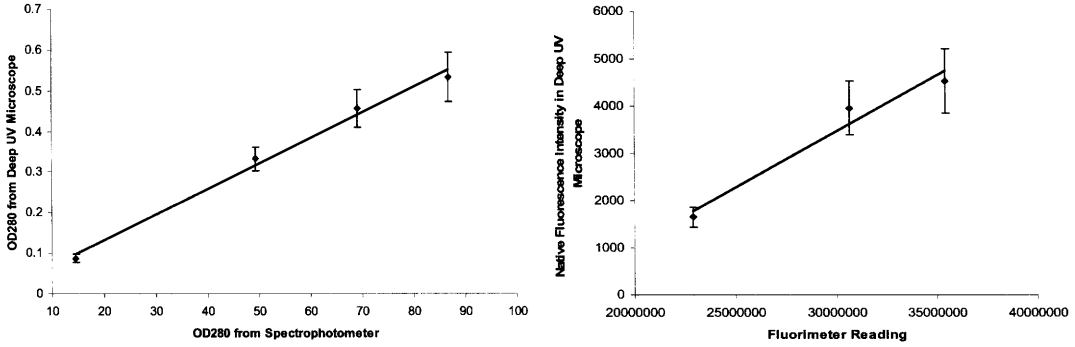


**Fig. 68:** Validation using tryptophan solutions. (**left**) OD280 for microscope vs. spectrophotometer. Different absolute values are a result of different pathlengths. (**right**) Fluorescence for microscope versus fluorimeter.

### 10.3 Validation Solutions Set 2

A solution of Bovine Serum Albumin (BSA) (Sigma-Aldrich, St. Louis MO) was prepared in PBS at approximately 124 mg/ml, and a separate solution of adenosine

(Sigma-Aldrich, St. Louis MO) to simulate nucleic acid was prepared in PBS with a concentration of approximately 2.4 mg/ml. A series of mixtures were prepared with the following BSA:adenosine fractions by volume (4:0),(3:1),(2:2),(1:3). The optical densities of these solutions were characterized at 260 nm and 280 nm using a ND-1000 spectrophotometer (NanoDrop Technologies, Wilmington DE) and the native fluorescence was measured with 280 nm excitation in a fluorometer (HoribaJobinYvon). Next, the solutions were imaged in the PDMS quartz flow channel with our deep UV microscope in 260 nm transmission, 280 nm transmission, and native fluorescence. Background images were obtained of the same channel filled with PBS. The mean optical densities/fluorescence values were determined in each case for a 200 pixel square towards the center of the channel as well as the quantum yields. The results are shown in **Fig. 69**.

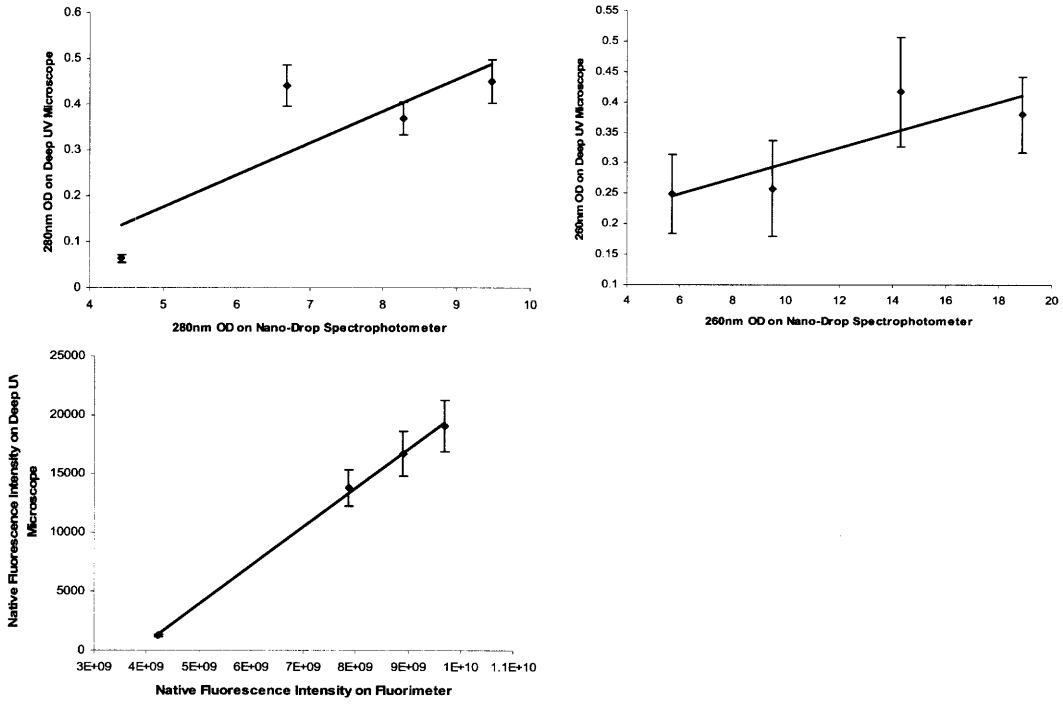


**Fig. 69:** Validation using BSA-adenosine mixtures. (**top left**) OD280 for microscope vs. spectrophotometer. Different absolute values are a result of different pathlengths. (**top right**) OD260 for microscope vs. spectrophotometer. Different absolute values are a result of different pathlengths. (**bottom left**) Fluorescence for microscope versus fluorimeter.

The native fluorescence matches the fluorimeter exceedingly well. The OD values are slightly noisier but follow the right trends. This noise is due in large part to the high absorbance of PDMS at deep UV wavelengths. The signal is significantly noisier at 260 nm since the transmission of PDMS is lower at that wavelength. The quantum yield of each solution was also calculated with the same equations used to determine quantum yield for the maps. This introduces some error because BSA and adenosine differ from the average protein and nucleic acid upon which the equations are based. The (1:3) solution yielded a negative value which was clearly an outlier due low values and high noise. However, the (4:0), (3:1), and (2:2) solutions had absolute quantum yields of 0.244±0.041, 0.265±0.056, and 0.218±0.058. These values compare favorably to published values for BSA of 0.15 and 0.21 [70].

## Chapter 11: Magnification

### 11.1 Determination of Pixel Size

For each configuration of the microscope, we determined pixel size using a fused silica Ronchi ruling (Edmund Optics, Barrington NJ) which was specified to have 600lp/mm. We acquired an image of this ruling in sharpest focus, then used ImageJ software to take a line plot, being careful to start and end the line on peaks (bright areas) and make it as closely perpendicular to the lines as possible. An example image and line plot are shown in **Fig. 70**. Pixel size was determined for the optical path both with and without the tube lens, and was re-determined after the emission filter wheel was added to the optical path, since this slightly altered the tube length. Using these methods, we determined that the pixel size with the tube lens in place was ~190nm, while the pixel size with the tube lens removed was ~92nm. With the tube lens removed and the motorized emission filter wheel, we determined the pixel size to be ~88nm on average, since it was 86.5nm at 280nm and 89.6nm at 320nm. This slight difference in magnification for different wavelengths is one potential error source and is discussed further in Chapter 12.

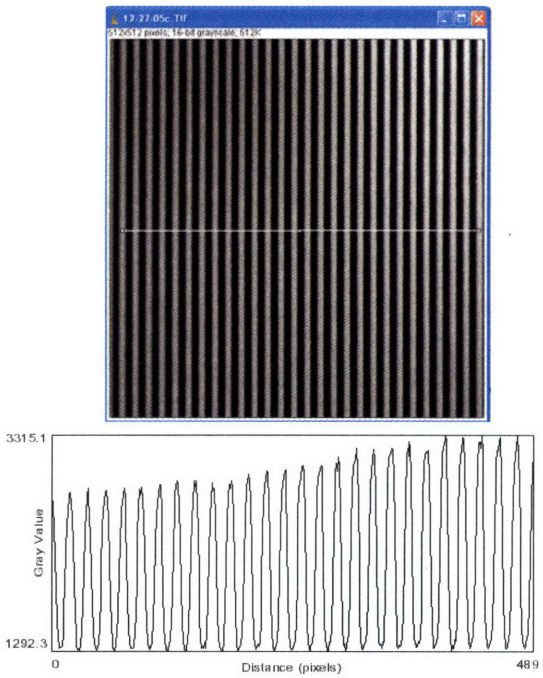


**Fig. 70:** (**top**) Image of fused silica Ronchi ruling with line, and (**bottom**) resulting line plot used to determine pixel size.

## 11.2 Determination of Spatial Resolution

The theoretical spatial resolution of the microscope should be determined by the standard formula:

$$D = \frac{\lambda}{2 \cdot NA}$$

Our 100X Zeiss Ultrafluar has NA=1.25, so for λ=280nm D = 112nm; for λ=340nm D = 136nm, and for λ=480nm D=192nm. However, to achieve full spatial resolution the pixel size must be ½ the spatial resolution because of the Nyquist limit. Our pixels are 92nm, which means that our minimum resolution is 184nm. To demonstrate this, we used a set of NIST traceable polystyrene microspheres with a mean diameter of 205.6±2.6 nm and a standard deviation of 6.3 nm (Polysciences). We prepared these beads on a quartz slide with a quartz coverslip. We then took one stack of images using a visible lamp and a 480nm excitation filter (Chroma D480/30X), with ~0.1μm z-step between each plane. We then took another stack of images using a 280nm LED with no excitation or emission filters, and a third stack using the visible lamp and a 480nm excitation filter again to make sure the beads had not moved. A series of planes surrounding the best focused plane were examined, as shown in **Fig. 71**. The results demonstrate the significant improvement in spatial resolution for deep UV images.

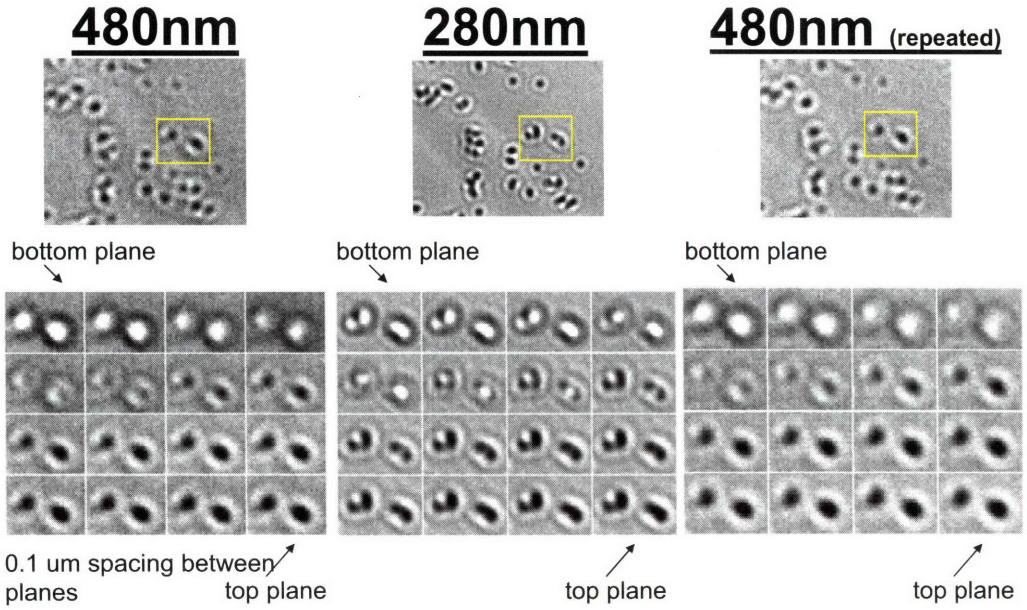


**Fig. 71:** A (**top row**) wider field and (**bottom row**) smaller field of 205nm beads at a variety of focal planes, for (**left column**) 480nm light. (**center column**) 280nm light, and (**right column**) 480nm light again.

## Chapter 12: Possible Artifacts/Error Sources

A number of possible error sources may affect the accuracy of our measurements. Here we report some of the most significant potential error sources.

### 12.1 Chromatic Aberration

One of the most serious potential error sources is chromatic aberration. In theory, the Zeiss Ultrafluar objective should be achromatic, but we are using it with a significantly longer tube length than the 160mm for which it was designed. Because our 260nm, 280nm, 320nm, and 340 nm images are all taken at the same focal plane, chromatic aberration would mean that not all of these images are precisely in focus, which could introduce errors into the very smallest details of our images. However, the differences are very slight and would not affect the larger picture (on the order of several pixels or more).

We do notice, qualitatively, that the 260nm images appear slightly "grainier" than the 280nm images. This does not appear to be a signal-to-noise issue since it is independent of the total intensity. Nor do we believe that the 260nm images are simply out of focus, since we have taken images at a variety of thinly spaced focal planes and still observed this phenomenon. It is possible that this effect is caused solely by increased scattering at this shorter wavelength, and that our scattering correction removes most of this effect. However, we must also be aware that our deep UV bandpass filter or the camera chip or coating itself could potentially respond differently to different wavelengths. Again, this would effect the smallest details (highest frequency features) of our images but we do not believe the effects would be significant on a scale of several pixels or more.

We have noticed a similar phenomenon with the native fluorescence images, which also appear to have less fine detail than the 280nm transmission images. At first we believed this to be a result of the fact that native fluorescence is measured over a wide range of wavelengths, so not all of it may be in focus in the same image. However, our images taken with a single bandpass emission filter did not appear to significantly affect this issue.

Finally, as discussed in the previous chapter the magnification appears to be at least weakly a function of wavelength. This could cause problems with alignment when calculating our scattering correction, but again we believe that this error would at the most only affect the very finest details of the images.

### 12.2 Lensing Effects

A more significant effect seems to occur from refractive lensing at the cell edges. This concern was pointed out in the literature [20] and it is clearly visible in **Fig. 72** which shows a quantum yield (calculated with our old method using just 280nm light) which exhibits negative values around the cell – these negative values are caused by a negative OD, meaning that the transmission image is brighter than the blank field as a result of lensing effects. From this, we conclude that data from the very edges of cells must be treated with significantly more skepticism than data inside the cytoplasm. Future work could involve finding ways to characterize and correct for this lensing at the edges, as well any refractive lensing that may occur within the cell.

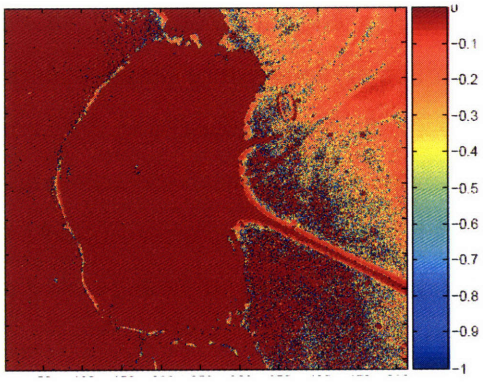


**Fig. 72:** Negative quantum yield at cell edges as a result of lensing effects.

### 12.3 Beer-Lambert Law Breakdown

Another potential concern is the well-known fact that the Beer-Lambert law (upon which our mass map calculations are based) breaks down at extremely high optical densities. But because of our short pathlength our maximum OD values were generally around 0.6 so the Beer-Lambert should hold, as our controls show.

### 12.4 Wavelength Shifts

Another possible source of error is the shift in wavelength of absorption and emission peaks of protein with changes in molecular environment. In particular, certain

conditions can shift protein emission to shorter wavelengths, making part of the emission outside the range of our longpass filter and thus artificially reducing our quantum yield.

### 12.5 Fixation Artifacts

As pointed out in the literature [19], the fixation process can significantly alter the optical properties of the cell. This may be a concern for our earlier work on fixed samples, but we believe that the effects are minimal and it is obviously not a problem now that we are focused on live-cell samples.

### 12.6 Vibration-Induced Blurring

While we have endeavored to make the scope as stable as possible, there may be some vibration. This could occur because the scope hangs off the edge of the optical table, and could also be exacerbated by the small cooling fan in the camera (although the manufacturer claims that this is not a problem. However, some of our longer-exposure images required 3 minutes or more, over which time it is possible that some blurring occurs. However, this would only affect very fine details.

### 12.7 Variations in LED Output Over Time

Our early calculations could be subject to error if the LED output varies over time, since the background image is taken at a different time but assumed to equal the excitation intensity. We do not believe this is a significant problem since the calculated OD for the blank areas surrounding cells are generally quite low. Moreover, in our more recent time lapse calculations we have introduced a normalization to account for this as described earlier.

### 12.8 Distributional Error

Distributional error refers to the fact that within one pixel there are many proteins, and so one aberrantly strong absorber could skew the average and make the pixel seem to have a much higher optical density than most of the proteins in it. This and other possible sources of error including glare are commonly associated with absorbance measurements in cytometry of stained samples [89].

# FUTURE DIRECTIONS

## Chapter 13: Near-term Scope Improvements

### 13.1 Infinity Correction

According to our Zeiss sales rep, Zeiss does manufacture a "160-to-ICS" adapter which screws into the back of 160mm tube length objectives and converts them to infinity-corrected. He also says that they used to manufacture a quartz version (part number 44-49-07). This item would be ideal because it would enable us to use our existing Ultrafluar objectives, but would eliminate the problems cause by placement of our filter wheel and would also help mitigate chromatic aberration. We have been unable to find or obtain this part. Doing this would reduce our magnification, but we could compensate for this by obtaining a Zeiss quartz 3x tv tube which our sales rep tells us they used to manufacture – similar in design to the current 4X tube (45-29-85) except with quartz lenses. We are also on the lookout for this part.

### 13.2 Dual Cameras

We are exploring a number of possible improvements to the current scope. One involves the simultaneous use of two cameras. This could be implemented in several advantageous configurations. Perhaps the most realistic involves simultaneously recording images above and below a cutoff wavelength. Technical Video Ltd. (Port Townsend, WA) manufactures a dual camera adapter (DCMSL-Z) for the Zeiss Axioskop for $1733. This cleverly designed adapter mounts in place of the standard phototube, accepts a standard Zeiss slider, and has two c-mounts. Using this device and our existing 310dcxxr beamsplitter, we could simultaneously collect 280nm transmitted light images and native fluorescence images on separate cameras. This would allow us to reduce the total exposure time necessary for quantum yield calculations, since we currently must expose the cell twice in order to acquire transmission and native fluorescence images. This arrangement would also enable us to acquire scattering correction images at 320nm and 340nm immediately after acquiring 260nm and 280nm images, without the time delay associated with changing the emission filter either manually or via a motorized

filter wheel. Moreover, on each of the two ports we could use a camera with optimum quantum efficiency for the wavelength range of interest. One drawback would be the need to very precisely align/register the two images prior to calculation. However, because the cameras would be fixed in place, this problem would most likely only need to be solved once. Also, the image quality of the transmission images may suffer as they are reflected off the dichroic before reaching the camera, since the dichroics are designed to reflect excitation light and thus may not do so at imaging-quality. Finally, this whole apparatus would function much more effectively if we had an infinity-corrected objective instead of fixed tube-length optics.

Another possible dual camera solution would be mechanically more difficult to implement, but warrants consideration. A native fluorescence image could be acquired using epifluorescence through the condenser, by mounting a dichroic and then a camera in the condenser pathway. This is mechanically impractical on our current scope, but may be feasible on future designs.

### 13.3 Improved Field Search

One key drawback of our current design is that user must search the field for a desired subject manually using the eyepieces and visible-wavelength transmission. Because these images are extremely low contrast, and because the only effective deep UV objective we have is a 100X, it is difficult and time consuming to identify an ideal cell to image, and even more difficult to return to the same cell again after moving the field of view. At the very least, it would help to use phase contrast or DIC to generate additional contrast during these visible light field searches. It is straightforward to rotate into place a lower power visible-wavelength phase contrast objective for field search, but implementing a matching condenser has proven more difficult. Because we are using an objective-style condenser we have not yet developed a reliable and feasible way to switch condensers. One option would be to install an objective-style rotating turret beneath, but this would also need x-y-z adjustment which would be infeasible with our present design. As an additional option, we removed the annulus ring from a standard condenser, and mounted this 25mm diameter optic underneath our current condenser. However, this approach was not effective because the position of the ring is important. Implementing

DIC may be more feasible since a polarizer could be placed anywhere in the condenser pathway.

Another challenge with our current field-search arrangement is that a cell that looks interesting under visible light may not look interesting under UV, and vice versa. On occasion, we have donned UV protective gear and adjusted the stage manually while observing the camera output. This approach is more effective for finding excellent cells to image in UV, but it may prove impractical for live-cell imaging because in order to provide near real-time display the cells must be exposed to UV at a very high frequency. Moreover, having the operator don protective gear is not a long term solution, so in order to effectively implement this approach we would need to motorize the stage. Implementing this would cost ~$13-17k, which would be a worthwhile investment if the scope is to be used by people other than its developers. It would also allow us to record and return to the same locations on a slide.

The acquisition of lower-magnification UV objectives would also aid in field search, as well as in toxicity studies on more than one cell at a time. We desperately want a Zeiss 32X Ultrafluar but lost the bidding on the only one we have seen available on eBay. Our 36X Ealing reflecting objective introduces too many artifacts and has too low of a numerical aperture to prove particularly useful in this regard. Nikon has generously loaned us a UV-Fluor 20X 0.75NA objective, but we are awaiting the transmission curves for this objective since it may only be designed for 340nm, as our tests on a similar 100X objective seem to indicate. We have also obtained an Olympus DPLAN APO 20X/0.80 UV objective but have not yet tested it. We are not particularly optimistic because it most likely is also designed for 340nm, and also it uses oil immersion media instead of glycerol so switching between the two objectives would be infeasible. We remain on the lookout for a 32X Ultrafluar.

### 13.4 3D Imaging

As discussed more extensively in the native fluorescence section, we believe that with more effective z-control (such as a piezo) and the ability to effectively measure a PSF, it would be possible to acquire 3D stacks of native fluorescence data and deconvolve them to create high resolution 3D images. We would also take 3D stacks of

transmitted light data. While deconvolving these is less common, a few companies (including SVI and AutoQuant) claim to either sell or plan to sell transmitted light deconvolution software and this is worth exploring as a potential way to obtain 3D mass maps.

### 13.5 Inverted Scope

We are also in the early stages of modifying a Nikon TE2000-U inverted microscope for use in the UV. We are working to design an adapter that will enable us to mount an RMS threaded condenser in the condenser mount, which is specified to have M48x0.75 pitch threads. We are also working to find or build an RMS-to-M25 (Nikon) thread adapter to mount a UV objective in the turret. In order to examine the inner workings of the scope, we removed this turret and the filter wheel beneath it. We were able to remove the tube-lens mount in order to create a clear path down to the port selector. This is where the design becomes difficult. A series of cube or cylinder beamsplitter/mirrors are used to select the port. For best image quality we would prefer not to use a mirror, so we need a straight path to a bottom port. While the similarly designed TE2000-E has a bottom port, Nikon service tells us the TE2000-U cannot be modified to include one. It may be possible to adapt it anyway since the rotating port selector has holes to allow light through to the eyepiece prism. Our current opinion is that a bottom port could be created, but only at the cost of sacrificing the use of the eyepieces. This would also present a mechanical challenged for stably mounting the scope over a camera. As an alternative, we could also install a UV-reflecting mirror in the "Aux" spot on this rotating port selector which is now empty, and we are working to obtain the dimensions and attachment mechanism that would allow us to do this (although the current cubes appear basically glued in, with a few posts to guide them). See **Fig. 73**.

One advantage of the Nikon is that it may be more amenable to dual-camera adaptation, since the epifluorescence excitation path is relatively exposed (compared to that on the Zeiss upright) and so we should be able to convert it into an imaging path with a camera port. Another advantage of the Nikon is that the current rotating filter selector can be motorized (unlike the Zeiss filter sliders). This would cost $7.879k and would

require a hub controller (MEF55010) as well as the actual motorized cassette (MEV51100), a control pad (MEF55000) and a few accessories.

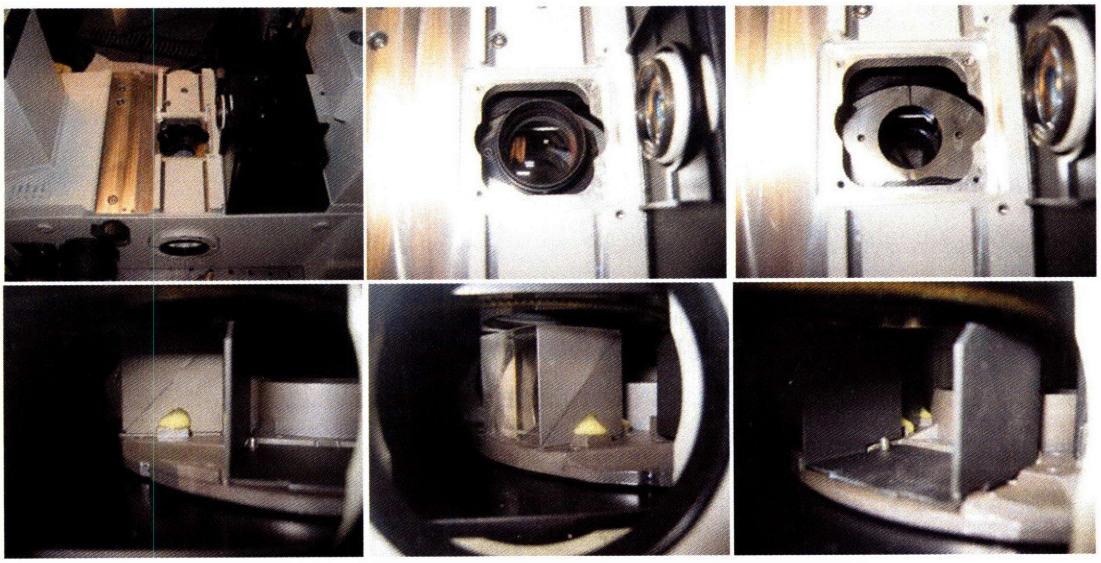

**Fig. 73:** The Nikon TE2000-U, (**top left**) shows the results of removing the stage, objective turret, and filter cube wheel. (**top center**) Shows the tube lens mount before and (**top right**) after removal of the tube lens. (**bottom left and center**) show the mounting of beamsplitter cubes in the path selector, and (**bottom right**) shows the empty "aux" position.

## Chapter 14: Collaborations Initiated/Other Applications Explored

### 14.1 Pharmaceutical Production Analysis

We found an unexpected application for deep UV imaging in the pharmaceutical production field. In chemical engineering, significant effort is devoted to studies of methods for mixing a tiny amount of drug with a much larger quantity of tablet material, in order to produce a tablet big enough for a person to handle and consume. When testing these tablet manufacturing methods, caffeine is typically used as the sample drug. Caffeine molecules happen to fluoresce when excited in the deep UV, so our microscope is well suited to image this. In order to attempt this, we set the scope back up for an epifluorescent imaging geometry which was necessary because the tablet is opaque. We then attempted to image the native fluorescence of a 5% caffeine tablet working in collaboration with Mridula Pore (MIT Cooney Lab, Chemical Engineering). While we were able to obtain some images with good resolution as shown in **Fig. 74**, we met significant challenges because the surface of the tablet was uneven and so it was difficult to focus on more than one spot at a time. The tablets we were using were hand-split. We concluded that in order to proceed we would need to find a way to cut them either very flat, or thin enough to do transmission imaging. One idea we considered was to cryo section the tablet the way tissue is traditionally prepared for electron microscopy, but we were not able to determine whether or not this was feasible. Nevertheless, these images prove that with proper sample preparation, deep UV excited native fluorescence could be a valuable tool for assessing pharmaceutical production procedures.

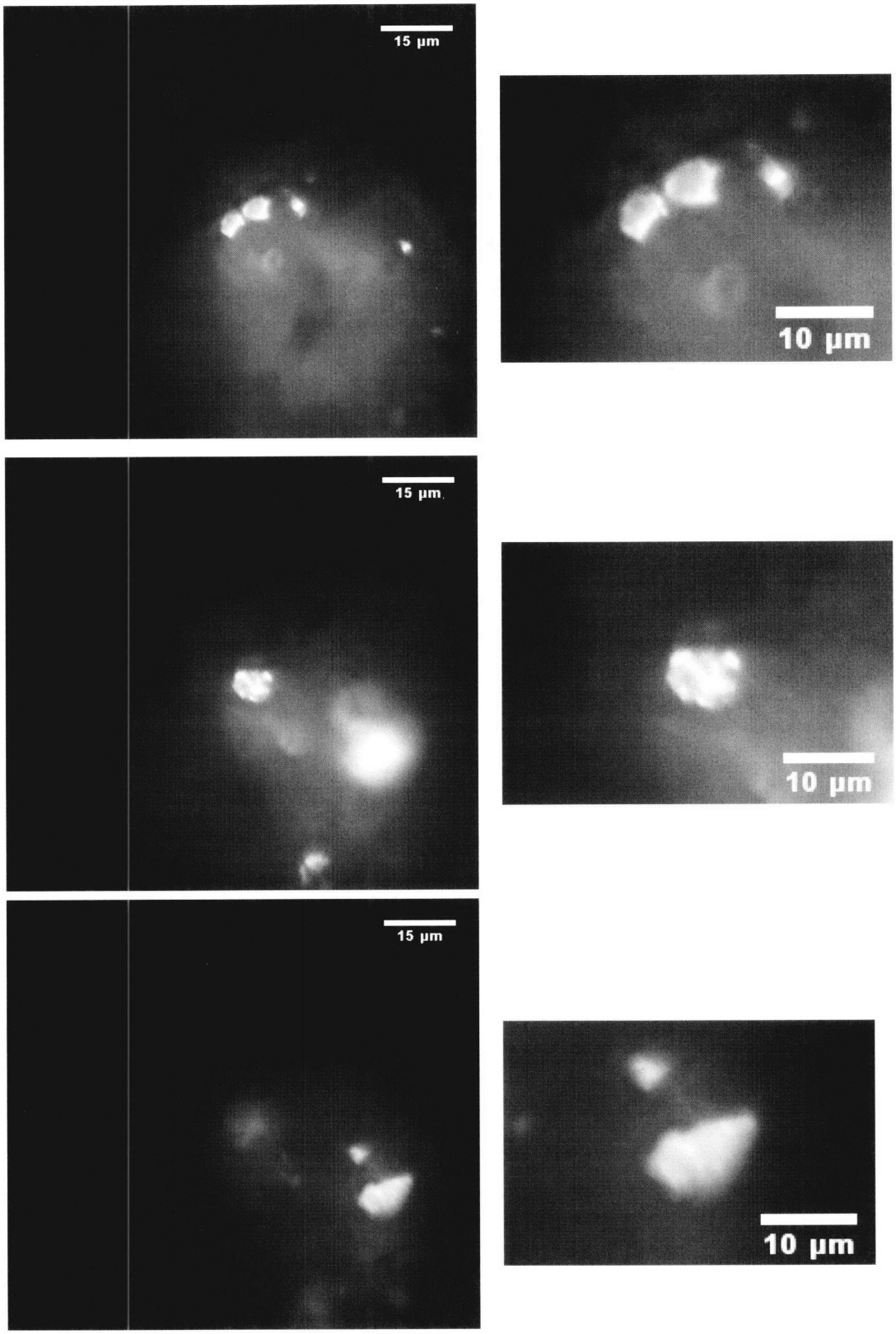


**Fig. 74:** (**left column)** Full images, and (**right column**) close-ups of a 5% caffeine tablet.

### 14.2 Protein Microarrays

Another potential collaboration we explored was the idea of imaging protein microarrays. The advantage here over traditional fluorescence methods is that we would be able to very precisely quantify the amount of protein bound, whereas fluorescence is less quantitative because proteins can sometimes be bound by multiple fluorophores. We decided to explore this in collaboration with Shaun Deignan (MIT Keating Lab, Biology). In order to explore whether or not proteins could be printed onto quartz slides instead of glass, Shaun first found a vendor that could functionalize quartz slides. We had this procedure done, and then tested the slides to make sure that they were still UV transparent. As shown in **Fig. 75**, the functionalization did not significantly impede the UV transmission of the slides. The next step is to print protein spots onto the slides – this is awaiting full testing of the protein printer. The spots are also fairly large, so to do this effectively we would need a low magnification objective and a well-calibrated motorized stage that would allow us to repeatably select known locations of spots on the stage. It is also possible that printed proteins could provide an effective way to calibrate the microscope, if we could control the thickness of the printed protein spot and the amount of protein deposited.

### 14.3 Yeast in Microchannels

Another potential collaboration was explored regarding deep UV imaging in a PDMS microfluidic system for imaging yeast that were exposed to time-varying stimuli (Ty Thomson, MIT Endy Lab, Biological Engineering). The chips were being designed in house but fabricated at the CalTech Soft Lithography Fab where they were pre-bonded to slides. However, we determined that we could bond them ourselves to quartz. We first attempted to do this using a plasma bonder which we were generously permitted to use by the Voldman Lab. However, when our collaborator tested these channels he found that they had collapsed in the bonding process, meaning that it was too harsh. He spoke

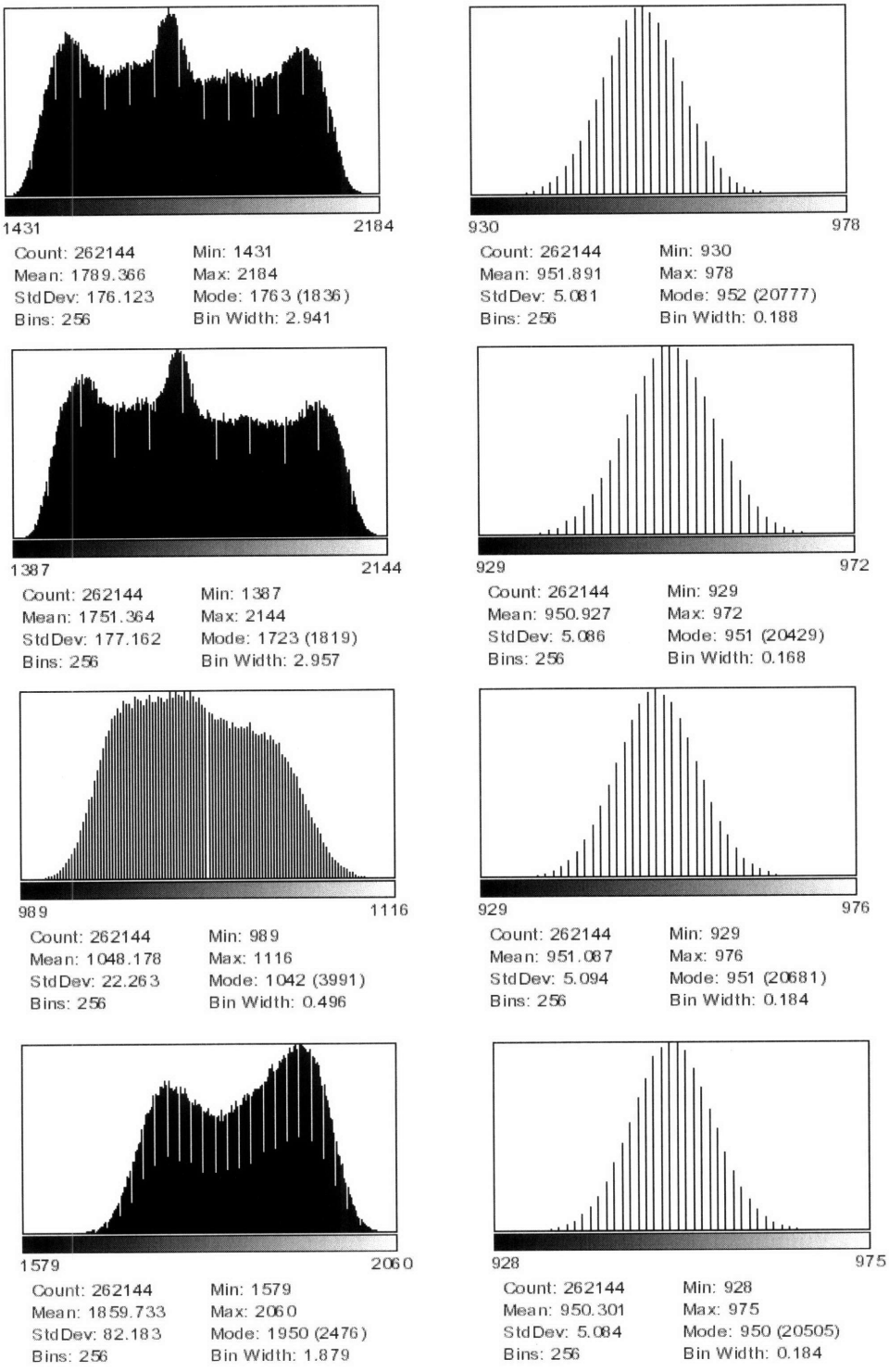


**Fig. 75:** Histograms of blank field (**left column**) transmission and (**right column**) autofluorescence measurements for (**top row**) functionalized quartz, (**second row**) blank quartz, (**third row**) glass slide, and (**bottom row**) no slide.

to the CalTech foundry and determined that they simply attached the PDMS chips to glass slides by bonding them "overnight" in an 80°C oven. We therefore tried bonding the PDMS chips to quartz slides in the oven for a variety of times, and found that 11 hours seemed to adhere the chips fine. In order to use an immersion lens such as our Ultrafluar 100X the quartz would have to be on top in our upright scope. Therefore a microscope slide would be too thick. We needed a quartz coverslip to adhere to the PDMS, but our largest coverslips were 1" by 1" which was too small to cover all the channels. We therefore investigated manufacturers of custom quartz coverslips and found two possibilities. We ended up purchasing these coverslips from Quartz Plus in Brookline NH. This fairly small outfit had 1 "by 3" coverslips left over from another run that they were able to sell us for around $60 each. Another option we found but did not utilize was CRAIC Technologies in Altadena CA, the same company that makes microspectrophotometers. They also were able to make quartz coverslips in 1" x 2" and 1" x 3" geometries for less than $50 apiece.

Future work could use the oven technique to bond these coverslips to the PDMS and then try imaging yeast exposed to time-varying stimuli. Mecahnical and logistical challenges still remain, however. We will need to make a mount that holds the PDMS chip inverted on the stage, yet allows the connector pins to protrude down and out of the chip. This may be mechanically challenging. In addition, in order to actually conduct the experiment our collaborator will have to bring all the valves and other pressure control equipment to our lab. Finally, the thickness of the PDMS chip may seriously impeded our UV transmission. We are trying to have the chip made as thinly as possible, but it needs to be at least several millimeters thick so that the foundry can handle it and so that the connector pins will stay in place.

### 14.4 *Vorticella*

Working with Danielle Cook France from our lab, we have attempted to image *Vorticella* with UV. Initial experiments found the *Vorticella* to be very sensitive to UV light. After even short exposures they would be contracting very rapidly and then eventually cease all motion and appear to be dead. Once dead, the *Vorticella* produced excellent transmission images and bright native fluorescence images. We subsequently

attempted to image extracted stalks under various conditions including extended (with EGTA) and contracted (with $Ca^{2+}$). These images were acquired using our old method of quantum yield calculations with just a 280nm image, but we do not believe this will be a problem because there is little nucleic acid in the stalk. The results are shown in **Fig. 76**. In a subsequent attempt we had difficulty imaging because the stalk was not sufficiently flat and our z-stacks did not line up, but we are planning experiments to overcome these issues. We ultimately want to determine the protein mass across the spasmoneme.

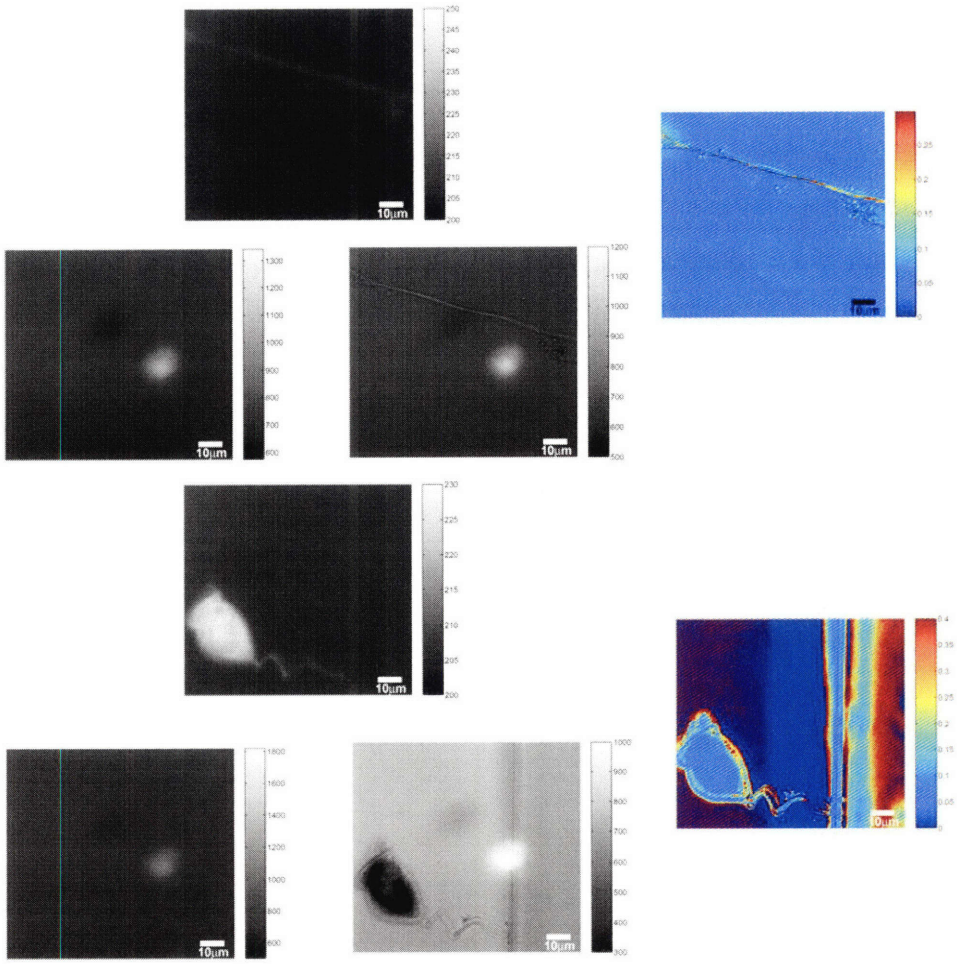


**Fig. 76:** (**top images**) Native fluorescence, blank field, and transmission images used to calculate quantum yield (color image) of a stalk extended with EGTA. (**bottom images**) Native fluorescence, blank field, and transmission images used to calculate quantum yield (color image) of a stalk contracted with $CaCl_2$.

## Chapter 15: Longer Term Applications/Areas of Study

### 15.1 Imaging Tryptophan Catabolism for Cancer/Immune System Evasion

Since literature suggests that tumor cells evade the immune system partly through tryptophan degradation [90], we would like to investigate this as a function of time and position, and see how early in the tumor development process we can detect these changes. Our scope is perfectly suited to study this problem. We could conduct controls by using known tryptophan degradation enzymes (such as Apotryptophanase from Escherichia coli – Sigma A6007) to examine the changes in absorbance and native fluorescence of solutions of tryptophan and whole proteins using the spectrophotometer and fluorimeter, then image these same solutions on our microscope in PDMS/quartz channels, then attempt to image the same phenomena in cells.

### 15.2 Deep UV Endoscope for Clinical Applications

If native fluorescence imaging does in fact prove to be a distinctive marker of cancer, we believe a deep UV endoscope could be possible. While there would be significant safety concerns about DNA damage, which would require long-term trials, this instrument could still prove useful in certain situations. For instance, it could allow the examination of a suspected tumor without the need to actually remove tissue for a biopsy. This could be important for brain tumors where it is damaging to remove even a small portion of tissue. While it is unlikely that transmission measurements could be made, it may be possible to extract some absorbance data from reflected light.

### 15.3 Live-Cell Quantum Yield

Although we now have the ability to switch emission filters using a motorized filter wheel (albeit at reduced image quality), implementing live-cell quantum yield measurement has thus far proved elusive, mostly because of the low signal-to-noise ratio which necessitates very long exposure times – on the order of 10 seconds – in order to get reasonable image quality. The signal is extremely weak to begin with, and significant noise is generated by the media necessary to keep cells alive, which contains some tryptophan and also proteins from fetal bovine serum. We also believe these components

in media may have higher quantum yield since they are not compact and thus experience less quenching. This is difficult because a weak signal alone can be compensated for electronically. However, even using the high gain electron-multiplying feature of our EMCCD camera has not led to a significant improvement in image quality – mostly because of this additional noise. We have tried replacing the media with PBS but cells react quickly to this less ideal environment. A few additional alternatives include the dual-camera acquisition discussed above, and also obtaining a camera with higher quantum yield than our 35% in the region between 300nm and 350nm.

Another more practical problem is that with our current camera control software and triggering setup, all images in a series must be taken with the same exposure time, which means that we cannot set up an automated time-lapse acquisition in which we acquire a long-exposure native fluorescence image followed by a short exposure transmission image. There may be a way to solve this by using independently generated TTL pulses of different lengths to control the camera exposure, or else we may need to write LabView or MATLAB code to control the camera.

### 15.4 GFP/UV Imaging

As described above, we incorporated a visible wavelength fluorescence capability into the microscope in order to conduct the experiments with live/dead kit staining. However, this capability is more generally useful and may enable a number of interesting experiments. Using the input automation techniques that we developed for the live cell 260/280 imaging, we could automate the process of switching between visible mercury lamp illumination (filtered with the 480nm bandpass filter for instance) and deep UV LED illumination. With our newly implemented automated emission filter selection, we will be able to take time lapse images of GFP or other exogenous visible fluorophores, superimposed with deep UV images. It is possible that the GFP may introduce some error into our UV images by absorbing at these wavelengths, but we believe the effect will be minimal. This would allow us to conduct very powerful studies by combining the specificity of labeling with the general structural information of protein and nucleic acid mass maps. For instance, we could fluorescently label histones, and then determine

whether or not the histones are present in the protein structures that we believe to be non-histone protein scaffolds.

### 15.5 Phototoxicity Studies

Our experiments raise many questions about UV response and toxicity. For instance, we have hypothesized that the interval between frames is important, and that the same total exposure of UV will have different effects depending on whether it is delivered all at once, or with intervals in between. We have also observed experimentally that different cell types have very different responses to UV radiation. While the IC-21s show dramatic necrosis after just a few hours, HT-1080s seem significantly more resistant to even longer exposures to UV. In order to investigate these effects, it would be ideal to have a more sensitive way to gauge cell damage, instead of the gross morphological changes associated with necrosis. One such approach could involve looking at genes that are upregulated in response to UV irradiation. We could start with *E. coli* in which many of theses genes are known [91]. Using GFP reporter constructs and the hardware changes discussed in the previous section, we could acquire time-lapse images of the upregulation of these genes, interleaved with time-lapse UV transmission images.

There are a number of other mechanisms that are used to quantify UV-induced damage biochemically. A method of counting the number of chromatin condensed cells to determine an apoptotic index is described in [67], along with analysis using flow cytometry, a DNA ladder assay, and a colony formation assay. However, most of these techniques rely on exposing a large number of cells and getting quantitative information by analyzing a large number of cells. It may be possible to measure chromatin condensation on a single cell, but in the Aoki paper it was measured as a binary measurement on each cell (condensed or not) and thus is no more sensitive than our current methods. The flow cytometry requires many cells, and the DNA ladder assay requires biochemical decomposition which is difficult to do on a single cell. The colony formation assay may be applicable if we could see a cell divide and then wait long enough to see it again. We have attempted one such experiment for over 48 hours using the 4 wavelength imaging procedure but did not see the cell divide again. This could be

due to many reasons including changes in temperature or $CO_2$ balance. Future work should investigate this further. But the reporting of UV-damage response genes seems to be the most elegant prospect for quantitative measurement of UV damage.

We have also investigated cell types that may be specifically resistant to UV. Reference [92] describes a set of mouse lymphoblast cells in which one type (LY-S) is resistant to UV radiation and another (LY-R) is sensitive to UV. We have also explored using antioxidants or other chemicals to reduce the UV damage, such as vitamin C or trolox. Another excellent suggestion, from Prof. Bevin Engelward, was to express a direct reversal photolyase, since these enzymes are not part of any pathways other than those related to photodamage repair, so overexpressing these enzymes would not interfere with any other pathways.

### 15.6 High Throughput Deep UV Imaging

While most of the imaging described here has been on single cells, there are many experiments where it would be ideal to examine large numbers of cells in order to obtain statistically relevant data. In particular, phototoxicity studies would benefit from such high throughput. Our lab currently performs high throughput imaging on living cells in multiwell plates using a Cellomics KineticScan system. In order to implement high throughput deep UV imaging, we would need a lower power objective than our 100X, and ideally one that does not require immersion media. Next, we would need a motorized stage in order to reliably scan different wells and record which fields belong to which wells. Finally, we would need to obtain UV transparent multiwell plates. These are in fact available. BD Falcon makes 96-well and 384-well UV-transparent microplates (353261 and 353262) from a resin which has very high transmission at wavelengths as short as ~240 nm. Corning also makes polymer-based 96-well and 384-well UV-microplates (3635 and 3675) with better than 60% transmission as low as 220nm. Hellma also makes 96-well and 384-well quartz microplates which have even higher transmission at even shorter wavelengths, but are significantly more expensive than the resin/polymer alternatives.

### 15.7 Live Cell Circular Dichroism Imaging

As discussed more extensively in the chapter on polarization modulation, we are working towards the ability to image living cells with circular dichroism at 222nm, in order to assess the alpha-helix and beta-sheet content of protein as a function of space and time.

### 15.8 Alzheimer's Studies

Circular dichroism spectroscopy has also been used to study the beta-peptide associated with Alzheimer's [43]. The ability to image deep UV circular dichroism could prove useful for examining frozen brain sections from the cadaver of an Alzheimer's patient, in order to better understand the spatial organization of this protein.

### 15.9 Native Fluorescence Imaging of Viral Infection

An exciting recent spectroscopy study [93] found that bacteriophages have a different emission peak for their native fluorescent than do their host cells, and utilized this difference to observe the process of virus infection of host cells by changes in native fluorescence. With the right filters, our microscope is well suited to make these same observations as a function of position, providing a noninvasive way to identify and study viral infection. Viruses may also show up clearly in our protein and nucleic acid mass maps, as suggested by Matt Lang, because they have such a high concentration of DNA and relatively little protein. We believe that this represents a huge area of potential research with many medically relevant applications and deserves significant further attention.

## REFERENCES


1. Belmont, A. Dynamics of chromatin, proteins, and bodies within the cell nucleus. *Current Opinion in Cell Biology* **15**, 304-310 (2003).
2. Paulson, J. R. & Laemmli, U. K. The structure of histone-depleted metaphase chromosomes. *Cell* **12**, 817-828 (1977).
3. Personal communication with Danielle Cook France, Matsudaira Lab, MIT.
4. Watkins, S. in *Current Protocols in Molecular Biology* 14.6.1-14.6.13 (John Wiley & Sons., 2003).
5. Liu, H. S., Jan, M. S., Chou, C. K., Chen, P. H. & Ke, N. J. Is green fluorescent protein toxic to the living cells? *Biochemical and Biophysical Research Communications* **260**, 712-717 (1999).
6. Hanson, D. & Ziegler, S. Fusion of green fluorescent protein to the C-terminus of granulysin alters its intracellular localization in comparison to the native molecule. *Journal of Negative Results in BioMedicine* **3**, 2 (2004).
7. Yang, W. S. et al. C-terminal region of Bfl-1 induces cell death that accompanies caspase activation when fused with GFP. *Journal of Cellular Biochemistry* **94**, 1234-1247 (2005).
8. Aokage, T., Ohsawa, I. & Ohta, S. Green fluorescent protein causes mitochondria to aggregate in the presence of the Bcl-2 family proteins. *Biochemical and Biophysical Research Communications* **314**, 711-716 (2004).
9. Martinez-Serrano, A., Villa, A., Navarro, B., Rubio, F. J. & Bueno, C. Human neural progenitor cells: better blue than green? *Nature Medicine* **6**, 483-483 (2000).
10. Krestel, H. E., Mihaljevic, A. L. A., Hoffman, D. A. & Schneider, A. Neuronal co-expression of EGFP and beta-galactosidase in mice causes neuropathology and premature death. *Neurobiology of Disease* **17**, 310-318 (2004).
11. Steinbauer, M. et al. GFP-transfected tumor cells are useful in examining early metastasis in vivo, but immune reaction precludes long-term tumor development studies in immunocompetent mice. *Clin Exp Metastasis* **20**, 135-41 (2003).
12. Personal communication with Winston Timp, Matsudaira Lab, MIT.
13. Inoue, S. & Spring, K. R. *Video Microscopy The Fundamentals* (Plenum Press, New York, 1997).
14. Evans, J. G., Correia, I., Krasavina, O., Watson, N. & Matsudaira, P. Macrophage podosomes assemble at the leading lamella by growth and fragmentation. *J. Cell Biol.* **161**, 697-705 (2003).
15. Shribak, M. & Inoue, S. Orientation-independent differential interference contrast microscopy. *Appl Opt* **45**, 460-9 (2006).
16. Van Munster, E. B., Winter, E. K. & Aten, J. A. Measurement-based evaluation of optical pathlength distributions reconstructed from simulated differential interference contrast images. *J Microsc* **191**, 170-176 (1998).
17. Gallagher, S. R. in *Current Protocols in Molecular Biology* A.3D.1-A.3D.12 (John Wiley & Sons, 2004).
18. Alupoaei, C. E. & Garcia-Rubio, L. H. Growth behavior of microorganisms using UV-Vis spectroscopy: Escherichia coli. *Biotechnol Bioeng* **86**, 163-7 (2004).
19. Walker, P. M. B. in *Physical Techniques in Biological Research* (ed. Oster, G.) 401-487 (Academic Press, New York, 1956).

20. Caspersson, T. O. *Cell Growth and Cell Function* (W.W. Norton & Co., New York, 1950).
21. Lang-Pauluzzi, I. The behaviour of the plasma membrane during plasmolysis: a study by UV microscopy. *Journal of Microscopy-Oxford* **198**, 188-198 (2000).
22. Lichtscheidl, I. K. & Url, W. G. Investigation of the Protoplasm of Allium-Cepa Inner Epidermal-Cells Using Ultraviolet Microscopy. *European Journal of Cell Biology* **43**, 93-97 (1987).
23. Lunde, C. S. et al. UV microscopy at 280 nm is effective in screening for the growth of protein microcrystals. *Journal of Applied Crystallography* **38**, 1031-1034 (2005).
24. Hatfield, J. M., Schulze, L. & Ernst, D. Measurement of the ultraviolet absorption in specific parts of both living and fixed mammalian cells, using a specially designed microspectrophotometer. *Exp Cell Res* **59**, 484-6 (1970).
25. Heimann, P. A. & Urstadt, R. Deep Ultraviolet Microscope. *Applied Optics* **29**, 495-501 (1990).
26. Davies, H. G. Ultra-violet microspectrography of living tissue culture cells. Part I. Radiation measurements. *Discussions of the Faraday Society* **9**, 442-449 (1950).
27. Walker, P. M. B., Davies, H.G. Ultra-violet microspectrography of living tissue culture cells. Part II. Microspectrographic studies of living cells and ultraviolet-irradiated chick fibroblasts. *Discussions of the Faraday Society* **9**, 461-470 (1950).
28. Williams, G. Z. & Neuhauser, R. G. Instrumentation for time lapse ultraviolet television microscopy. *Ann N Y Acad Sci* **97**, 358-63 (1962).
29. Freed, J. J. & Engle, J. L. Development of the vibrating-mirror flying spot microscope for ultraviolet spectrophotometry. *Ann N Y Acad Sci* **97**, 412-30 (1962).
30. Engle, J. L. & Freed, J. J. Double-beam vibrating mirror flying spot scanning-integrating microspectrophotometer. *Rev Sci Instrum* **39**, 307-12 (1968).
31. Yuan, T., Weljie, A. M. & Vogel, H. J. Tryptophan fluorescence quenching by methionine and selenomethionine residues of calmodulin: Orientation of peptide and protein binding. *Biochemistry* **37**, 3187-3195 (1998).
32. Ruan, K., Tian, S., Lange, R. & Balny, C. Pressure effects on tryptophan and its derivatives. *Biochem Biophys Res Commun* **269**, 681-6 (2000).
33. Palmer, G. M., Keely, P. J., Breslin, T. M. & Ramanujam, N. Autofluorescence spectroscopy of normal and malignant human breast cell lines. *Photochemistry and Photobiology* **78**, 462-469 (2003).
34. Lillard, S. J. & Yeung, E. S. Temporal and spatial monitoring of exocytosis with native fluorescence imaging microscopy. *Journal of Neuroscience Methods* **75**, 103-109 (1997).
35. Tan, W. H., Parpura, V., Haydon, P. G. & Yeung, E. S. Neurotransmitter Imaging in Living Cells Based on Native Fluorescence Detection. *Analytical Chemistry* **67**, 2575-2579 (1995).
36. Judge, R. A., Swift, K. & Gonzalez, C. An ultraviolet fluorescence-based method for identifying and distinguishing protein crystals. *Acta Crystallographica Section D-Biological Crystallography* **61**, 60-66 (2005).
37. James, J., Tanke, H.J. *Biomedical Light Microscopy* (Kluwer Academic Publishers, Boston, 1991).

38. Vergani, L., Canneva, F., Ghisellini, P. & Nicolini, C. Expression, Purification, and Structural Characterization of Human Histone H4. *Protein Expression and Purification* **24**, 420-428 (2002).
39. Wang, X., Moore, S. C., Laszckzak, M. & Ausio, J. Acetylation Increases the alpha -Helical Content of the Histone Tails of the Nucleosome. *J. Biol. Chem.* **275**, 35013-35020 (2000).
40. Mahadev, K. & Vemuri, M. C. Effect of ethanol on chromatin and nonhistone nuclear proteins in rat brain. *Neurochemical Research* **23**, 1179-1184 (1998).
41. Sprecher, C. A. & Johnson, W. C. Circular-Dichroism of Nucleic-Acid Monomers. *Biopolymers* **16**, 2243-2264 (1977).
42. Saxena, V. P. & Wetlaufer, D. B. A New Basis for Interpreting the Circular Dichroic Spectra of Proteins. *Proceedings of the National Academy of Sciences of the United States of America* **68**, 969-972 (1971).
43. Huang, T. H. J. et al. Structural studies of soluble oligomers of the alzheimer [beta]-amyloid peptide. *Journal of Molecular Biology* **297**, 73-87 (2000).
44. Garnett, A. P. & Viles, J. H. Copper binding to the octarepeats of the prion protein - Affinity, specificity, folding, and cooperativity: Insights from circular dichroism. *Journal of Biological Chemistry* **278**, 6795-6802 (2003).
45. Livolant, F. & Maestre, M. F. Circular-Dichroism Microscopy of Compact Forms of DNA and Chromatin Invivo and Invitro - Cholesteric Liquid-Crystalline Phases of DNA and Single Dinoflagellate Nuclei. *Biochemistry* **27**, 3056-3068 (1988).
46. Mickols, W. & Maestre, M. F. Scanning differential polarization microscope: Its use to image linear and circular differential scattering. *Review of Scientific Instruments* **59**, 867-872 (1988).
47. Claborn, K., Puklin-Faucher, E., Kurimoto, M., Kaminsky, W. & Kahr, B. Circular dichroism imaging microscopy: Application to enantiomorphous twinning in biaxial crystals of 1,8-dihydroxyanthraquinone. *Journal of the American Chemical Society* **125**, 14825-14831 (2003).
48. Mackey, J. R., Salari, E. & Tin, P. Optical material stress measurement using two orthogonally polarized sinusoidally intensity-modulated semiconductor lasers. *Measurement Science & Technology* **13**, 179-185 (2002).
49. Lobenstine, E. W., Schaefer, W. C. & Turner, D. H. Fluorescence Detected Circular-Dichroism of Proteins with Single Fluorescent Tryptophans. *Journal of the American Chemical Society* **103**, 4936-4940 (1981).
50. http://www.darpa.mil/mto/suvos/
51. Whitaker, T. SUVOS pushes UV LEDs and lasers to shorter wavelengths. *Compund Semiconductor Magazine* (2004).
52. Adivarahan, V. et al. 250 nm AlGaN light-emitting diodes. *Applied Physics Letters* **85**, 2175-2177 (2004).
53. Zhang, J. P. et al. Milliwatt power deep ultraviolet light-emitting diodes over sapphire with emission at 278 nm. *Applied Physics Letters* **81**, 4910-4912 (2002).
54. Chitnis, A. et al. Milliwatt power AlGaN quantum well deep ultraviolet light emitting diodes. *Physica Status Solidi a-Applied Research* **200**, 99-101 (2003).
55. Herman, P., Maliwal, B. P., Lin, H. J. & Lakowicz, J. R. Frequency-domain fluorescence microscopy with the LED as a light source. *J Microsc* **203**, 176-81 (2001).

56. Jaksic, Z., Milan Maksimovic & Sarajlic, M. Silver-silica transparent metal structures as bandpass filters for the ultraviolet range. *Journal of Optics A: Pure and Applied Optics* **7**, 51 (2005).
57. Kochergin, V., Ofer Sneh, Mahavir Sanghavi, Philip R. Swinehart. in *NASA Earth-Sun System Technology Conference* (University of Maryland Inn and Conference Center in College Park, 2005).
58. Personal communication with Joe Yeager, Lake Shore Cryotronics, Inc. 10/3/05.
59. JASCO, C. *CD-ORD Measurement Manual* (Jasco Corporation, Tokyo, Japan, 1995).
60. Johnson, W. C., Jr. Circular dichroism and its empirical application to biopolymers. *Methods Biochem Anal* **31**, 61-163 (1985).
61. Johnson, W. C. J. in *Circular Dichroism and the Conformational Analysis of Biomolecules* (ed. Fasman, G. D.) (Plenum Press, New York, 1996).
62. Cassim, J. Y. & Yang, J. T. A computerized calibration of the circular dichrometer. *Biochemistry* **8**, 1947-51 (1969).
63. Geng, L., L.B. McGown. Correction for Unequal Intensities of Left and Right Circularly Polarized Light in Steady-State and Lifetime-Resolved Fluorescence-Detected Circular Dichroism. *Applied Spectroscopy* **48**, 167-175 (1994).
64. Venyaminov, S. Y., J.T. Yang. in *Circular Dichroism and the Conformational Analysis of Biomolecules* (ed. Fasman, G. D.) 69-107 (Plenum Press, New York, 1996).
65. Personal communication from Dr. Yuri Bilenko, Sensor Electronic Technology Inc., 12/1/05.
66. Zeskind, B., C. Jordan, W. Timp. D. Ehrlich, P. Matsudaira. Mapping Nucleic Acid and Protein Mass in Live Cells by Deep Ultraviolet Microscopy. *(submitted)* (2006).
67. Aoki, M., Furusawa, Y., Higashi, S. & Watanabe, M. Action spectra of apoptosis induction and reproductive cell death in L5178Y cells in the UV-B region. *Photochem Photobiol Sci* **3**, 268-72 (2004).
68. Freshney, R. I. *Culture of Animal Cells A Manual of Basic Technique* (Alan R. Liss, Inc., New York, 1987).
69. Freifelder, D. *Physical Biochemistry* (W.H. Freeman, New York, 1982).
70. Fasman, G. D. (ed.) *Practical Handbook of Biochemistry and Molecular Biology* (CRC Press, Boca Raton, FL, 1990).
71. Lodish, H., Matsudaira, P.T., Kaiser, C.A., Krieger, M., Scott, M.P., Zipursky, S.L., Darnell, J. *Molecular Cell Biology* (W.H. Freeman and Co., New York, 2004).
72. Voet, D., Voet, J.G. *Biochemistry* (John Wiley & Sons, New York, 1995).
73. Berg, J. M., J.L. Tymoczko, L. Stryer. *Biochemistry* (W.H. Freeman, New York, 2002).
74. Butler, J. M. *Forensic DNA Typing* (Academic Press, San Diego, CA, 2001).
75. Alberts, B., D. Bray,J. Lewis,M. Raff,K. Roberts,J.D. Watson. *Molecular Biology of the Cell* (Garland Publishing, New York, 1994).
76. Weidemann, T. et al. Counting Nucleosomes in Living Cells with a Combination of Fluorescence Correlation Spectroscopy and Confocal Imaging. *Journal of Molecular Biology* **334**, 229-240 (2003).
77. Gualberto, A., Lowry, J., Santoro, I. M. & Walsh, K. Parameters That Influence the Extent of Site Occupancy by a Candidate Telomere End-binding Protein. *J. Biol. Chem.* **270**, 4509-4517 (1995).

78. Bauer, K. & Dethlefsen, L. Total cellular RNA content: correlation between flow cytometry and ultraviolet spectroscopy. *J. Histochem. Cytochem.* **28**, 493-498 (1980).
79. DiSanto, M. E. et al. Alteration in expression of myosin isoforms in detrusor smooth muscle following bladder outlet obstruction. *Am J Physiol Cell Physiol* **285**, C1397-1410 (2003).
80. Duck-Chong, C., Pollak, J. K. & North, R. J. THE RELATION BETWEEN THE INTRACELLULAR RIBONUCLEIC ACID DISTRIBUTION AND AMINO ACID INCORPORATION IN THE LIVER OF THE DEVELOPING CHICK EMBRYO. *J. Cell Biol.* **20**, 25-35 (1964).
81. Handwerger, K. E., Cordero, J. A. & Gall, J. G. Cajal Bodies, Nucleoli, and Speckles in the Xenopus Oocyte Nucleus Have a Low-Density, Sponge-like Structure. *Mol. Biol. Cell* **16**, 202-211 (2005).
82. Ellis, R. J. Macromolecular crowding: an important but neglected aspect of the intracellular environment. *Current Opinion in Structural Biology* **11**, 114-119 (2001).
83. Hudson, D. F., Vagnarelli, P., Gassmann, R. & Earnshaw, W. C. Condensin Is Required for Nonhistone Protein Assembly and Structural Integrity of Vertebrate Mitotic Chromosomes. *Developmental Cell* **5**, 323-336 (2003).
84. Belmont, A. S. Mitotic chromosome scaffold structure: New approaches to an old controversy 10.1073/pnas.262672799. *PNAS* **99**, 15855-15857 (2002).
85. Winder, A. F. & Gent, W. L. Correction of light-scattering errors in spectrophotometric protein determinations. *Biopolymers* **10**, 1243-51 (1971).
86. Perelman, L. T., V. Backman, M. Wallace, G. Zonios, R. Manoharan, A. Nusrat, S. Shields, M. Seiler, C. Lima, T Hamano, I. Itzkan, J. Van Dam, J.M. Crawford, M.S.Feld. Observation of Periodic Fine Structure in Reflectance from Biological Tissue: A New Technique for Measuring Nuclear Size Distribution. *Phys. Rev. Lett.* **80**, 627-630 (1998).
87. Sefkow, A., M. Bree, M.-A. Mycek. Method for Measuring Cellular Optical Absorption and Scattering Evaluated Using Dilute Cell Suspension Phantoms. *Applied Spectroscopy* **55**, 1495-1501 (2001).
88. Jacques, S. L. in *OSA Trends in Optics and Photonics on Advances in Optical Imaging and Photon Migration* (ed. Alfano, R. R., J.G. Fujimoto) 364-369 (Optical Society of America, Washington, DC, 1996).
89. Chieco, P., Jonker, A., Melchiorri, C., Vanni, G. & Van Noorden, C. J. A user's guide for avoiding errors in absorbance image cytometry: a review with original experimental observations. *Histochem J* **26**, 1-19 (1994).
90. Uyttenhove, C. et al. Evidence for a tumoral immune resistance mechanism based on tryptophan degradation by indoleamine 2,3-dioxygenase. *Nat Med* **9**, 1269-74 (2003).
91. Courcelle, J., Khodursky, A., Peter, B., Brown, P. O. & Hanawalt, P. C. Comparative Gene Expression Profiles Following UV Exposure in Wild-Type and SOS-Deficient Escherichia coli. *Genetics* **158**, 41-64 (2001).
92. Beer, J. Z. et al. Loss of tumorigenicity with simultaneous changes in radiosensitivity and photosensitivity during in vitro growth of L5178Y murine lymphoma cells. *Cancer Res* **43**, 4736-42 (1983).
93. Alimova, A. et al. Virus particles monitored by fluorescence spectroscopy: a potential detection assay for macromolecular assembly. *Photochem Photobiol* **80**, 41-6 (2004).

## APPENDIX

### Section 1: Photoacoustic work

Our earliest photoacoustic work aimed to use an existing Zeiss LSM510 laser scanning microscope as the excitation source, and detect vibrations in a sealed chamber made from a modified glass-bottomed Petri dish. However, we quickly learned that a more specialized chamber was needed to eliminate vibrations, and that we would need more control over the excitation light than the LSM would provide.

### A1.1 Photoacoustic Chamber

We next designed and had machined an aluminum photoacoustic chamber shown in **Fig. A1** which used a transparent window, had a carefully fitted hole for a microphone, and a panel on the bottom to insert and remove a sample. For excitation, we use an argon-ion laser modulated by a mechanical chopper (Stanford Research Systems, Sunnyvale CA). Modulated light excited a solid or liquid sample in the chamber. For most of our work we used activated charcoal as a strongly absorbing control substance. Photoacoustically induced vibrations are detected with a microphone (Knowles Acoustics, Itasca IL) and sent to a lock-in amplifier (Stanford Research Systems, Sunnyvale CA) to be amplified at the modulation frequency. Data from the lock-in amplifier is recorded on a PC and processed using MATLAB (Mathworks, Framingham MA). A block diagram of our system is shown in **Fig. A2**, and preliminary results in **Fig. A3**. As the figure illustrates, these results can be fitted well with the classic Rosencwaig-Gersho (R-G) theory of photoacoustics.

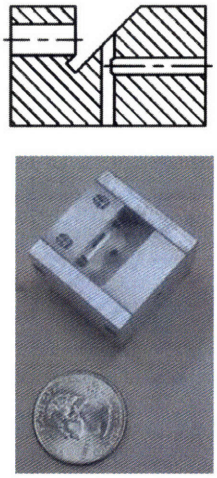

**Fig. A1:** Cross section (top left) and photo (bottom left) of the photoacoustic chamber designed by our group. A beam splitter plate is placed over the central channel, sending a reference beam of light out the channel on the left. The remaining light passes down the central channel and strikes the sample at the bottom of the chamber. The microphone is inserted in the channel on the right.

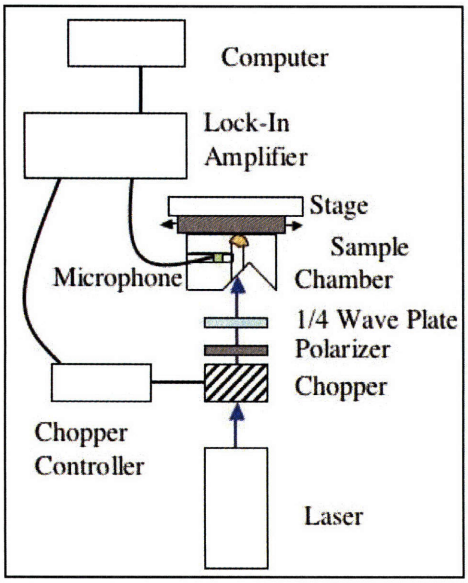


**Fig. A2:** Block diagram of our photoacoustic detector. Chopped laser light excites the sample in the chamber, creating vibrations that are detected by the microphone, amplified by the lock-in, and recorded on the computer. The magnitude of the signal is proportional to the absorption of the sample, according to the Rosencwaig-Gersho theory.

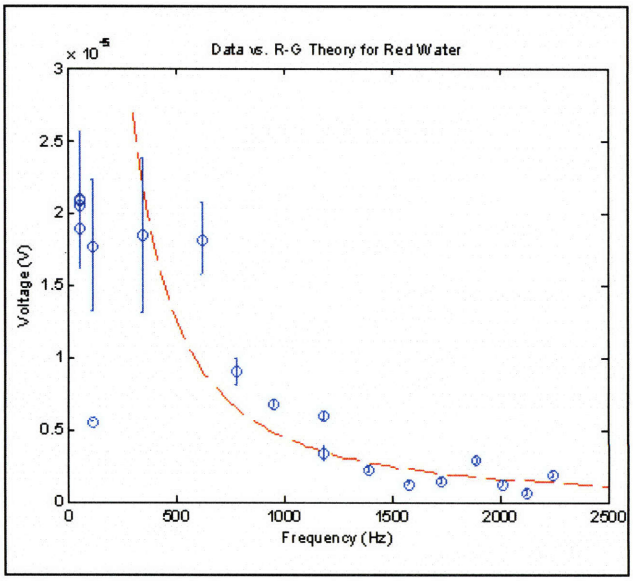


**Fig. A3:** Data measured with our photoacoustic detector, fitted with predictions from the Rosencwaig-Gersho theory. The sample was water with red dye. The circles, with error bars, represent the average and standard deviations of our measurements at a given frequency. The measured voltage is related to pressure by our microphone's conversion factor, and this pressure is related to the absorption of the sample. The dashed line is the R-G theory. We have used an arbitrary constant to scale the theory to the correct magnitude. Voltages are on the order of 20 μV and frequencies range from 0 – 2.5 kHz.

### A1.2 Photoacoustic Microscope

We have subsequently integrated our photoacoustic chamber with a SM-LUX HL upright microscope (Leitz, Germany) and directed our laser into the light port, as shown in **Fig. A4**. We have used onion cells as a simple biological sample, staining some with methylene blue chloride, and placing them on a standard microscope slide without a coverslip. This slide is attached to the bottom of our chamber, and a 150W quartz halogen light (Cuda Products, Jacksonville FL) source placed underneath. A Fire-i400 digital camera (Unibrain, San Ramon CA) allows us to record a transmission image of the cells, and to visualize the laser spot on the cells, while simultaneously recording a photoacoustic signal. The results are shown in **Fig. A5**. A very strong photoacoustic

signal is produced when the laser is at certain points, and not at others. While this sometimes corresponds with the presence of dark spots in the visible image, this is not always the case, suggesting that we are obtaining some new information. During the course of our research we will improve the quality of the optics and signal. We have also recently included a MicroMax Series 670 galvanometer (Cambridge Technology, Cambridge MA) which allows us to scan the laser beam along one axis controllably and reproducibly by using the output from a PCI-6704 DC analog output card (National Instruments, Austin TX) controlled by LabView software. We are in the process of adding a second galvanometer for full X-Y control.

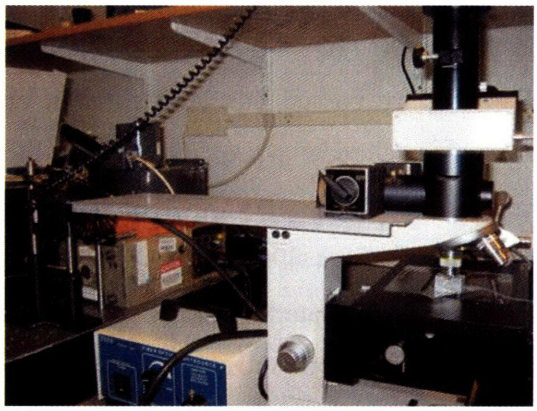

**Fig. A4:** Initial laser scanning photoacoustic microscope apparatus.

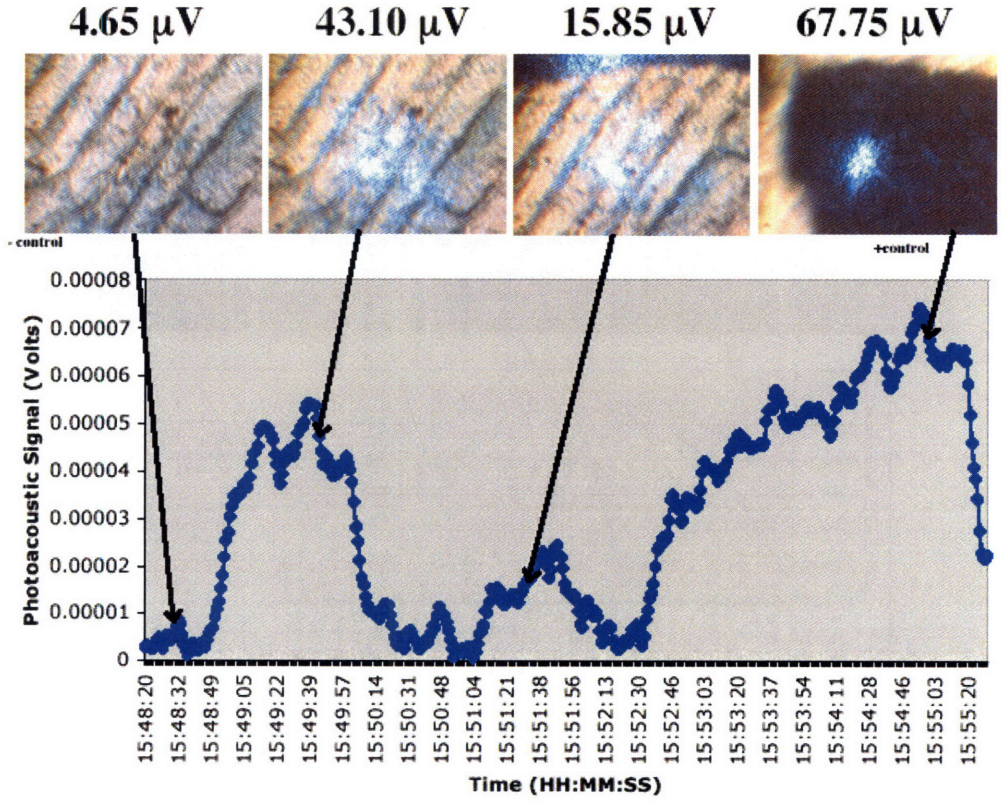


**Fig. A5:** Data from laser scanning photoacoustic microscope.

### A1.3 Dual Wavlength Photoacoustic Microscope

Building on the microscope described in the previous section, we added a second laser, a HeNe (JDS Uniphase) operating at 633nm. Through careful alignment shown in **Fig. A6**, we passed this laser through one ring of the chopper wheel and the argon-ion laser through the other, so that the HeNe was modulated at 490Hz and the argon-ion laser was modulated at 408Hz. We then combined these two beams so they were both incident on the sample. As shown in **Fig. A7**, by selecting which frequency was used to synchronize the lock-in, we could measure the photoacoustic absorption of the sample at the wavelength modulated at that frequency, independent of whether or not the other laser was on. This shows that, with two lock-in amplifiers, we could simultaneously measure absorbance at two wavelengths.

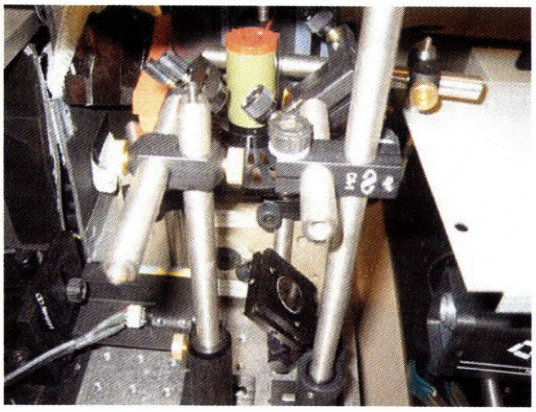

**Fig. A6:** Appartus for modulating two lasers at different frequencies and combining the resulting beam.

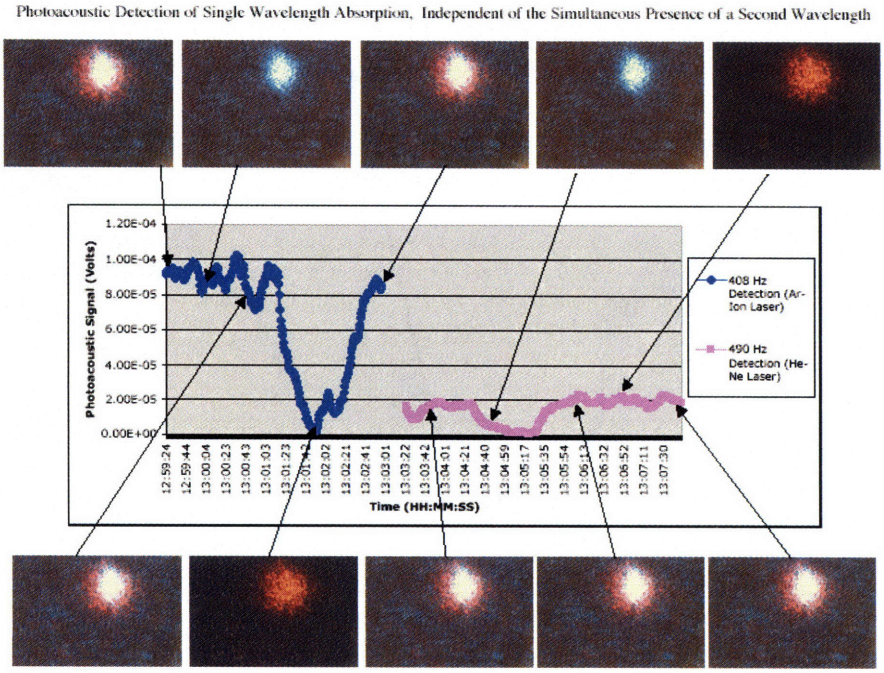


**Fig. A7:** Data from dual-wavelength photoacoustic microscope.

### A1.4 Photoacoustic Measurement in Microfabricated Channel

By placing a sample in the laser-drilled hole of a chip containing microfabricated channels, and carefully aligning and clamping this to our chamber, we were able to measure a photoacoustic signal from the sample in this system, demonstrating proof-of-principle that a microchannel could be used to present sample to a photoacoustic detector. See diagram in **Fig. A8**, and data in **Fig. A9**.

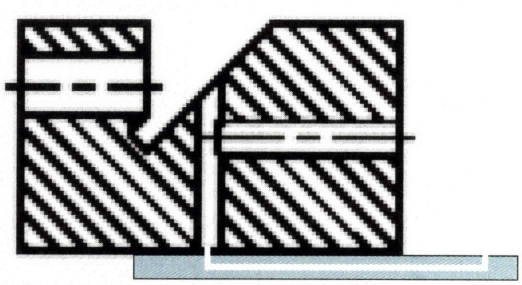

**Fig. A8:** Chip with microchannels coupled to photoacoustic chamber.

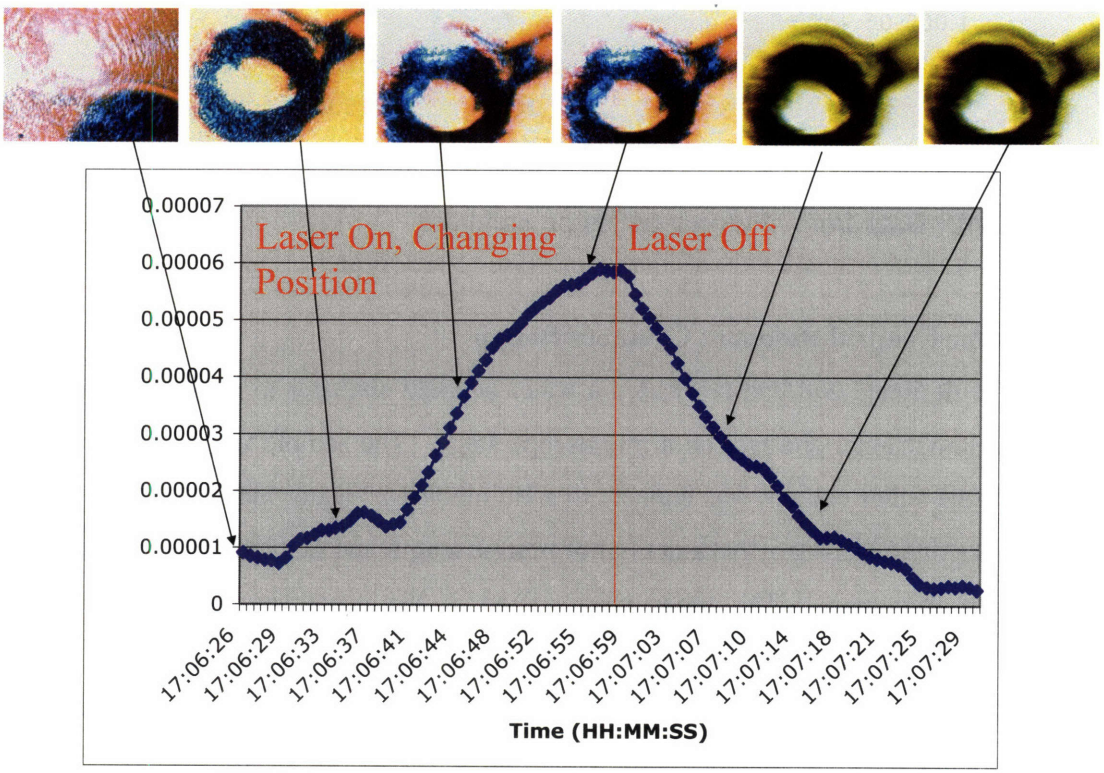


**Fig. A9:** Data from chip with microchannels.

### A1.5 Photoacoutic Measurement on Tissue Samples

To demonstrate the ability of photoacoustics to measure the absorbance of opaque tissue, we obtained calf liver from a supermarket and placed a small piece in our chamber, then detected a photoacoustic signal as shown in **Fig. A10**.

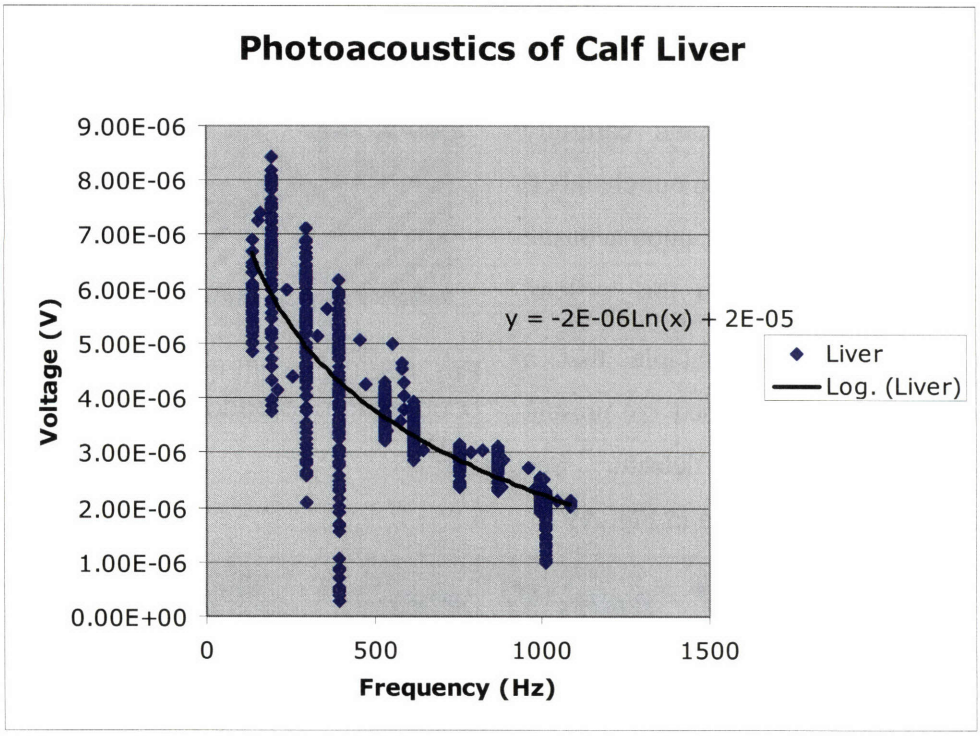


**Fig. A10:** Data from photoacoustics on calf liver.

### A1.6 Water Coupled Resonant Chamber Design

We designed and had fabricated a water coupled chamber to clamp onto a glass slide or microchannel and rest on a microscope stage. The sample was in contact with water and the water column was connect to a Helmholtz resonator made of two stainless steel tubes (McMaster-Carr, Atlanta GA) of precise length and diameter to be resonant at the desired frequency. The tubes were joined at the center by a reducing union (Swagelok, Solon OH). A hydrophone (Bruel & Kjaer, Norcross GA) was placed in the larger chamber, and could be repositioned to vary the volume of the chamber and resonant frequency. The chamber is shown in **Fig. A11.**

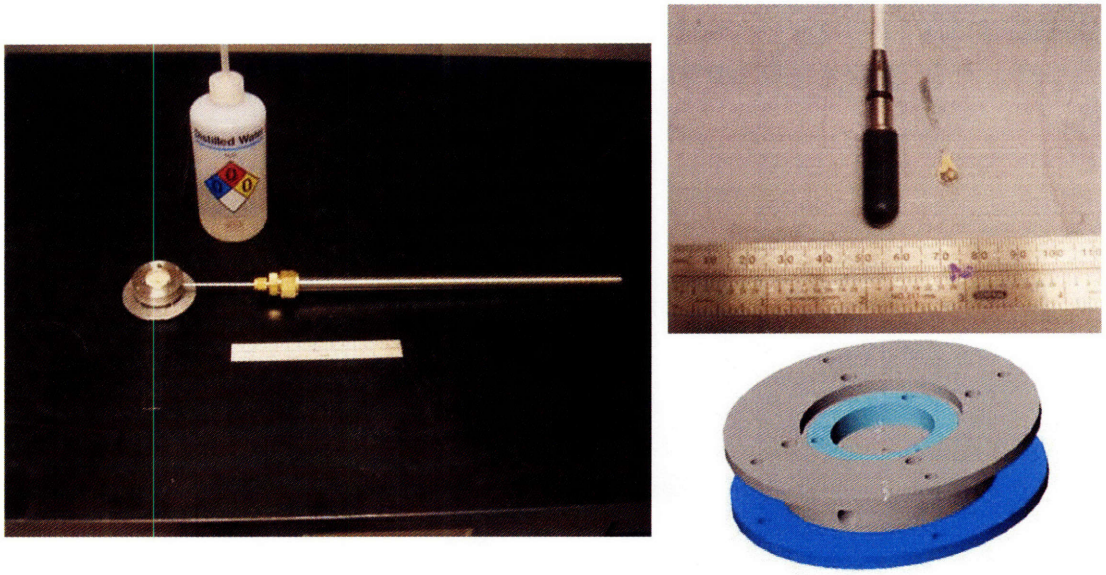

**Fig. A11:** Water coupled resonant chamber.

### A1.7 Air Coupled Resonant UV Chamber Design

We also designed and had fabricated an air-coupled resonant chamber. This chamber was designed to be thinner than the working distance of an Ealing 36X objective so that deep UV light could be focused into it. It was also designed to use standard 1 inch square quartz coverslips as the window. Finally, two diameters of tube were included so that the microphone would rest in a resonant chamber, designed as a Helmholtz resonator to provide approximately 3X pressure amplification. **See Fig. A12**.

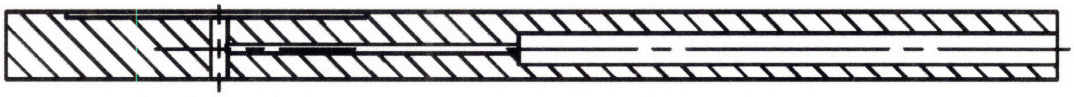

**Fig. A12:** Air coupled resonant chamber designed for Ealing objective.

### A1.8 Deep UV LED-Excited Photoacoustic Measurement

Using a quartz window on our original chamber, we were able to focus the output from a 280nm LED, modulated directly on and off, into the chamber to excite the sample sufficiently to generate a detectable signal. We believe this to be the first demonstration of photoacoustics with a UV LED. The apparatus is shown in **Fig. A13,** and data in **Fig. A14.**

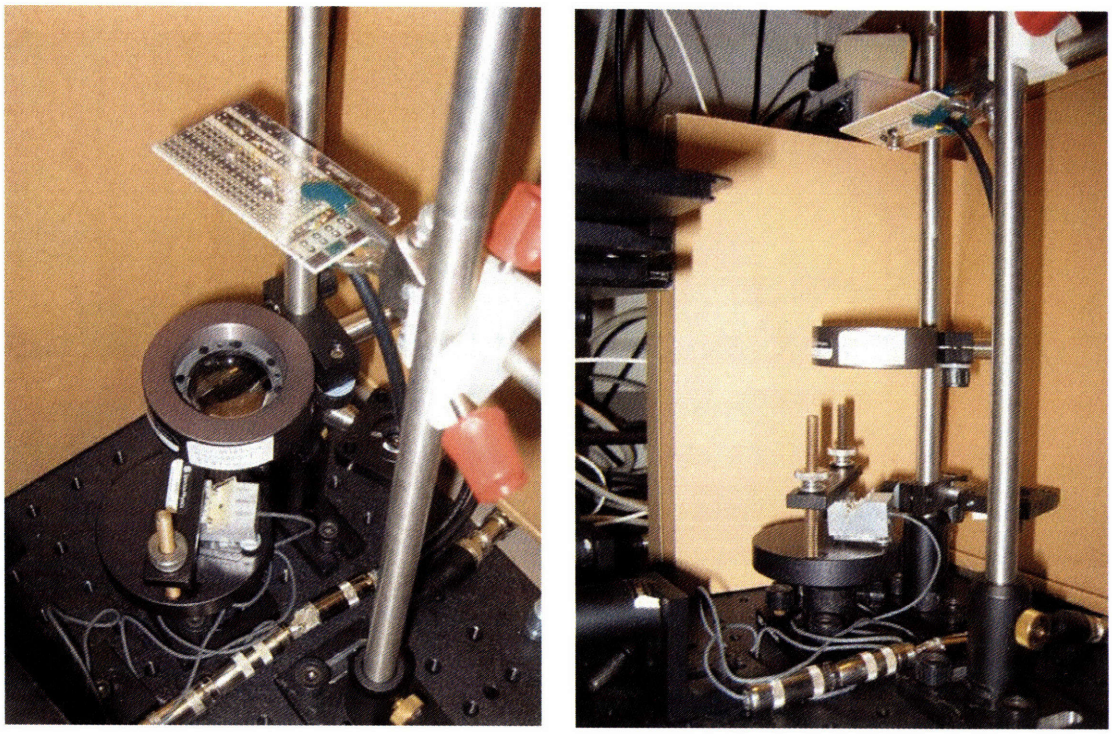

**Fig. A13:** DUV LED photoacoustic apparatus.

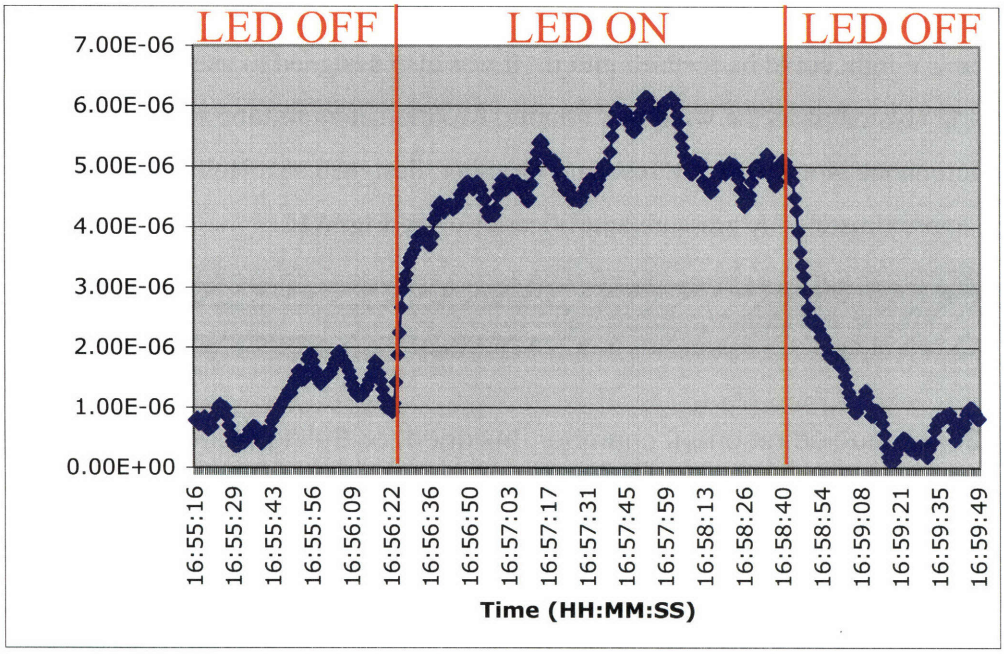


**Fig. A14:** Data from DUV LED photoacoustic apparatus for an activated charcoal sample.

### A1.9 Deep UV Photoacoustic Spectrum Measurement

We were able to focus the output from a mercury lamp and monochrometer, with a chopper in the path, into our photoacoustic chamber which contained a sample of guanosine in solution. Using this setup, we were able to demonstrate the ability of photoacoustic detection to exceed the upper dynamic range of a spectrophotometer, as shown in Fig. A15. We believe this is the most relevant benefit of photoacoustics.

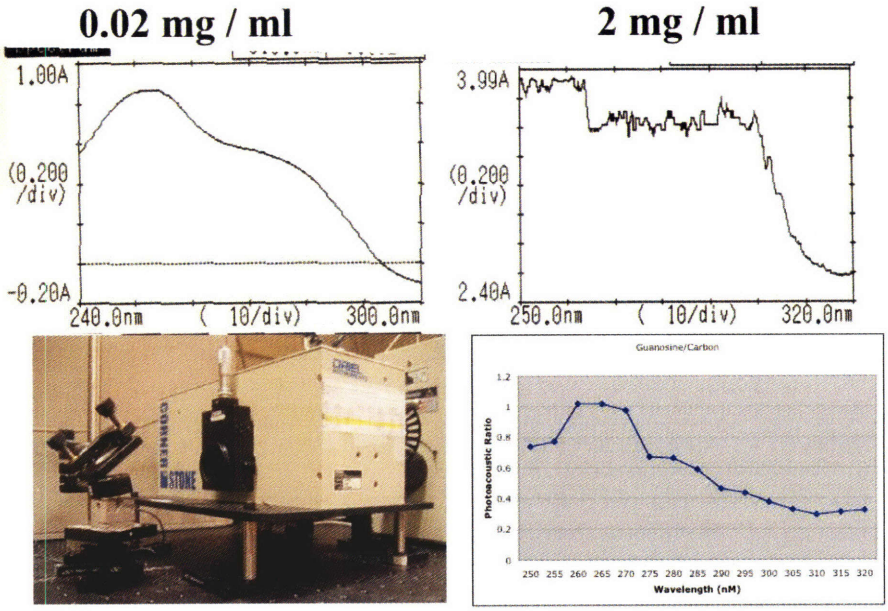


**Fig. A15:** Shimadzu spectrophotometer data at **(top)** low concentration and (**top right**) high concentration, and photoacoustic data at **(bottom right)** high concentration collected on our appartus **(bottom left)** demonstrating the ability of photoacoustics to measure a spectra even on concentrations at which the spectrophotometer saturates.

## Section 2: MATLAB Code

**concalcPb_d_pcheckICgrams.m**

*Code for calculating and displaying OD260/OD280 ratio image, protein mass image, nucleic acid mass image, and quantum yield Image (display range manually set to be appropriate for 190nm pixels).*

```
%------------------------------------------------------------------------
%MATLAB Code for Calculating and Displaying OD260/OD280 Ratio Image, Protein Mass
Image, Nucleic Acid Mass Image, and Quantum
%Yield Image
%
%By Benjamin J. Zeskind, Whitehead Institute for Biomedical Research and
%MIT Division of Biological Engineering
%
%Last Modified: January 6, 2006
%
%Takes as input:
%"filepath" = folder containing image files
%"affile" = file name for autofluorescent (aka native fluorescent) image of subject
%"trans280file" = filename for 280nm transmission image of subject
%"trans260file" = filename for 260nm transmission image of subject
%"back280file" = filename for 280nm transmission image of blank background
%"back260file" = filename for 260nm transmission image of blank background
%"NA" = numerical aperture of objective lens
%"Nimmersion" = index of refraction for objective lens immersion media
%"AFfilterEFF" = percent transmission of emission filter used for native
%   fluorescence measurement; estimated average over relevant wavelengths
%"TRANS280filterEFF" = percent transmission of emission filter used for
%   280nm transmission measurement, at 280nm
%   NOTE: the filter efficiencies are only needed for the quantum yield calculation; they
%   are not needed for calculations involving optical
%   density because each transmission image and its corresponding background
%   are taken with the same emission filter.
%"xval" = x dimension of images in pixels
%"yval" = y dimension of images in pixels
%"pixelsizenm" = the size of one pixel on the sample (in nm)
%"epsilonTRP" = extinction coefficient of tryptophan at 280nm (in 1/(M*cm))
%"epsilon280protein" = average extinction coefficient for protein at 280nm
%   (in 1/(M*cm))
%"epsilon260protein" = average extinction coefficient for protein at 260nm
%   (in 1/(M*cm))
%"epsilon280nucleic" = average extinction coefficient for nucleic acid at 280nm
%    (in 1/(M*cm))
%"molarmassPROTEIN" = molar mass for average protein (in g/mol)
%"molarmassNUCLEIC" = molar mass for average nucleic acid (in g/mol)
%"file280time" = exposure time used for 280m transmission images
%"affiletime" = exposure time used for native fluorescence image
%   NOTE: the file times are only needed for the quantum yield calculation; they
%   are not needed for calculations involving optical
%   density because each transmission image and its corresponding background
%   are taken with the same exposure time.
%"yvalline" = y-value for horizontal line section through the nucleus
%"xvallinestart" = starting x-value for horizontal line section through the nucleus
%"xvallineend" = ending x-value for horizontal line section through the nucleus
```

```
%"pixeldarkvalue" = average offset of camera pixels when shutter closed
%-------------------------------------------------------------------------
function [] = concalcPb_d_pcheckICgrams(filepath, affile, trans280file, trans260file, back280file,
back260file, NA, Nimmersion, AFfilterEFF, TRANS280filterEFF, xval, yval, pixelsizenm,
epsilonTRP,epsilon280protein,epsilon260protein,epsilon280nucleic,molarmassPROTEIN,molarm
assNUCLEIC,file280time,affiletime, yvalline,xvallinestart,xvallineend,pixeldarkvalue)
tic
%-------------------------------------------------------------------------
%Read pixel values from image files into MATLAB
%-------------------------------------------------------------------------
[AFimagepredark] = double(imread([filepath,affile,'.tif'],'tiff'));
[BACK280imagepredark] = double(imread([filepath,back280file,'.tif'],'tiff'));
[BACK260imagepredark] = double(imread([filepath,back260file,'.tif'],'tiff'));
[trans280imagepredark] = double(imread([filepath,trans280file,'.tif'],'tiff'));
[trans260imagepredark] = double(imread([filepath,trans260file,'.tif'],'tiff'));
%-------------------------------------------------------------------------
%Subtract dark value (offset from camera)
%-------------------------------------------------------------------------
[AFimage] = AFimagepredark-double(pixeldarkvalue);
[BACK280image] = BACK280imagepredark-double(pixeldarkvalue);
[BACK260image] = BACK260imagepredark-double(pixeldarkvalue);
[trans280image] = trans280imagepredark-double(pixeldarkvalue);
[trans260image] = trans260imagepredark-double(pixeldarkvalue);
%-------------------------------------------------------------------------
%Calculate optical density at each pixel from transmission images and
%determine ratio
%-------------------------------------------------------------------------
for j = 1:xval
   for k = 1:yval
       OD280image(j,k) = log10(BACK280image(j,k)/trans280image(j,k));
       OD260image(j,k) = log10(BACK260image(j,k)/trans260image(j,k));
       ratioimage(j,k) = OD260image(j,k)/OD280image(j,k);
  end
end
%-------------------------------------------------------------------------
%Plot OD260/OD280 Image; restrict display range to one standard deviation
%above and below the mean in order to prevent noise-induced outliers from
%dominating image
%-------------------------------------------------------------------------
%FLATratioimage = reshape(ratioimage(1:xval,1:yval),1,xval*yval)
%LOWERBOUNDratioimage = mean(FLATratioimage)-std(FLATratioimage);
%UPPERBOUNDratioimage = mean(FLATratioimage)+std(FLATratioimage);
figure
%imagesc(ratioimage,[LOWERBOUNDratioimage UPPERBOUNDratioimage])
imagesc(ratioimage,[0 2])
ax1 = gca;
set(ax1,'FontSize',16,'PlotBoxAspectRatio',[1 1 1]);
colorbar('FontSize',16)
axis('off')
%-------------------------------------------------------------------------
%Calculate Concentration-Pathlength Products for
%Nucleic Acid and Protein from OD260 and OD280 values,
%by solving equation (2) from the text for both wavelengths; built into the
%code below is the assumption that the extinction coefficient of nucleic
%acid at 260nm is 2.0X that at 280nm [Gallagher]
%-------------------------------------------------------------------------
```

```
for i = 1:xval
   for j = 1:yval
   CLprotein(i,j) = ((2*OD280image(i,j))-OD260image(i,j))/((2*epsilon280protein)-
epsilon260protein);
   end
end
for i = 1:xval
   for j = 1:yval
   CLnucleic(i,j) = ((OD280image(i,j)-(epsilon280protein*CLprotein(i,j)))/(epsilon280nucleic));
   end
end
%-------------------------------------------------------------------------
%Calculate mass of nucleic acid and protein in milligrams using the
%concentration-pathlength products, pixel size, and estimated molar
%mass. Factors of 1000 are used to convert liters to ml and grams to mg;
%factor of 10^-7 is used to convert nm to cm; calculation relies on fact
%that 1ml = 1 cm^3.
%-------------------------------------------------------------------------
%MASSprotein = CLprotein*(1/1000)*((pixelsizenm*10^-7)^2)*molarmassPROTEIN*1000;
%MASSnucleic = CLnucleic*(1/1000)*((pixelsizenm*10^-7)^2)*molarmassNUCLEIC*1000;
MASSprotein = CLprotein*(1/1000)*((pixelsizenm*10^-7)^2)*molarmassPROTEIN;
MASSnucleic = CLnucleic*(1/1000)*((pixelsizenm*10^-7)^2)*molarmassNUCLEIC;
%-------------------------------------------------------------------------
%Plot mass images; restrict display range to one standard deviation
%above and below the mean in order to prevent noise-induced outliers from
%dominating image
%-------------------------------------------------------------------------
figure
imagesc(MASSprotein,[0 1e-13]);
ax1 = gca;
set(ax1,'FontSize',16,'PlotBoxAspectRatio',[1 1 1]);
colorbar('FontSize',16)
axis('off')
figure
imagesc(MASSnucleic,[0 1e-14]);
ax1 = gca;
set(ax1,'FontSize',16,'PlotBoxAspectRatio',[1 1 1]);
colorbar('FontSize',16)
axis('off')
%-------------------------------------------------------------------------
%Create line plots of mass; divide pixel size by 1000 to get length in um
%-------------------------------------------------------------------------
nucleusxscale = (pixelsizenm/1000)*(0:(xvallineend-xvallinestart));
figure
plot(nucleusxscale,MASSprotein(yvalline,xvallinestart:xvallineend),'-b.');
axis([0 25 0 1e-13]);
ax1 = gca;
set(ax1,'FontSize',16);
xlabel('Distance (um)','FontSize',16)
ylabel('Protein Mass (g)','FontSize',16)
figure
plot(nucleusxscale,MASSnucleic(yvalline,xvallinestart:xvallineend),'-b.');
axis([0 25 0 1e-14]);
ax1 = gca;
set(ax1,'FontSize',16);
xlabel('Distance (um)','FontSize',16)
```

```
ylabel('Nucleic Acid Mass (g)','FontSize',16)
%----------------------------------------
%Calculate optical density due to tryptophan alone in preparation for
%calculation quantum yield, based on average 466
%amino acid protein [Lodish] and 1.4% frequency of tryptophan [Voet]
%----------------------------------------
CLtrp = CLprotein*466*.014;
TRPabs = CLtrp*epsilonTRP;
%----------------------------------------
% Calculate collection angle of objective lens
%----------------------------------------
collectionangle = 2*(asin(NA/Nimmersion));
%----------------------------------------
%Calculate QYIELD image; normalize for different exposure times and filter
%efficiencies
%----------------------------------------
for i = 1:xval
   for j = 1:yval
      qyield(i,j) =
(AFimage(i,j)*((2*pi)/collectionangle)*(file280time/affiletime)*(TRANS280filterEFF/AFfilterEFF))/(B
ACK280image(i,j)*(1-(10^-TRPabs(i,j))));
   end
end
figure
imagesc(qyield,[0 0.12])
FLATqyield = reshape(qyield(1:xval,1:yval),1,xval*yval);
LOWERBOUNDqyield = mean(FLATqyield)-std(FLATqyield);
UPPERBOUNDqyield = mean(FLATqyield)+std(FLATqyield);
%imagesc(qyield,[LOWERBOUNDqyield,UPPERBOUNDqyield]);
ax1 = gca;
set(ax1,'FontSize',16,'PlotBoxAspectRatio',[1 1 1]);
colorbar('FontSize',16)
axis('off')
figure
plot(nucleusxscale,qyield(yvalline,xvallinestart:xvallineend),'-b.');
axis([0 25 0 0.12]);
ax1 = gca;
set(ax1,'FontSize',16);
xlabel('Distance (um)','FontSize',16)
ylabel('Quantum Yield','FontSize',16)
toc
t=toc
```

**concalcPb_d_pcheck_grams.m**

*Code for calculating and displaying OD260/OD280 ratio image, protein mass image, nucleic acid mass image, and quantum yield Image (display range manually set to be appropriate for 92nm pixels).*

```
%--------------------------------------------------------------------------
%MATLAB Code for Calculating and Displaying OD260/OD280 Ratio Image, Protein Mass
Image, Nucleic Acid Mass Image, and Quantum
%Yield Image
%
%By Benjamin J. Zeskind, Whitehead Institute for Biomedical Research and
%MIT Division of Biological Engineering
%
%Last Modified: January 6, 2006
%
%Takes as input:
%"filepath" = folder containing image files
%"affile" = file name for autofluorescent (aka native fluorescent) image of subject
%"trans280file" = filename for 280nm transmission image of subject
%"trans260file" = filename for 260nm transmission image of subject
%"back280file" = filename for 280nm transmission image of blank background
%"back260file" = filename for 260nm transmission image of blank background
%"NA" = numerical aperture of objective lens
%"Nimmersion" = index of refraction for objective lens immersion media
%"AFfilterEFF" = percent transmission of emission filter used for native
%   fluorescence measurement; estimated average over relevant wavelengths
%"TRANS280filterEFF" = percent transmission of emission filter used for
%   280nm transmission measurement, at 280nm
%   NOTE: the filter efficiencies are only needed for the quantum yield calculation; they
%   are not needed for calculations involving optical
%   density because each transmission image and its corresponding background
%   are taken with the same emission filter.
%"xval" = x dimension of images in pixels
%"yval" = y dimension of images in pixels
%"pixelsizenm" = the size of one pixel on the sample (in nm)
%"epsilonTRP" = extinction coefficient of tryptophan at 280nm (in 1/(M*cm))
%"epsilon280protein" = average extinction coefficient for protein at 280nm
%   (in 1/(M*cm))
%"epsilon260protein" = average extinction coefficient for protein at 260nm
%   (in 1/(M*cm))
%"epsilon280nucleic" = average extinction coefficient for nucleic acid at 280nm
%    (in 1/(M*cm))
%"molarmassPROTEIN" = molar mass for average protein (in g/mol)
%"molarmassNUCLEIC" = molar mass for average nucleic acid (in g/mol)
%"file280time" = exposure time used for 280m transmission images
%"affiletime" = exposure time used for native fluorescence image
%   NOTE: the file times are only needed for the quantum yield calculation; they
%   are not needed for calculations involving optical
%   density because each transmission image and its corresponding background
%   are taken with the same exposure time.
%"yvalline" = y-value for horizontal line section through the nucleus
%"xvallinestart" = starting x-value for horizontal line section through the nucleus
%"xvallineend" = ending x-value for horizontal line section through the nucleus
%"pixeldarkvalue" = average offset of camera pixels when shutter closed
%--------------------------------------------------------------------------
```

```
function [] = concalcPb_d_pcheck_grams(filepath, affile, trans280file, trans260file, back280file,
back260file, NA, Nimmersion, AFfilterEFF, TRANS280filterEFF, xval, yval, pixelsizenm,
epsilonTRP,epsilon280protein,epsilon260protein,epsilon280nucleic,molarmassPROTEIN,molarm
assNUCLEIC,file280time,affiletime, yvalline,xvallinestart,xvallineend,pixeldarkvalue)
tic
%--------------------------------------------------------------------------
%Read pixel values from image files into MATLAB
%--------------------------------------------------------------------------
[AFimagepredark] = double(imread([filepath,affile,'.tif'],'tiff'));
[BACK280imagepredark] = double(imread([filepath,back280file,'.tif'],'tiff'));
[BACK260imagepredark] = double(imread([filepath,back260file,'.tif'],'tiff'));
[trans280imagepredark] = double(imread([filepath,trans280file,'.tif'],'tiff'));
[trans260imagepredark] = double(imread([filepath,trans260file,'.tif'],'tiff'));
%--------------------------------------------------------------------------
%Subtract dark value (offset from camera)
%--------------------------------------------------------------------------
[AFimage] = AFimagepredark-double(pixeldarkvalue);
[BACK280image] = BACK280imagepredark-double(pixeldarkvalue);
[BACK260image] = BACK260imagepredark-double(pixeldarkvalue);
[trans280image] = trans280imagepredark-double(pixeldarkvalue);
[trans260image] = trans260imagepredark-double(pixeldarkvalue);
%--------------------------------------------------------------------------
%Calculate optical density at each pixel from transmission images and
%determine ratio
%--------------------------------------------------------------------------
for j = 1:xval
   for k = 1:yval
       OD280image(j,k) = log10(BACK280image(j,k)/trans280image(j,k));
       OD260image(j,k) = log10(BACK260image(j,k)/trans260image(j,k));
       ratioimage(j,k) = OD260image(j,k)/OD280image(j,k);
  end
end
%--------------------------------------------------------------------------
%Plot OD260/OD280 Image; restrict display range to one standard deviation
%above and below the mean in order to prevent noise-induced outliers from
%dominating image
%--------------------------------------------------------------------------
%FLATratioimage = reshape(ratioimage(1:xval,1:yval),1,xval*yval)
%LOWERBOUNDratioimage = mean(FLATratioimage)-std(FLATratioimage);
%UPPERBOUNDratioimage = mean(FLATratioimage)+std(FLATratioimage);
figure
%imagesc(ratioimage,[LOWERBOUNDratioimage UPPERBOUNDratioimage])
imagesc(ratioimage,[0 2])
ax1 = gca;
set(ax1,'FontSize',16,'PlotBoxAspectRatio',[1 1 1]);
colorbar('FontSize',16)
axis('off')
%--------------------------------------------------------------------------
%Calculate Concentration-Pathlength Products for
%Nucleic Acid and Protein from OD260 and OD280 values,
%by solving equation (2) from the text for both wavelengths; built into the
%code below is the assumption that the extinction coefficient of nucleic
%acid at 260nm is 2.0X that at 280nm [Gallagher]
%--------------------------------------------------------------------------
for i = 1:xval
   for j = 1:yval
```

```
   CLprotein(i,j) = ((2*OD280image(i,j))-OD260image(i,j))/((2*epsilon280protein)-
epsilon260protein);
   end
end
for i = 1:xval
   for j = 1:yval
   CLnucleic(i,j) = ((OD280image(i,j)-(epsilon280protein*CLprotein(i,j)))/(epsilon280nucleic));
   end
end
%-------------------------------------------------------------------------
%Calculate mass of nucleic acid and protein in milligrams using the
%concentration-pathlength products, pixel size, and estimated molar
%mass. Factors of 1000 are used to convert liters to ml and grams to mg;
%factor of 10^-7 is used to convert nm to cm; calculation relies on fact
%that 1ml = 1 cm^3.
%-------------------------------------------------------------------------
MASSprotein = CLprotein*(1/1000)*((pixelsizenm*10^-7)^2)*molarmassPROTEIN;
MASSnucleic = CLnucleic*(1/1000)*((pixelsizenm*10^-7)^2)*molarmassNUCLEIC;
%-------------------------------------------------------------------------
%Plot mass images; restrict display range to one standard deviation
%above and below the mean in order to prevent noise-induced outliers from
%dominating image
%-------------------------------------------------------------------------
figure
imagesc(MASSprotein,[0 2e-14]);
ax1 = gca;
set(ax1,'FontSize',16,'PlotBoxAspectRatio',[1 1 1]);
colorbar('FontSize',16)
axis('off')
figure
imagesc(MASSnucleic,[0 2e-15]);
ax1 = gca;
set(ax1,'FontSize',16,'PlotBoxAspectRatio',[1 1 1]);
colorbar('FontSize',16)
axis('off')
%-------------------------------------------------------------------------
%Create line plots of mass; divide pixel size by 1000 to get length in um
%-------------------------------------------------------------------------
nucleusxscale = (pixelsizenm/1000)*(0:(xvallineend-xvallinestart));
figure
plot(nucleusxscale,MASSprotein(yvalline,xvallinestart:xvallineend),'-b.');
ax1 = gca;
set(ax1,'FontSize',16);
xlabel('Distance (um)','FontSize',16)
ylabel('Protein Mass (mg)','FontSize',16)
figure
plot(nucleusxscale,MASSnucleic(yvalline,xvallinestart:xvallineend),'-b.');
ax1 = gca;
set(ax1,'FontSize',16);
xlabel('Distance (um)','FontSize',16)
ylabel('Nucleic Acid Mass (mg)','FontSize',16)
%-----------------------------------------
%Calculate optical density due to tryptophan alone in preparation for
%calculation quantum yield, based on average 466
%amino acid protein [Lodish] and 1.4% frequency of tryptophan [Voet]
%-----------------------------------------
```

```
CLtrp = CLprotein*466*.014;
TRPabs = CLtrp*epsilonTRP;
%-----------------------------------------
% Calculate collection angle of objective lens
%-----------------------------------------
collectionangle = 2*(asin(NA/Nimmersion));
%-----------------------------------------
%Calculate QYIELD image; normalize for different exposure times and filter
%efficiencies
%-----------------------------------------
for i = 1:xval
   for j = 1:yval
      qyield(i,j) =
(AFimage(i,j)*((2*pi)/collectionangle)*(file280time/affiletime)*(TRANS280filterEFF/AFfilterEFF))/(B
ACK280image(i,j)*(1-(10^-TRPabs(i,j))));
   end
end
figure
imagesc(qyield,[0 0.12])
FLATqyield = reshape(qyield(1:xval,1:yval),1,xval*yval);
LOWERBOUNDqyield = mean(FLATqyield)-std(FLATqyield);
UPPERBOUNDqyield = mean(FLATqyield)+std(FLATqyield);
%imagesc(qyield,[LOWERBOUNDqyield,UPPERBOUNDqyield]);
ax1 = gca;
set(ax1,'FontSize',16,'PlotBoxAspectRatio',[1 1 1]);
colorbar('FontSize',16)
axis('off')
figure
plot(nucleusxscale,qyield(yvalline,xvallinestart:xvallineend),'-b.');
ax1 = gca;
set(ax1,'FontSize',16);
xlabel('Distance (um)','FontSize',16)
ylabel('Quantum Yield','FontSize',16)
toc
t=toc
```

**FOURwheelstacksplitter_C.m**

*Code for separating four-wavelength image stacks (acquired with DUALwheel_A.m) into separate files.*

```
function [] = FOURwheelstacksplitter_C(filepath, transfile, numofframes,xval, yval)
tic
m = 1;
n = 1;
o = 1;
p = 1;
trans280image = zeros(xval,yval,numofframes/4);
trans260image = zeros(xval,yval,numofframes/4);
trans320image = zeros(xval,yval,numofframes/4);
trans340image = zeros(xval,yval,numofframes/4);
for i = 1:numofframes
if rem(i,4) == 0
   trans340image(:,:,m) = double(imread([filepath,transfile,'.tif'],'tiff',i));
   m = m+1
elseif rem(i,4) == 3
   trans260image(:,:,n) = double(imread([filepath,transfile,'.tif'],'tiff',i));
   n = n+1
elseif rem(i,4) == 2
   trans320image(:,:,o) = double(imread([filepath,transfile,'.tif'],'tiff',i));
   o = o+1
elseif rem(i,4) == 1
   trans280image(:,:,p) = double(imread([filepath,transfile,'.tif'],'tiff',i));
   p = p+1
end
end
for i = 1:(numofframes/4)
imwrite(uint16(trans260image(:,:,i)),[filepath,transfile,'_260.tif'],'tiff','compression','none','WriteMod
e','append')
imwrite(uint16(trans280image(:,:,i)),[filepath,transfile,'_280.tif'],'tiff','compression','none','WriteMod
e','append')
imwrite(uint16(trans320image(:,:,i)),[filepath,transfile,'_320.tif'],'tiff','compression','none','WriteMod
e','append')
imwrite(uint16(trans340image(:,:,i)),[filepath,transfile,'_340.tif'],'tiff','compression','none','WriteMod
e','append')
end
end
```

**multipleMASSmaps_CORR_C_nocluster.m**

*Code for calculating background-normalized, scattering corrected protein and nucleic acid mass maps for a four-wavelength time-lapse series of images. Assumes that FOURwheelstacksplitter_C.m has already been run.*

```
function [Mn, Mp, Mcn, Mcp] = multipleMASSmaps_CORR_B_nocluster(filepath, transfile,
backfile,startframe,numoffframes,numofbackframes,xval, yval,pixelsizenm,
epsilonTRP,epsilon280protein,epsilon260protein,epsilon280nucleic,molarmassPROTEIN,molarm
assNUCLEIC,pixeldarkvalue,blankYstart,blankheight,blankXstart,blankwidth)
tic
%Read in the entire background file at each wavlength
for i = 1:numofbackframes
   backfile_280(:,:,i) = double(imread([filepath,backfile,'_280','.tif],'tiff',i));
   backfile_260(:,:,i) = double(imread([filepath,backfile,'_260','.tif],'tiff',i));
   backfile_320(:,:,i) = double(imread([filepath,backfile,'_320','.tif],'tiff',i));
   backfile_340(:,:,i) = double(imread([filepath,backfile,'_340','.tif],'tiff',i));
end
%subtract pixel dark value
[backfile_280_corr] = backfile_280-double(pixeldarkvalue);
[backfile_260_corr] = backfile_260-double(pixeldarkvalue);
[backfile_320_corr] = backfile_320-double(pixeldarkvalue);
[backfile_340_corr] = backfile_340-double(pixeldarkvalue);
%create an average background image at each wavelength
   for j = 1:xval
      for k = 1:yval
      avg280back(j,k) = mean(backfile_280_corr(j,k,:));
      avg260back(j,k) = mean(backfile_260_corr(j,k,:));
      avg320back(j,k) = mean(backfile_320_corr(j,k,:));
      avg340back(j,k) = mean(backfile_340_corr(j,k,:));
      end
   end
%caculate mass maps for each time point
for i = startframe:numoffframes
    [MASSprotein, MASSnucleic, correctedMASSprotein, correctedMASSnucleic] =
scattMASSmap_B(i,filepath, [transfile,'_280'],[transfile,'_260'],[transfile,'_320'],[transfile,'_340'],
avg280back,avg260back, avg320back,avg340back,xval, yval, pixelsizenm,
epsilonTRP,epsilon280protein,epsilon260protein,epsilon280nucleic,molarmassPROTEIN,molarm
assNUCLEIC,pixeldarkvalue,blankYstart,blankheight,blankXstart,blankwidth);
%display and capture protein mass map at each timepoint
   imagesc(MASSprotein,[0 2e-14]);
   truesize
   axis('off')
   Mp(i) = getframe;
   imagesc(correctedMASSprotein,[0 2e-14]);
   truesize
   axis('off')
   Mcp(i) = getframe;
   %display and capture nucleic acid mass map at each timepoint
imagesc(MASSnucleic,[0 2.5e-15]);
   truesize
   axis('off')
   Mn(i) = getframe;
imagesc(correctedMASSnucleic,[0 2.5e-15]);
   truesize
   axis('off')
   Mcn(i) = getframe;
```

```
%
imwrite(frame2im(Mp(i)),[filepath,transfile,'_MASSproteincolor_blanknorm_',i,'.tif'],'tiff','compressio
n','none','WriteMode','append')

imwrite(frame2im(Mp(i)),[filepath,transfile,'_MASSproteincolor_blanknorm_',num2str(i),'.tif'],'tiff','c
ompression','none','WriteMode','append')

imwrite(frame2im(Mn(i)),[filepath,transfile,'_MASSnucleiccolor_blanknorm_',num2str(i),'.tif'],'tiff','c
ompression','none','WriteMode','append')

imwrite(frame2im(Mcp(i)),[filepath,transfile,'_corr_MASSproteincolor_blanknorm_',num2str(i),'.tif'],
'tiff','compression','none','WriteMode','append')

imwrite(frame2im(Mcn(i)),[filepath,transfile,'_corr_MASSnucleiccolor_blanknorm_',num2str(i),'.tif'],
'tiff','compression','none','WriteMode','append')

imwrite(uint16(MASSprotein.*10^18),[filepath,transfile,'_MASSprotein1018_blanknorm_',num2str(
i),'.tif'],'tiff','compression','none','WriteMode','append')

imwrite(uint16(MASSnucleic.*10^19),[filepath,transfile,'_MASSnucleic1019_blanknorm_',num2str(
i),'.tif'],'tiff','compression','none','WriteMode','append')

imwrite(uint16(correctedMASSprotein.*10^18),[filepath,transfile,'_corr_MASSprotein1018_blankn
orm_',num2str(i),'.tif'],'tiff','compression','none','WriteMode','append')

imwrite(uint16(correctedMASSnucleic.*10^19),[filepath,transfile,'_corr_MASSnucleic1019_blankn
orm_',num2str(i),'.tif'],'tiff','compression','none','WriteMode','append')
   finalstep = i
end
toc
t= toc
```

**scattMASSmap_B.m**

*Subroutine called by multipleMASSmaps_CORR_C_nocluster.m for determining scattering correction factor and mass maps.*

```
function [MASSprotein, MASSnucleic, correctedMASSprotein, correctedMASSnucleic] =
scattMASSmap_B(fileindex,filepath, trans280file, trans260file, trans320file, trans340file,
BACK280image, BACK260image, BACK320image, BACK340image, xval, yval, pixelsizenm,
epsilonTRP,epsilon280protein,epsilon260protein,epsilon280nucleic,molarmassPROTEIN,molarm
assNUCLEIC,pixeldarkvalue,blankYstart,blankheight,blankXstart,blankwidth)
%--------------------------------------------------------------------------
%Version B scales background to match
%Read pixel values from image files into MATLAB
%--------------------------------------------------------------------------
[trans280imagepredark] = double(imread([filepath,trans280file,'.tif'],'tiff',fileindex));
[trans260imagepredark] = double(imread([filepath,trans260file,'.tif'],'tiff',fileindex));
[trans320imagepredark] = double(imread([filepath,trans320file,'.tif'],'tiff',fileindex));
[trans340imagepredark] = double(imread([filepath,trans340file,'.tif'],'tiff',fileindex));
%--------------------------------------------------------------------------
%Subtract dark value (offset from camera)
%--------------------------------------------------------------------------
[trans280image] = trans280imagepredark-double(pixeldarkvalue);
[trans260image] = trans260imagepredark-double(pixeldarkvalue);
[trans320image] = trans320imagepredark-double(pixeldarkvalue);
[trans340image] = trans340imagepredark-double(pixeldarkvalue);
%--------------------------------------------------------------------------
scaling280factor =
(mean(mean(trans280image(blankYstart:blankYstart+blankheight,blankXstart:blankXstart+blankw
idth))))/(mean(mean(BACK280image(blankYstart:blankYstart+blankheight,blankXstart:blankXstar
t+blankwidth))));
scaling260factor =
(mean(mean(trans260image(blankYstart:blankYstart+blankheight,blankXstart:blankXstart+blankw
idth))))/(mean(mean(BACK260image(blankYstart:blankYstart+blankheight,blankXstart:blankXstar
t+blankwidth))));
scaling320factor =
(mean(mean(trans320image(blankYstart:blankYstart+blankheight,blankXstart:blankXstart+blankw
idth))))/(mean(mean(BACK320image(blankYstart:blankYstart+blankheight,blankXstart:blankXstar
t+blankwidth))));
scaling340factor =
(mean(mean(trans340image(blankYstart:blankYstart+blankheight,blankXstart:blankXstart+blankw
idth))))/(mean(mean(BACK340image(blankYstart:blankYstart+blankheight,blankXstart:blankXstar
t+blankwidth))));
%--------------------------------------------------------------------------
%Calculate optical density at each pixel from transmission images and
%determine ratio
%--------------------------------------------------------------------------
for j = 1:xval
   for k = 1:yval
       OD280image(j,k) = log10(scaling280factor*BACK280image(j,k)/trans280image(j,k));
       OD260image(j,k) = log10(scaling260factor*BACK260image(j,k)/trans260image(j,k));
       OD320image(j,k) = log10(scaling320factor*BACK320image(j,k)/trans320image(j,k));
       OD340image(j,k) = log10(scaling340factor*BACK340image(j,k)/trans340image(j,k));
   end
end
%--------------------------------------------------------------------------
%Calculate scattering correction factor
%--------------------------------------------------------------------------
```

```
warning('off','all');
for i = 1:xval
   for j = 1:yval
      xvals = [320;340];
      yvals = [OD320image(i,j);OD340image(i,j)];
      [beta] = nlinfit(xvals,yvals,@mieB,[23 3]);
      %[beta] = nlinfit(xvals,yvals,@mieB,[23 3],'MaxIter',300,'Display','off');
      correction260val(i,j) = mieB(beta,260);
      correction280val(i,j) = mieB(beta,280);
      vals = [i,j];
   end
end
OD260corrected = OD260image-correction260val;
OD280corrected = OD280image-correction280val;
%Calculate corrected mass values
for i = 1:xval
   for j = 1:yval
   CLprotein(i,j) = ((2*OD280image(i,j))-OD260image(i,j))/((2*epsilon280protein)-
epsilon260protein);
   correctedCLprotein(i,j) = ((2*OD280corrected(i,j))-OD260corrected(i,j))/((2*epsilon280protein)-
epsilon260protein);
   end
end
for i = 1:xval
   for j = 1:yval
   CLnucleic(i,j) = ((OD280image(i,j)-(epsilon280protein*CLprotein(i,j)))/(epsilon280nucleic));
   correctedCLnucleic(i,j) = ((OD280corrected(i,j)-
(epsilon280protein*correctedCLprotein(i,j)))/(epsilon280nucleic));
   end
end
%-------------------------------------------------------------------------
%Calculate mass of nucleic acid and protein in milligrams using the
%concentration-pathlength products, pixel size, and estimated molar
%mass. Factors of 1000 are used to convert liters to ml and grams to mg;
%factor of 10^-7 is used to convert nm to cm; calculation relies on fact
%that 1ml = 1 cm^3.
%-------------------------------------------------------------------------
MASSprotein = CLprotein*(1/1000)*((pixelsizenm*10^-7)^2)*molarmassPROTEIN;
correctedMASSprotein = correctedCLprotein*(1/1000)*((pixelsizenm*10^-
7)^2)*molarmassPROTEIN;
MASSnucleic = CLnucleic*(1/1000)*((pixelsizenm*10^-7)^2)*molarmassNUCLEIC;
correctedMASSnucleic = correctedCLnucleic*(1/1000)*((pixelsizenm*10^-
7)^2)*molarmassNUCLEIC;
```

**mieB**

```
function [OD] = mieB(nsconandl,lambda)
n = 1.35;
nc = 1.46;
OD = nsconandl(1).*(1/4.606)*pi*nsconandl(2).^2*(1-((sin(2*pi*nsconandl(2)*nc*(n-
1)./lambda))./(pi*nsconandl(2)*nc*(n-1)./lambda))+((sin(pi*nsconandl(2)*nc*(n-
1)./lambda))./(pi*nsconandl(2)*nc*(n-1)./lambda)).^2);
end
```

**wheelstacksplitter_C.m**

*Code for splitting 2-wavelength stacks (taken with wheelonly_B.m) into separate files.*

```
function [] = wheelstacksplitter_C(filepath, transfile, numoffframes,xval, yval)
tic
m = 1;
n = 1;
trans280image = zeros(xval,yval,numoffframes/2);
trans260image = zeros(xval,yval,numoffframes/2);
for i = 1:numoffframes
if rem(i,2) == 1
   trans280image(:,:,m) = double(imread([filepath,transfile,'.tif'],'tiff',i));
   m = m+1
elseif rem(i,2) == 0
   trans260image(:,:,n) = double(imread([filepath,transfile,'.tif'],'tiff',i));
   n = n+1;
end
end
for i = 1:(numoffframes/2)
imwrite(uint16(trans260image(:,:,i)),[filepath,transfile,'_260.tif'],'tiff','compression','none','WriteMod
e','append')
imwrite(uint16(trans280image(:,:,i)),[filepath,transfile,'_280.tif'],'tiff','compression','none','WriteMod
e','append')
end
end
```

**DUALwheel_A.m**

*Instrument control code for synchronizing emission and excitation filter wheels.*

```
for i = 1:10
timeforwheelinplaceandsnap = 1;
timebetweenframes = 10;
emission = serial('COM2');
set(emission,'BaudRate',9600,'DataBits',8,'Parity','none','StopBits',1,'FlowControl','none','Terminat
or','CR');
excitation = serial('COM1');
set(excitation,'BaudRate',9600,'DataBits',8,'Parity','none','StopBits',1,'FlowControl','none','Termina
tor','CR');
fopen(excitation);
fprintf(excitation,'trig=1\n')
fopen(emission);
fprintf(emission,'trig=1\n')
%----------------start actual sequence
fprintf(excitation,'pos=6\n')
t2 = timer('TimerFcn','disp("")','StartDelay', timeforwheelinplaceandsnap);
start(t2)
wait(t2)
fprintf(emission,'pos=1\n')
t3 = timer('TimerFcn','disp("")','StartDelay', timeforwheelinplaceandsnap);
start(t3)
wait(t3)
fprintf(excitation,'pos=2\n')
t4 = timer('TimerFcn','disp("")','StartDelay', timeforwheelinplaceandsnap);
start(t4)
wait(t4)
fprintf(emission,'pos=6\n')
t5 = timer('TimerFcn','disp("")','StartDelay', timeforwheelinplaceandsnap);
start(t5)
wait(t5)
fprintf(excitation,'pos=3\n')
t6 = timer('TimerFcn','disp("")','StartDelay', timeforwheelinplaceandsnap);
start(t6)
wait(t6)
fprintf(emission,'pos=1\n')
t7 = timer('TimerFcn','disp("")','StartDelay', timeforwheelinplaceandsnap);
start(t7)
wait(t7)
fprintf(excitation,'pos=1\n')
t8 = timer('TimerFcn','disp("")','StartDelay', timeforwheelinplaceandsnap);
start(t8)
wait(t8)
fprintf(emission,'pos=6\n')
t9 = timer('TimerFcn','disp("")','StartDelay', timebetweenframes);
start(t9)
wait(t9)
fclose(excitation)
delete(excitation)
clear excitation
fclose(emission)
delete(emission)
clear emission
```

```
%fclose(instrfind)
delete(timerfind)
ben = i
end
```

**wheelonly_B.m**
*Instrument control code for alternating excitation wheel between two wavelengths.*

```
for i = 1:10
timeforwheelinplaceandsnap = 2;
timebetweenframes = 60;
s = serial('COM1');
set(s,'BaudRate',9600,'DataBits',8,'Parity','none','StopBits',1,'FlowControl','none','Terminator','CR')
;
fopen(s);
fprintf(s,'trig=1\n')
fprintf(s,'pos=6\n')
t2 = timer('TimerFcn','disp("")','StartDelay', timeforwheelinplaceandsnap);
start(t2)
wait(t2)
fprintf(s,'pos=1\n')
t3 = timer('TimerFcn','disp("")','StartDelay', timebetweenframes);
start(t3)
wait(t3)
fclose(s)
delete(s)
clear s
%fclose(instrfind)
delete(timerfind)
ben = i
end
```